Contributions of Muscle, Skin, and Adipose Tissue to Indentation Response, Assessed with Computational Arm Model Under Quasi-Static Conditions

by

Bartłomiej Michał Pilarczyk

A thesis

presented to the University of Waterloo

in fulfilment of the

thesis requirement for the degree of

Master of Applied Science

in

Mechanical and Mechatronics Engineering

Waterloo, Ontario, Canada, 2019

Author's Declaration

I hereby declare that I am the sole author of this thesis. This is a true copy of the thesis, including any required final revisions, as accepted by my examiners.

I understand that my thesis may be made electronically available to the public.

Abstract

Computational Human Body Models (HBMs) enable the assessment of human response in potentially injurious impact scenarios; however, to do so HBMs require biofidelic material representations to predict the potential for injury risk. HBMs are recently seeing a widespread application in modelling vehicle occupant response for car crash scenarios. Although the soft tissue deformations in these scenarios occur at high deformation rates, a biofidelic model requires quasi-static properties of the tissues prior to the incorporation of deformation rate effects. Specifically, soft tissues such as skeletal muscle, adipose tissue, and skin play an important role in impact response including supporting and protecting the internal organs.

At present, the mechanical responses of muscle, skin, and adipose tissue are measured using excised tissue experiments and assessed at the individual tissue level, providing a valuable source of information on the behaviour of a particular tissue. Current computational models use these experimental results to define individual tissue response. However, the literature review revealed that there is a paucity of experimental and numerical studies assessing the cooperation of the soft tissues and their joint contribution to a loading scenario. The current study addresses this paucity by creating a Simplified Arm Model (SAM) comprising skeletal muscle, adipose tissue, and skin assessed using a quasi-static upper arm indentation test. In this study, material properties for the skeletal muscle, adipose tissue, and skin were collected from individual experimental tissue tests reported in the literature. This data set was called New Soft Tissues (NST), and the properties were implemented in the SAM. Finally, the arm model was assessed using a quasi-static indentation test and the predicted force-displacement response was compared to a published human volunteer data set.

The model predicted the response of the upper arm to the indentation in agreement with the shape and the magnitude of the experimental data. The work performed by the indenter differed by 2% to 65% from the experimental response. To address the variability within the human population, a series of parametric studies were performed assessing: skin thickness, skin age, and the circumference of the arm. The response of the SAM to indentation was close to the experimental average and demonstrated sensitivity to arm diameter. Moreover, the current study showed that the main contributor to the indentation response was the compressive properties of the muscle

tissue followed by the adipose tissue, and to a lesser extent the skin. Future research should consider deformation rate effects and the importance of muscle activation on response.

Acknowledgements

I would like to express my gratitude for help and guidance in the world of biomechanics to my supervisor, Duane Cronin. I am very fortunate to have worked with him and being guided on the winding road of biomechanical modelling.

I would like to thank my co-supervisor, Ciaran Simms from Trinity College Dublin, Ireland, for a different perspective and additional insight into my work.

I am pleased to thank the Global Human Body Models Consortium (GHBMC) for their financial support and vast knowledge about human body modelling.

Moreover, I would like to thank Günther Benderoth from the Frankfurt University of Applied Sciences for sharing additional experimental data that was used to validate the model I have developed in my research.

I want to thank my colleagues and fellow students within the Impact Mechanics and Material Characterization group (IMMC) for their insight, help, and moral support, especially in the difficult times of E r r o r T e r m i n a t i o n.

I would like to thank my family and friends, in Canada and around the world, who supported me even from across the great Atlantic pond. Their love, friendship, and support were the factors that helped me to move forward.

Finally, I would like to thank a special person who helped me to keep my eyes on the road and reach one of my life goals.

Table of Contents

List of Figures

List of Tables

List of Equations

1 Introduction

1.1 Background

Numerical human body models (HBM) are used in various scenarios including car-pedestrian impact (Silva & Ambrósio, 1999), occupant safety (Brolin *et al*., 2008; Gierczycka & Cronin, 2018; Iwamoto *et al*., 2015; Östh *et al*., 2015; Panzer *et al*., 2011), virtual surgery (Flynn *et al*., 2015; Lapeer *et al*., 2010; Sommer *et al*., 2013), forensics (Danelson *et al*., 2008), and prosthetics design (Sengeh *et al*., 2016; Vannah & Childress, 1996; Zheng *et al*., 1999). In order to obtain the most biofidelic response of computational models, it is important to base the soft tissue models on appropriate experimental data (Lewandowski et al., 2012; Östh et al., 2017; Soetens et al., 2018).

These tissues provide postural maintenance to the whole body (Östh, 2014; Winters *et al*., 1988) and protect the internal organs from injuries (Calvo-Gallego *et al*., 2018). The stiffness of soft tissues increases with deformation in a non-linear fashion (Flynn & Mccormack, 2008; Mohammadkhah et al., 2016; Sommer, 2013). Moreover, soft tissues in the human body were shown to be strain rate dependent (Limbert & Middleton, 2004; Morrison et al., 2003; Myers et al., 1998; Ottenio et al., 2015; Shapiro et al., 2014) such that the material stiffness increased with the strain rate. Soft tissue properties are an integral component of HBMs because their mechanical properties are important contributors to the behaviour of the full-scale models (Loerakker et al., 2013; Murakami et al., 2006; Östh, 2017).

Finite element HBMs can provide information which may be otherwise unavailable experimentally, e.g. soft tissue injuries or body response to a high severity car crash (Loerakker, 2013; Schwartz et al., 2015; Stitzel et al., 2005). To provide a biofidelic response, HBMs need to be assessed at the deformation rates and modes representative for a given scenario. An integral part of this process is to introduce appropriate mechanical properties at the tissue level. There is a wide range of numerical body models used for commercial and research applications. Some of the most recognized and used HBMs are THUMS (Iwamoto et al., 2012), VIVA OpenHBM (Östh, 2017), Hybrid-III (Vezin et al., 2002), and GHBMC (Gayzik et al., 2011). These HBMs were developed to recreate the behaviour of the human body during high severity impacts. This type of scenario requires the mechanical properties of the soft tissues at high deformation rates. However, deformations of the soft tissues occur also at the low deformation rates, especially during prolonged mechanical loading that may lead to a tissue damage or injury (Loerakker et al., 2010).

Therefore, there is a need for the quasi-static properties. The main contribution of this research work is development and validation of skin, skeletal muscle, and adipose tissue models in the arm indentation test under quasi-static conditions and validation of these properties in a simple arm model, which forms the basis for wider implementation in contemporary HBM.

1.2 Motivation for Research

In the current study, the term *soft tissues* refers to the following tissues in the human body: skeletal muscle, adipose tissue, and skin. These soft tissues have been tested experimentally (Alkhouli et al., 2013; Annaidh et al., 2012; Comley & Fleck, 2010b; Davis et al., 2003; Gepner et al., 2018; Lanir & Fung, 1974; Morrow et al., 2010; Myers et al., 1995; Ottenio, 2015) and numerical models have also been proposed (Bischoff et al., 2000; Engelbrektsson, 2011; Gepner, 2018; Hedenstierna et al., 2008; Morrow, 2010; Sherman et al., 2017).

Obtaining the mechanical properties of soft tissues; however, may be challenging. The response of the soft tissue to tensile or compressive loading may be affected by a number of factors, such as dimensions of the sample (Simms et al., 2017), age of the donor (Eby et al., 2015; Faulkner et al., 2007; Shuster et al., 1975), or condition of the sample (fresh or thawed) (Gottsauner-Wolf et al., 1995; Wheatley et al., 2016a). Another method of obtaining mechanical properties of the soft tissues is *in-vivo* testing performed on volunteers (Carvalhais et al., 2013; Dhaliwal et al., 2002; Dordević et al., 2011; Iivarinen et al., 2011; Krašna et al., 2017; Maganaris, 2002; Pamuk et al., 2016; Vannah, 1996). Due to ethical reasons, this type of testing can be only performed in a non-injurious manner. Testing on human volunteers usually involves quasi-static and low deformation rates (Clemen et al., 2017; Jacquet et al., 2017; Vannah, 1996). This approach is most relevant to the current study, as the quasi-static indentation of the human upper arm was addressed. One limitation of *in-vivo* testing is that the provided response is the combination of all tissues within the investigated system. For example, an indentation test on the arm (Clemen, 2017) incorporates the response of skin, adipose tissue and skeletal muscle. It is not possible to obtain the response of a single tissue as it constantly interacts with other surrounding tissues. In order to analyze and describe the mechanical properties of the particular tissues, experimentalists turned towards the testing of excised animal tissues (Bekmez et al., 2014; Böl et al., 2014; Comley & Fleck, 2009; Grasa et al., 2011). However, certain physiological and chemical dissimilarities between animal and human tissues may also lead to mechanical differences (Stokes et al., 2013;

Tirrell et al., 2012). Another way of obtaining the experimental response of the human tissue is to use Post Mortem Human Subject (PMHS) tissue testing; however, the tissue donors are often elderly and the measured response of the soft tissues may differ from a younger population. The average value of the water content in a living person is approximately 70%. This number decreases to 50% in elderly subjects, leading to increased stiffness of the soft tissues and may also explain, in part, the higher injury rates observed in the elderly population (Schmitt et al., 2019).

Very often, scientific literature reports experimental data and models of a single soft tissue under tensile or compressive modes of loading. These are highly valuable sources of information on a single tissue level. However, the single tissue models do not inform about the joint contribution and interaction between all soft tissues on the behaviour of a more complex model (e.g., arm indentation, calf impact). An ideal scenario would involve the analysis of an *in-vivo* subject using medical imaging techniques (i.e. MRI or CT) to display the interactions between particular tissues. This study builds on the experimental data measured for individual soft tissues reported in the literature and assesses the influence of the soft tissues in the arm indentation scenario under quasi-static conditions.

1.3 Aim and Objectives

The main goal of this study was to bridge the experimental data on biomechanical properties of the skeletal muscle, skin, and adipose tissue in the human body with finite element modelling thereof. This aim was achieved by providing numerical models of the soft tissues based on the accurate experimental data. Moreover, by doing so, this study also investigated the contribution of particular tissues to their integrated response in the arm model.

The main aim of this study was achieved by following the list of objectives. In the initial stage, the literature review on the mechanical properties of the skeletal muscle, skin, and adipose tissue was performed. All these tissues are non-linear, strain rate dependent, and nearly incompressible. However, the detailed mechanical properties are different for each tissue stemming from their physiological structure. Another objective was to identify the existing constitutive models capable of representing the behaviour of the soft tissues. Numerical modelling in this study was performed in a commercial finite element analysis code (LS-DYNA, LSTC, Livermore, CA), widely used for analyzing HBMs in impact scenarios (Gierczycka, 2018; Khor, 2018; Östh, 2015). To establish a baseline for accurate soft tissue models, the behaviour of the soft tissues within the quasi-static

regime is investigated in the current study, thus providing a starting point for the future of soft tissue modelling. Potential constitutive material models incorporated in the FE code were identified and assessed. Next, the material properties from the literature were implemented in the selected models. These properties were obtained from the reviewed literature sources. Models that provided the response closest to the experimental data were identified for implementation in the arm model and assessed in the indentation loading scenario. Finally, the simulation response was compared to the experimental results.

1.4 Document Organization

Chapter two of this thesis reviews the physiology of three main types of soft tissues in the human body: skeletal muscle, skin, and adipose tissue. This chapter also discusses the mechanical properties of each tissue and experimental methodologies used to obtain this data. Based on the latter, this chapter also covers the existing experimental data which was used in this study. This section also provides background information on the existing models of soft tissues. Finally, this chapter discusses the upper arm indentation test, which pertains to the area of interest of this thesis.

Chapter three discusses the methodology. The first section identifies the mechanical properties of the soft tissues based on the literature review. This section also describes the constitutive model identification and appropriate single element test cases. This chapter also discusses the simulation setup and boundary conditions used to represent the experimental setup. Lastly, the mesh refinement study is described.

Chapter four discusses the results obtained for the single element test cases, arm indentation test, and test refinement study.

Chapter five presents the discussion of the results and the effects of different boundary conditions on the outcome of the simulation.

Chapter six summarizes the outcomes of this study, provides conclusions and proposes paths for future investigation and development.

2 Background

2.1 Anatomy and Physiology of the Soft Tissues in the Human Body

The term *soft tissues* encompasses a variety of tissues in the human body, such as muscle, adipose tissue, skin, ligaments, tendons, blood vessels, and nerves. These tissues protect and support internal organs, transport fluids and transmit neural signals (Standring 2008, Hansen 2010). However, the current study specifically focuses on the mechanical behaviour of the skeletal muscle, skin, and adipose tissue. Therefore, in the present study, the term *soft tissues* refers to the three aforementioned tissue types.

2.1.1 Skeletal Muscle

There are three muscle types present in the human body: cardiac, smooth and skeletal muscles (Hansen, 2010; Östh, 2014; Standring, 2008). Cardiac muscles are present in the heart and proximal portions of the great vessels. Smooth muscles line various organs and the walls of most blood vessels (Hansen, 2010; Standring, 2008). Skeletal muscle, also known as striated muscle, is the most abundant muscle type within the human body (Souza & Gottfried, 2013; Standring, 2008). This type of muscle is responsible for locomotion and postural maintenance (Dibb et al., 2013; Hernández-Gascón et al., 2013; Muggenthaler et al., 2006; Rehorn et al., 2014; Wheatley, 2016a; Winters, 1988).

A skeletal muscle is a complex anatomical entity connecting usually two points, origin and insertion, located on the adjacent bones. The origin is a muscle attachment proximal or medial to the centre of the human body. The insertion is the muscle attachment which is distal or lateral (Hansen, 2010; Standring, 2008; Vizniak, 2010). Two main functions of a skeletal muscle are to move bones at their joints (Standring, 2008; Vizniak, 2010) and provide postural support (Iwamoto, 2012; Mortensen et al., 2018; Ólafsdóttir et al., 2015; Siegmund et al., 2003; Siegmund & Blouin, 2009).

At the macroscopic scale, the muscle consists of a belly and a tendon (Figure 2-1). The latter part connects the belly with a bone. On the outside, the skeletal muscle is covered by epimysium, connective tissue which protects the muscle against friction from adjacent organs, e.g. other muscles and bones. On the inside, the belly of the skeletal muscle is a complex entity with a hierarchical structure. The muscle contains several fascicles (this number varies between the

muscles). Fascicles are bundles of muscle fibres, which are encased by perimysium. A closer look at the single muscle fibre shows that it is comprised of myofibrils. These myofibrils contain two overlapping types of filaments: actin and myosin. The latter are repeated in units called sarcomeres and are the basic functional unit of the muscle fibre. Myofibrils are oriented longitudinally along the muscle fibres, which is crucial for the force developed by a skeletal muscle (Hansen, 2010; Standring, 2008).

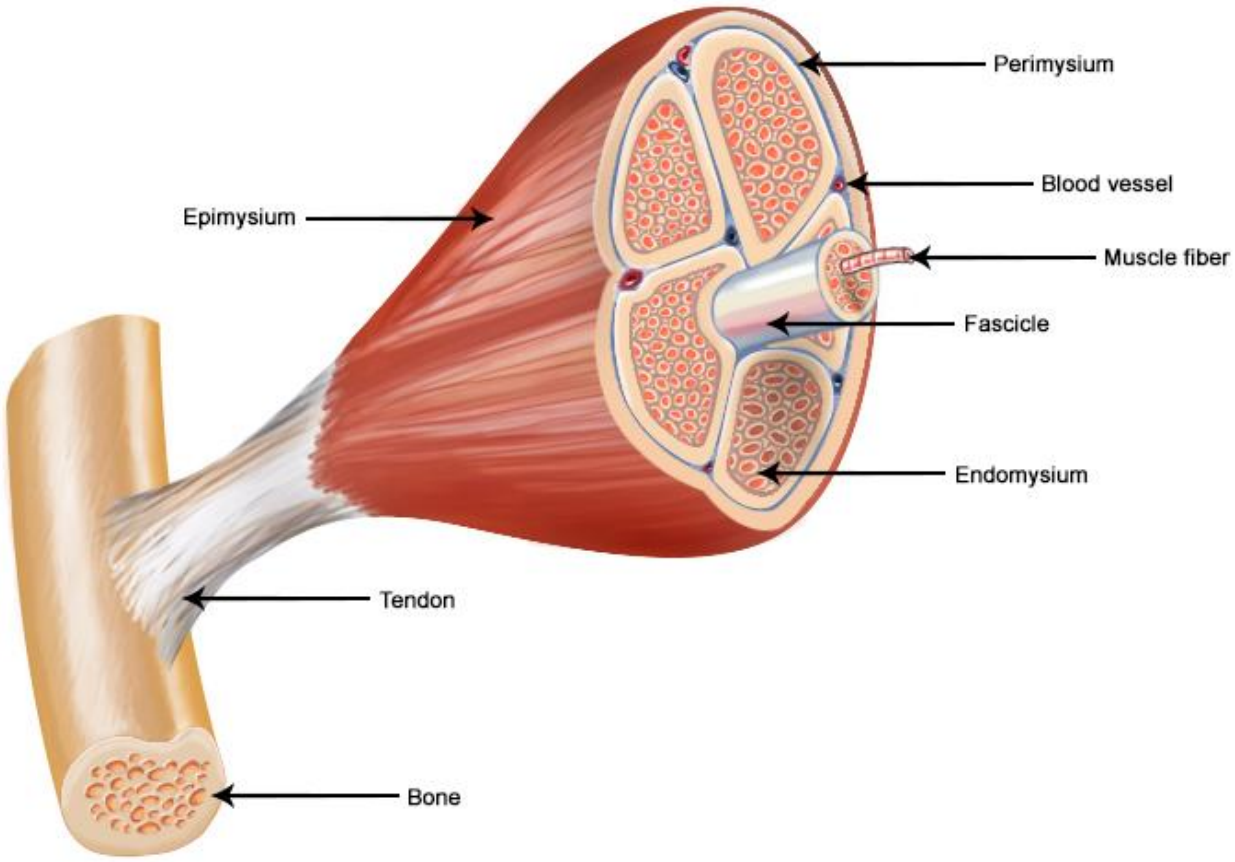

Figure 2-1. The structure of a skeletal muscle. Adapted from: SEER Training Modules, Structure of Skeletal Muscle. U. S. National Institutes of Health, National Cancer Institute. Accessed: 11th of April 2018 <https://training.seer.cancer.gov/>.

2.1.2 Skin

Human skin is the outer most tissue of the human body. It constitutes 15-20% of the human body mass, which makes it the largest single organ of the human body. It is a multi-layered membrane covering and protecting the deeper tissues (Standring, 2008). Three layers are distinguished in the skin: epidermis, dermis, and hypodermis (Ní Annaidh et al., 2012). The epidermis consists of two layers: *stratum corneum* and the viable epidermis. The dermis is mainly comprised of elastin and

collagen surrounded by ground substance and water. The hypodermis contains adipocytes within the connective tissue (Lamers et al., 2013). Each of the layers contributes to the typical stress-stretch behaviour of the skin (Figure 2-2). In the initial stretching phase, the response of the skin demonstrated low stiffness (Phase I). This is caused by the crimped collagen fibres. Once the collagen fibres begin to uncrimp, the response stiffens (Phase II). In the final phase, the collagen fibres are fully extended and aligned, thus providing the highest stiffness (Phase III) (Joodaki & Panzer, 2018).

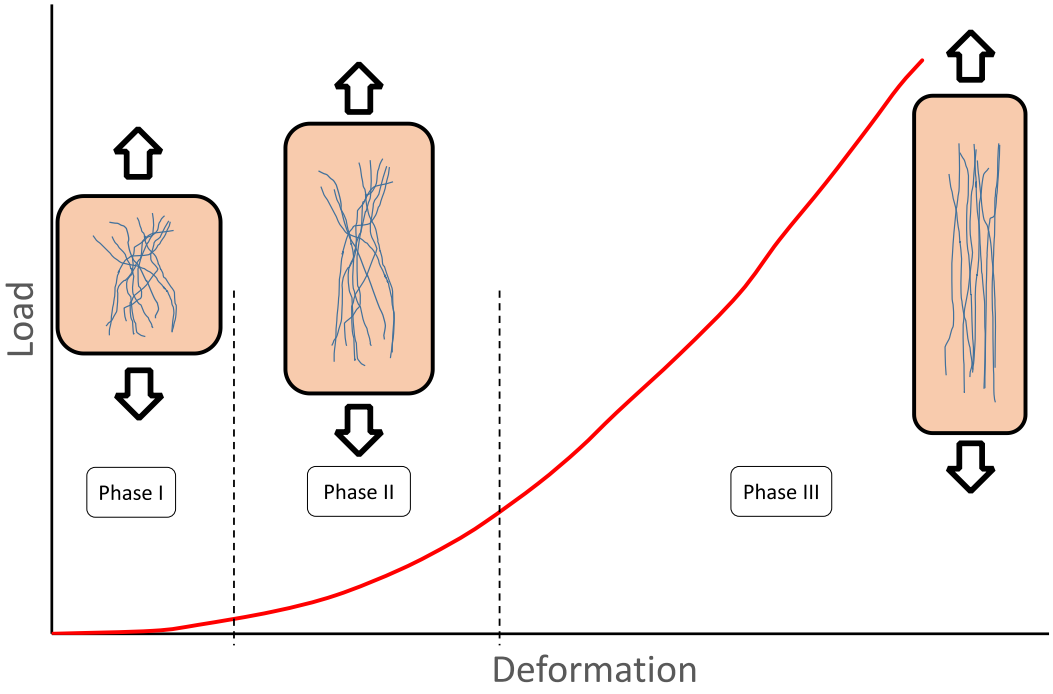

Figure 2-2. Three phases of the tensile response of the skin

2.1.3 Adipose Tissue

Adipose tissue (AT) is one of the connective tissues in the human body. In some references, this tissue is also referred to as *flesh* (Kleinbach et al., 2017; Panzer, 2011; Ruan et al., 2008). The AT is a soft connective tissue which is located beneath the dermis (Comley & Fleck, 2010a). In the human body, the AT is responsible for a number of tasks. It works as thermal insulation, absorbs shocks and impacts, stores energy, as well as covers the underlying muscles (Comley, 2010a). The percentage of this tissue in the human body depends on the age, sex, and level of fitness. However, on average it is 25-30% of the body weight.

An increased amount of AT in the human body leads to different levels of obesity. Depending on the obesity level, the risk of injury during car impact may change. Jehle reported a dependency between the body mass index (BMI) of the car occupant and the risk of injury/death. BMI is calculated as body weight in kilograms divided by square of height in square metres:

$$BMI = \frac{body\ weight}{height^2}\ (\frac{kg}{m^2})$$

The risk of injury increases for moderately obese (35 < BMI < 40), morbidly obese (BMI ≥ 40) and underweight drivers (BMI < 18.5); whereas it decreases for overweight drivers (25 < BMI < 30) (Jehle et al., 2012). A similar observation was reported by Joseph et al. (2017). These reports have shown that AT has an influence on the response of the human body during car impacts. Therefore, it is important to study the mechanical properties of the AT.

2.2 Mechanical Properties of the Soft Tissues in the Human Body | Experimental Data

The experimental data on the soft tissue properties were obtained from the relevant literature. Alongside the mechanical properties, the responses of the tissues to mechanical testing were collected. The latter included stress-strain and force-displacement curves. This study also considered the existing Full HBM developed by the Global Human Body Models Consortium (GHBMC) (Gayzik, 2011). GHBMC is a state-of-the-art HBM incorporating many details of the human body, including the geometry and material properties of the organs in the human body. The experimental data retrieved from the literature were also compared with the material models proposed in the GHBMC HBM.

2.3 Properties of the Skeletal Muscle

Numerical human body modelling finds application in many fields, with the emphasis on body behaviour in car accidents (Gierczycka, 2018; Östh, 2015). To provide a biofidelic response of the whole body model, all the components should be based on the experimental data. Therefore, it is crucial to obtain the mechanical response of the passive muscle tissue that is representative of the modelled scenario. Response may depend on the sample dimensions (Simms, 2017), sample geometry (Böl et al., 2012), subject species (Mohammadkhah, 2016), time post-mortem (Böl et al., 2016), and freshness of the sample (freeze/thaw cycle) (Gottsauner-Wolf, 1995). Moreover, studies have shown that the AT can infiltrate the skeletal muscle tissue, thus influencing the mechanical properties of the muscle tissue (Goodpaster et al., 2000). The experiments have been

performed on human tissue (Then et al., 2012), as well as on animal tissue: porcine, bovine, murine, and chicken (Mathur et al., 2001; Mohammadkhah, 2016; Van Loocke et al., 2006). Although humans and the aforementioned animals are mammals, the composition of muscle tissue varies between different species. Stokes et al. (2013) have reported an interesting observation: based on microbial activity and patterns of soil decomposition they found that ovine tissue was most similar to human tissue in many chemical parameters, e.g. nutrient composition. However, there is no reported experimental data on the mechanical properties of ovine muscle tissue. As described above, methodologies used by the experimentalists vary, therefore, the experimental responses may differ.

Measurements of the muscle density reported in independent studies were consistent (Table 2-1). The results demonstrated that the density of the muscle is approximately the same as the density of water (ρ_{water} = 1000 kg·m^{-3}).

Muscle density (kg m^{-3})	Source
1060	(Urbanchek et al., 2001)
1060	(Richmond et al., 2001)
1000	(Nordez & Hug, 2010)

Table 2-1. Density of skeletal muscle

The bulk modulus of the skeletal muscle tissue describes the resistance of the tissue to the compressive loading. Independent studies reported inconsistent values of the bulk modulus (Table 2-2).

Bulk modulus (GPa)	Source
1.00	(Chawla et al., 2009)
0.00002	(Takaza et al., 2013)
0.25 - 0.49	(Saraf et al., 2007) *cardiac muscle

Table 2-2. Bulk modulus of the muscle tissue

Provided the correct values of the sound speed in the muscle tissue, shear modulus of the muscle, and the density of the muscle, the accurate value of the muscle bulk modulus can be calculated (Equation 2-1).

$$C = \sqrt{\frac{\kappa + \frac{4}{3}G}{\rho}}$$

C – the speed of sound in the medium

κ – bulk modulus

G – shear modulus

ρ - density

2-1. Speed of sound in the muscle tissue

Marsh (2016) identified and reported the soundwave speed in the skeletal muscle as a function of the body temperature. The temperature of the human body equals T = 37°C. Marsh measured the speed of sound in the muscle tissue at this temperature as C = 1592 $m \cdot s^{-1}$. To assure biofidelity of the model, this value of the wave speed was selected and used in further research. Nordez and Hug (2010) reported the value of the muscle shear modulus at G = 11.3 kPa. Urbanchek (2001) reported the density of the muscle at 1060 $kg \cdot m^{-3}$. Using the provided properties, the bulk modulus of the muscle tissue was calculated.

$$\kappa = \rho C^2 - \frac{4}{3}G = 2.69\ GPa$$

It can be observed that the bulk modulus calculated in this study (2.69 GPa) is higher than the values reported in the literature (Table 2-2). This can be attributed to the oversight exhibited in the experimental studies.

2.3.1 Animal Muscle Testing

The most common modes of loading employed to test the muscle tissue are tension and compression. Usually, a cubic sample of the muscle tissue is excised from an animal and then tested. In order to overcome the limitations of the *in-vivo* human testing, the experimentalists use animal subjects. One of the common methods is the *ex-vivo* muscle testing. In this type of test, muscle is only partially excised from the animal. The muscle origin remains attached to the body, thus allowing the flow of the capillary fluids within the muscle. In contrast, the insertion of the muscle is dissected and attached to a testing mechanism. Then, the muscle is being tested and the responses are collected. This type of experiments allows for obtaining measurements closest to the *in-vivo* conditions.

2.3.2 Factors Affecting Muscle Response

Some experimentalists perform experiments on the samples immediately post mortem, whereas others freeze the samples first and store them for later investigation. However, the latter approach may significantly affect the response. First, the tensile strength of a muscle decreases immediately due to the post-mortem autolysis. This process is augmented by the standard freeze/thaw procedure. Gottsauner-Wolf at al. (1995) reported those observations based on the experiments performed on the extracted canine supraspinatus bone-muscle-bone segments. Some specimens were tested immediately after the extraction, whereas others were frozen and then thawed first. Ultimate tensile stress was 41.2% lower in the freeze/thaw samples. Usually, the frozen muscle tissues are stored at the temperature of -20° C (Böl, 2016). Whereas the storage between -15° C and -60° C leads to the formation of ice crystals which damage the muscle tissue (Gottsauner-Wolf, 1995; Ralis, 1989). Gottsauner-Wolf at al. stated even that one could not expect to obtain representative data if muscle was frozen and thawed (Gottsauner-Wolf, 1995). Yet still, many researchers have performed their experiments on the frozen/thawed tissues (Abraham et al., 2013; Chawla, 2009; Gras et al., 2013; Morrow, 2010; Nagle et al., 2014). Alternatively, some researchers have experimented on freshly excised PMHS muscle tissues in order to avoid *rigor mortis* (Eby et al., 2013; Takaza, 2013; Van Loocke et al., 2009; Wheatley et al., 2016b).

Another factor important to consider the mechanical testing of the muscle is the anisotropy of this tissue. Due to the fibre reinforcement of the muscle tissue, the response will vary based on the direction of the applied load. Therefore, tensile experiments were performed in two main directions: along the muscle fibres (0° from the fibre direction) and in the direction transverse to the muscle fibres (90° from the fibre direction, or cross-fibre).

Muscle testing may also vary due to the way a sample was prepared for testing. Mostly, the tissue is extracted, cut into a cube, and then tested (Böl, 2016; Takaza, 2013; Van Loocke et al., 2008). However, some references report that the whole muscle was used for experiments (Calvo et al., 2010; Eby, 2013; Grasa et al., 2016). This difference influenced the recorded response. The differences between responses of a full muscle and a muscle sample stem mainly from the physiology of the muscle tissue. In the full muscle, the fibres, and connective tissues remain intact, and no muscle fluid exudation occurs, whereas in the muscle sample the fibres and other

connective tissues are dissected which decreases the integrity of the tested sample and the muscle fluid exudes from the excised sample.

2.3.3 Importance of the Sample Dimensions

Most of the experimental data were collected from excised cubic muscle samples with a characteristic dimension of 10 mm (Böl, 2016; Mohammadkhah, 2016; Morrow, 2010; Van Loocke, 2009). However, a recent study has proven that the sample dimensions may affect the response (Simms, 2017). The situation is different in the case of biological tissues, especially skeletal muscle tissue. Muscles display hierarchical structure. They consist of muscle fibres and connective matrix, as well as fluid, which is an intrinsic part of the muscle. Moreover, some of the fibres end intrafascicularly (Sharafi & Blemker, 2011). All those factors make the skeletal muscle highly non-homogenous. Simms investigated the influence of the physical sample dimension on the stress-stretch response of the muscle tissue (Simms, 2017) and noted that the dimensions of the physical sample played an important role in the stress-stretch response. The size effect was attributed to the higher amount of intact fascicles in the larger samples that are known to affect the passive muscle mechanical properties. Moreover, the amount of the fluid exudation was smaller in the larger samples, as opposed to the smaller samples. These two factors contribute to the higher stress response of the larger samples (Simms, 2017). Based on these observations, it seems preferable to use data taken from the larger samples or full muscles. Yet, the importance of the sample dimension is only a recent discovery, therefore there are not many studies available acknowledging this effect. Therefore, although a sample 10x10x10 mm in size may not be highly representative of a full-sized muscle, this is how the majority of the experiments were carried out and one has to work with the available data.

2.3.4 Tensile Tests on Muscle Tissue

Eby et al. worked on the validation of shear wave elastography in the muscle. They used whole porcine brachialis muscle specimen elongated at a constant strain rate 0.0115 s^{-1}. The stress-stretch response was reported along the fibre direction (Eby, 2013). Takaza tested the porcine muscle in the fibre and cross-fibre directions, at three high strain rates: 116, 220, and 378 s^{-1}. Nie et al. tested porcine muscle tissue over the wide range of strain rates: 0.05, 0.4, 700, 1400, and 2100 s^{-1}. The response of the muscle was reported stiffer in the cross-fibre direction than along the fibres. This was observed for all strain rates (Nie et al., 2011). Morrow tested the *extensor digitorum longus*

(EDL) rabbit muscle in three different scenarios: tension along the muscle fibres, extension in the cross-fibre direction, and shear in the longitudinal direction. Tests were performed at a quasi-static rate of 0.0005 s^{-1}. This paper reports an interesting observation that the response in the fibre direction was stiffer than the response in cross-fibre direction (Morrow, 2010). This is opposite to what was reported by other sources. Mohammadkhah performed a comparative study between chicken and porcine fibre tissue for both fibre and cross-fibre direction. The cross-fibre response of the porcine tissue was the stiffest of all the samples, whereas the response of the porcine tissue in the fibre direction was the most compliant. The chicken tissue presented a similar trend: response in the cross-fibre direction was stiffer than in the fibre direction (Mohammadkhah, 2016). Rehorn measured the influence of the strain rate on the peak stress response of the murine muscle tissue. Tests were performed at a wide range of strain rates, i.e.: 0.1-10 s^{-1} and confirmed strain rate effect: the stiffness of the muscle increased with the strain rate. However, the greatest influence of the strain rate on the muscle stiffness was observed in the lower speed regime, i.e.: 0.1-3 s^{-1} (Rehorn, 2014). The research presented by Calvo was two-fold. In the first part, rat *Tibialis Anterior* (TA) was tested *in-vitro*. In the second part, the muscle-tendon unit was tested *ex-vivo*. In both cases, the samples were stretched along the fibre direction (Calvo, 2010). Myers experimented on passive muscle from rabbits using a partially excised TA muscle, maintaining the connection of the muscle at the origin (*ex-vivo* condition). The muscle was extended at three different strain rates: 0.44, 4.44, and 11.1 s^{-1}. It was observed that the stiffness of the muscle increased with the strain rate (Myers, 1998). The same experiment was later recreated by Hedenstierna *et al*. Their results corroborated with those reported by Myers (Hedenstierna, 2008). A summary of the experimental responses is presented in Figure 2-3.

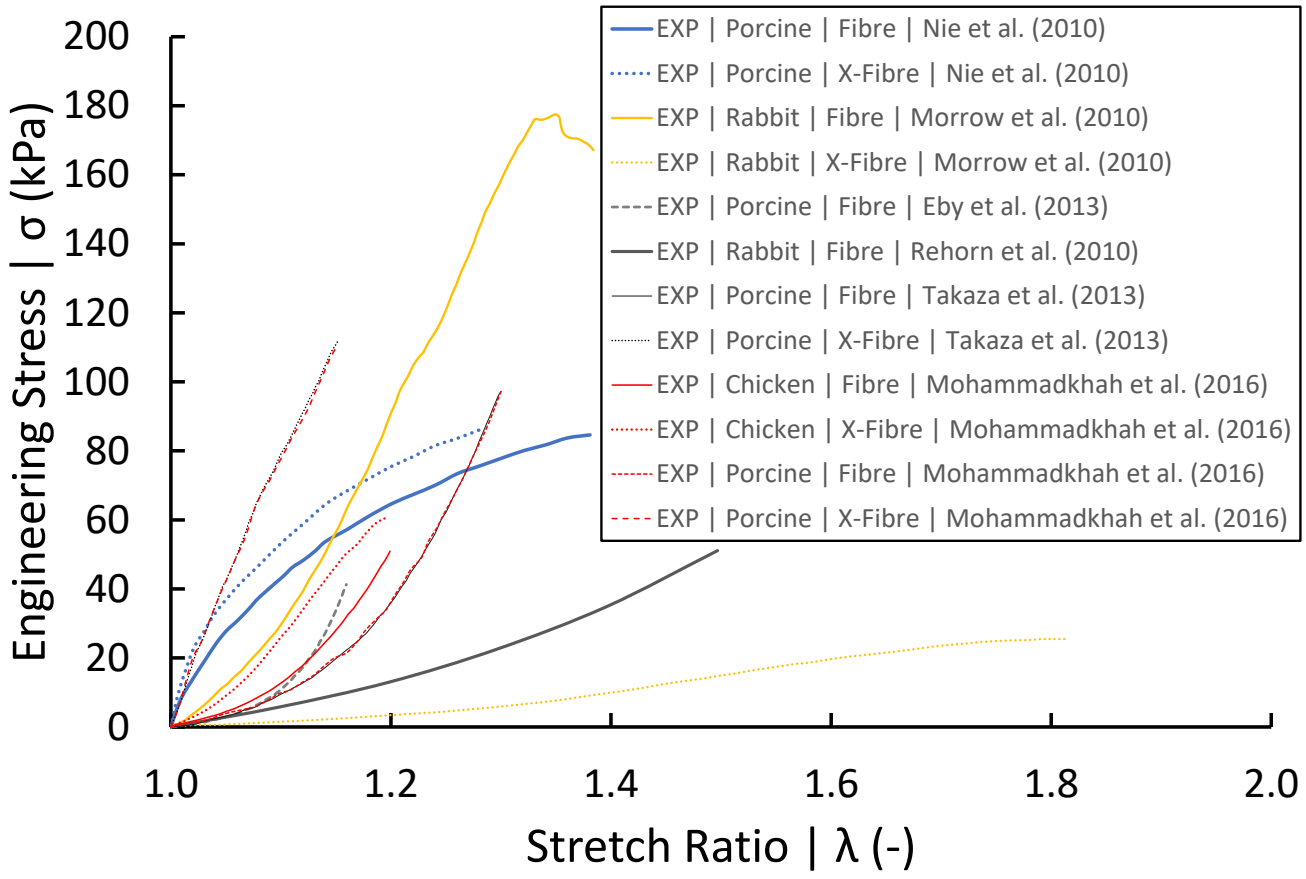

Figure 2-3. Experimental data on muscle tension at a quasi-static strain rate

2.3.5 Compression Tests on Muscle Tissue

Compression is another mode of loading used to test the mechanical properties of the muscle tissue. Muscle tissue samples were compressed along the direction of the muscle fibres (0° from the fibre direction), as well as in the transverse direction (also known as 90° from the fibre direction, or cross-fibre). Some of the experimentalists also performed tests at angles different from 0° and 90°, e.g. 45° or 60°. Böl proposed two types of compression tests: unconfined (Böl, 2012) and confined muscle samples (Böl, 2016). The literature review shows that the experiments on unconfined muscle samples are more common that the confined samples.

Van Loocke et al. performed experiments on excised porcine tissue with a nominal dimension of 10 mm for the cubic samples. The samples were compressed at strain rates ranging from 0.0005 s^{-1} to 0.1 s^{-1}. The samples were compressed at different angles: 0° (fibre direction), 45°, 60°, and 90° (cross-fibre direction). The anisotropy effects were especially observed at the lower strain rates. The response in the cross-fibre direction was stiffer than in the fibre direction. However, an

observation was reported that the anisotropy effects do not play an important role at the strain rates higher than 0.05 s^{-1} (Van Loocke, 2008). Mohammadkhah performed a comparative study between chicken and porcine fibre tissue. The muscle samples were tested in two directions: fibre and cross-fibre direction. In both cases: chicken and porcine tissue, the response in the cross-fibre direction was stiffer than along the fibres. Experimental data shows that in compression the chicken muscle provided in general stiffer response than the porcine muscle. At the highest reported strain, the response of the cross-fibre chicken sample is six times stiffer than the fibre direction porcine sample (Mohammadkhah, 2016). Böl (2012) presented two sets of muscle compression experiments. The first set consisted of rabbit muscle tissue compression in fibre and cross-fibre direction at a quasi-static rate (0.0005 s^{-1}). In the initial stretch phase between $\lambda = 1.00$ and $\lambda = 0.85$, both directions provide a similar response. Whereas, in stretches between $\lambda = 0.85$ and $\lambda = 0.70$ the cross-fibre sample becomes stiffer, as much as by factor 2.5 at the final stretch. The collection of the experimental data was assembled in Figure 2-4.

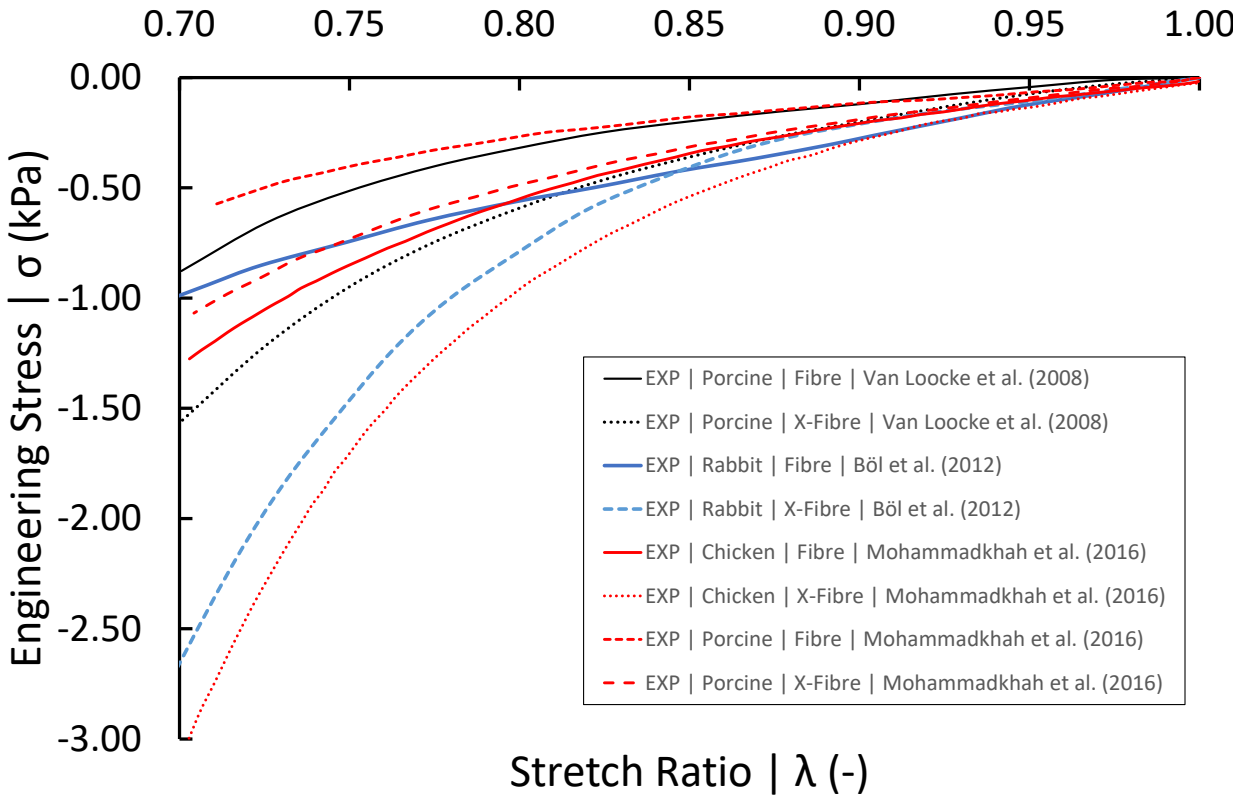

Figure 2-4. Experimental data on muscle compression at a quasi-static strain rate

2.4 Mechanical Properties of the Skin

Collagen fibres present in the skin form *Langer's lines* (Hansen, 2010). These lines describe the orthotropic behaviour of the skin under tensile testing. The response of the skin to tension in the direction parallel to the Langer's lines is different from the response to tension in the direction perpendicular to the lines (Gąsior-Głogowska et al., 2013; Ní Annaidh, 2012; Ottenio, 2015). Ridge reported the orientation of the Langer's lines in the human upper limb and torso (Ridge & Wright, 1966) (Figure 2-5).

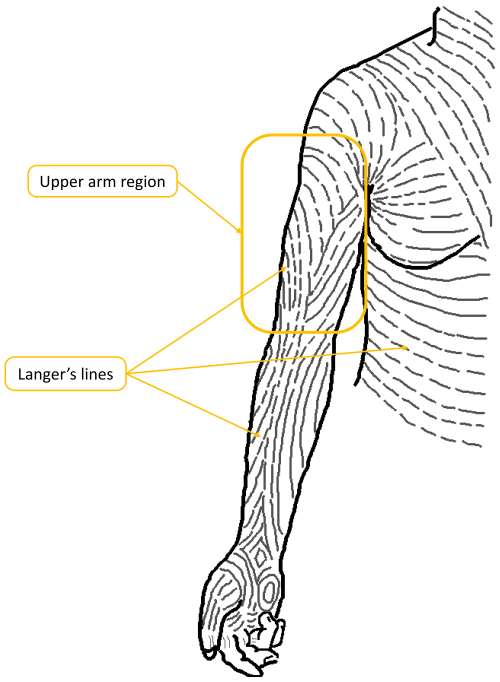

Figure 2-5. Langer's lines, orientation in the upper arm (adapted from Ridge et al., 1966)

The analysis of the stress-strain curves shows that the response of the skin can be divided into three phases (Figure 2-6). These phases depend on the behaviour of the collagen fibres within the skin tissue. In the first stretching phase (Phase I), the collagen fibres are still crimped. In most cases, their current length is shorter than the resting length of the fibres. Thus, in this state, these fibres cannot produce any tension. In the stress-stretch plot, this behaviour is represented by the initial toe region of the curve. The second phase (Phase II) includes uncrimping and engaging of the fibres to produce force. In this phase, fibres begin to extend beyond their resting length. In the stress-stretch curve, this can be identified by the nonlinear curve behaviour. This can be identified as the physiological range of motion of the skin. The final phase (Phase III) occurs when the collagen fibres are uncrimped and aligned. This phase may produce high forces, beyond the

physiological range of motion. In this phase the stress-stretch response is linear. In tensile tests, skin fails at the end of Phase III. All these phases contribute to the nonlinear response of the skin to tension (Benítez & Montáns, 2017).

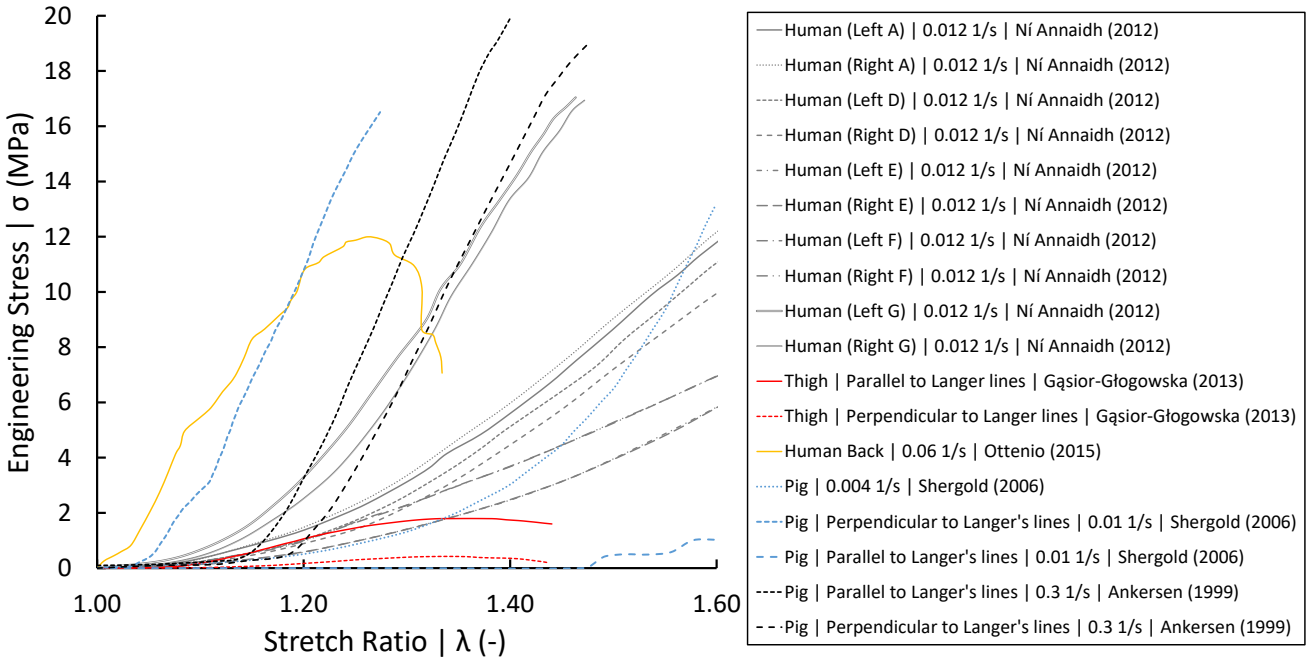

Figure 2-6. Experimental data on skin tension at a quasi-static strain rate

Ní Annaidh and colleagues (2012) have performed a series of tensile experiments on the human skin excised from the back. Although this data set covers 56 tissue samples taken from different regions from the back of the PMHS, they have been only tested in the quasi-static conditions. Skin samples were cut into a dog-bone shape and stretched at the strain rate of $\dot{\varepsilon}$=0.012 s^{-1}. In their study, researchers reported the ultimate tensile strength (UTS), mean elastic modulus, and the mean failure strain. Those parameters can be used in the process of designing a constitutive model and a finite element model.

Gąsior-Głogowska et al. (2013) have also performed tensile experiments on excised skin tissue. In this case, samples were cut in the shape of rectangular stripes, 10×28 mm and the average thickness of t=1.5 mm. Two types of samples were prepared: (i) excised along the Langer's lines, (ii) excised perpendicular to the Langer's lines. Experiments were performed at the quasi-static rate of 0.00125 s^{-1}. Skin samples in the longitudinal direction display mechanical properties (Young's modulus

and maximum stress value), which are approximately four times higher than in the perpendicular samples.

Ottenio et al. (2015) presented experimental data on skin tensile properties including higher strain rates: 0.06, 53, and 167 s^{-1}. In their study, researchers observed that the Ultimate Tensile Stress (UTS) increases with the strain rate. Moreover, regardless of the strain rate, experimental data showed that the orientation of the Langer's lines affects the response of the skin: it was observed that samples oriented perpendicular to the Langer's lines fail at a lower UTS than the longitudinal samples. This fact confirms the anisotropy of the skin tissue.

Sherman et al (2017). performed a series of experiments on the rabbit skin. Tensile tests at two strain rates were reported: 0.001 and 0.1 s^{-1}. Similar to the previously described studies, in this case also two directions of the skin were tested: parallel and perpendicular to the Langer's lines. These results follow the general trend observed in tensile skin testing. First, there was an extended toe region where stress remained at a low level (Phase I). The next phase (Phase II) followed an exponential-like trend. The last phase showed the linear stiffening of the response (Phase III). The authors reported this type of response for all tested samples, at both strain rates and for both tested directions.

Experimental measurements show that the skin thickness varies across different parts of the human body (Reihsner et al., 1995). Skin thickness is also a highly subject-specific parameter.

Source	Body region	Thickness	SD
Gąsior-Głogowska et al. (2013)	thigh	1.50	–
Ní Annaidh et al. (2012)	back	2.00	–
	forearm (i)	1.51	0.07
	forearm (o)	1.5	0.2
	upper arm (i)	1.14	0.2
	upper arm (o)	1.8	0.2
	shoulder	3.07	0.5
	sternum	1.86	0.3
	upper back	3.5	0.8
	abdomen	1.95	0.1
Reihsner et al. (1995)	lower back	2.54	0.3
	thigh (i)	1.5	0.07
	thigh (o)	1.57	0.1
	patella	1.72	0.08
	hollow of the knee	1.43	0.04
	tibia	1.72	0.2
	calf	1.57	0.1
	instep	1.69	0.2
	average	1.88	0.22

Table 2-3. Skin thickness reported in the literature

Measurements of the skin density reported in independent studies were consistent (Table 2-4). The results demonstrated that the density of the skin is approximately the same as the density of water (ρ_{water} = 1000 kg·m^{-3}).

Skin density (kg m^{-3})	Source
1100	(Potts et al., 1983)
1000	(Gahagnon et al., 2012)
1000	(Pereira et al., 1991)

Table 2-4. Density of skin

2.5 Properties of the Adipose Tissue

Adipose tissue (AT) is an intrinsic part of the human body. Depending on the amount of the AT in the human body, it may have an influence on the response of the human body to different perturbations and loading scenarios. In particular, a high mass of AT in obese car occupants can change their kinematics and behaviour during the impact (Engelbrektsson, 2011; Naseri et al., 2017). Because of that, Gepner et al. underlined the importance of the shear response of the adipose tissue (Gepner, 2018). The shear response was also investigated by Sommer (2013).

Farvid (2006) measured the density of the adipose tissue *in-vivo* within the population of Caucasian non-smoking men. Comley and Fleck (2009) measured the density of the porcine adipose tissue. Martin et al. (1994) measured the density of the adipose tissue in PMHS. The values are summarized in Table 2-5. Values obtained from different research groups are consistent. The density of the AT is lower than the density of the muscle tissue.

Adipose Tissue Density (kg m^{-3})	**Source**
919.6	(Farvid, 2006)
920	(Comley, 2009)
925-970	(Martin, 1994)

Table 2-5. Density of the Adipose Tissue

Experimental data on tension and compression of the adipose tissue was presented in Figure 2-7 and Figure 2-8, respectively. It can be noted that the curvature of the orbital fat response curve is concave down (Chen & Weiland, 2011). This remains in contrast to the other types of adipose tissue.

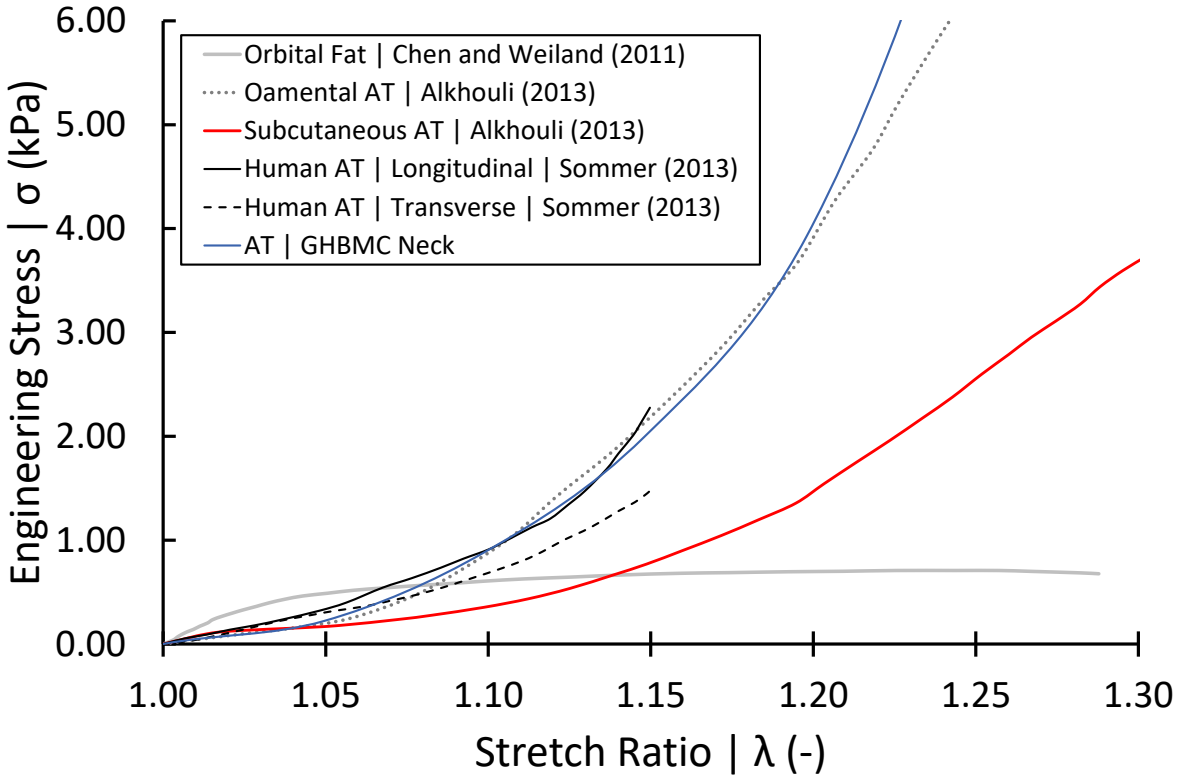

Figure 2-7. Experimental data on adipose tissue tension under quasi-static conditions

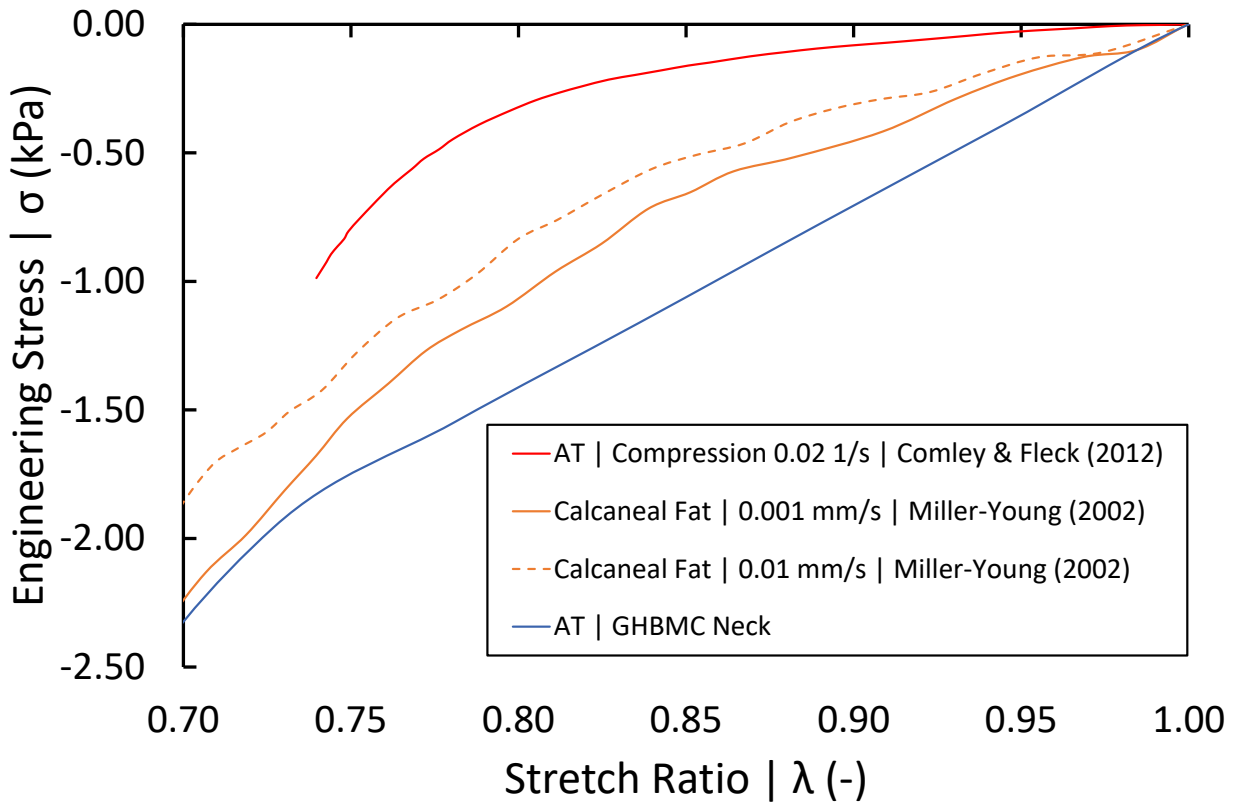

Figure 2-8. Experimental data on adipose tissue compression under quasi-static conditions

The analysis of the tension/compression response of the AT showed that the shape of the curve is similar to the shape of the skeletal muscle response. However, the response of the AT is more compliant than muscle tissue. In the low strain rate regime, the adipose tissue did not display high sensitivity to the strain rate in compression (Miller-Young et al., 2002).

2.6 The geometry of the Human Upper Arm

Human body modelling requires certain assumptions and simplifications. One of them includes the dimensions of the human body parts. A testbed developed in this study assumed the diameter of the upper arm d = 100 mm. This value is based on the average dimensions of a mid-size male (M50) (Gayzik, 2011). However, even among the population of the mid-sized males, these values may differ; therefore, it is also important to perform a study including the variability of the arm diameter. Anthropometrical measurements are presented in Table 2-6.

Source	Measurement conditions		Upper arm circumference (mm)	Diameter (mm)
NASA	relaxed		312	99.3
	flexed		332	105.7
ElMaraghy (2008)	right dominance		269.5	85.8
	left dominance		280	89.1
Ahmadi (2007)	–		258.5	82.3
Wang (2000)	–		272.9	86.9
McConville (1980)	relaxed		299.7	95.4
	flexed		321	102.2
Robbins (1983)	standing (relaxed)		298.6	95.0
	seated (flexed)		314.6	100.1
Liu et al. (2018)	LEFT	min	225.3	71.7
		mean	291.2	92.7
		max	364	115.9
	RIGHT	min	230.7	73.4
		mean	294.1	93.6
		max	373.3	118.8
Minimum			225.3	71.7
Average			296.1	94.2
Maximum			373.3	118.8

Table 2-6. Anthropometrical measurements of the upper arm circumference

2.7 Review of the Constitutive Models Used to Represent Soft Tissues

This section provides a description of constitutive models that relate stress and strain and can be used to represent the behaviour of the soft tissues. In addition, the implementation of these models with the required material parameters in LS-DYNA was briefly described (Table 2-7).

In the case of a simple linear elastic model, the stress and strain are related by the Young's (elasticity) modulus of the given material (*MAT_ELASTIC in LS-DYNA).

$$\sigma = E\varepsilon$$

σ stress
ε strain
E Young's modulus

2-2. Hooke's law for an elastic material. Stress-strain formulation.

This model is recommended to be used for a small deformation range. It is not suitable for large deformations occurring in soft biological tissues. Nevertheless, this material model was used in the current study for debugging purposes. This material is strain rate independent.

Nearly incompressible materials can be also represented by a Blatz-Ko material model. It is characterized by the shear modulus and density of the modelled material. To assure the near incompressibility of the material, the Poisson's ratio is set constant to ν = 0.463. This material model nearly symmetrical response in tension and compression (*MAT_BLATZ-KO in LS-DYNA).

An isotropic viscoelastic material is an extension of the previous material. It provides a linear response to deformation and strain rate dependency. This material is recommended for modelling of rubbers and foams (*MAT_VISCOELASTIC in LS-DYNA).

$$\sigma(t) = E_{inst}\varepsilon(t) + \int_0^t F(t-t')\dot{\varepsilon}(t')dt'$$

t	Time
$\sigma(t)$	stress as a function of time
$\varepsilon(t)$	strain as a function of time
$\dot{\varepsilon}(t)$	strain rate as a function of time
E_{inst}	instantaneous elastic modulus
$F(t)$	relaxation function

2-3. Stress developed by the viscoelastic model

A hyperelastic material model was proposed to represent the behaviour of rubbers and foams (Ogden, 1984). It allows for the representation of non-linear elastic response for rubber-like materials and is commonly used for modelling biological tissues (Engelbrektsson, 2011; Hedenstierna, 2008; Nolan et al., 2014; Shergold et al., 2006). The true stress-stretch relation is described using the following formula:

$$\sigma = \sum_{i=1}^{n} \mu_i(\lambda^{\alpha_i} - \lambda^{-0.5\alpha_i})$$

σ	true stress
λ	stretch ratio
μ	shear component
α	stiffening parameter

μ and α constitute the shear modulus:

$$2G = \sum_{i=1}^{n} \mu_i\alpha_i$$

2-4. Stress developed by the Ogden rubber model

The Ogden rubber formulation requires the μ and α parameters to be determined by fitting the response curve to the experimental data (*MAT_OGDEN_RUBBER in LS-DYNA).

The Ogden rubber formulation was used as a baseline for another hyperelastic and viscoelastic material model. However, in contrast to the original constitutive model, this model does not require fitting material constants to experimental data. Instead, a continuous tension/compression load curve can be defined to represent the behaviour of the modelled material. It is important to provide load curves over a large range of strain rates to cover the complete range of expected loading. In the case of the strain rate not specified by the curve, the model interpolates values between the available curves. The main advantage of this model is that it follows the provided load curve or set of curves. This property is useful in cases where the load curves represent high asymmetry in tension/compression and cannot be approximated by a continuous function. Further in the text, this model is referred to as *Du Bois model* (*MAT_SIMPLIFIED_RUBBER in LS-DYNA) (Du Bois, 2003).

*MAT_ELASTIC	ρ	Density
	E	Young's modulus
	ν	Poisson's ratio
*MAT_BLATZ-KO	ρ	Density
	G	Shear modulus
	ν	Poisson's ratio, constant: 0.463
*MAT_VISCOELASTIC	ρ	Density
	κ	Bulk modulus
	G_0	Instant shear modulus
	G_i	Long-term shear modulus
	β	Decay constant
*MAT_OGDEN_RUBBER	ρ	Density
	ν	Poisson's ratio
	μ_i	Shear modulus
	α_i	Hardening constant / model parameter
	G_i	Prony series relaxation shear modulus
	β_i	Relaxation constant
*MAT_SIMPLIFIED_RUBBER	ρ	Density
	κ	Bulk modulus
	μ	Damping coefficient
	LC/TBID	Load curve / table of load curves

Table 2-7. Parameters required for the material models

2.8 Existing Numerical Models of Muscle, Skin and Adipose Tissue

This section of the document describes the existing soft tissue models described in the literature.

2.8.1 Numerical Models of the Skeletal Muscle

The literature review revealed a number of numerical muscle models. This chapter describes those findings. Moreover, the main characteristics of these models were summarised in a table form (Table 2-9).

Along with the experimental data on the transverse compression of the rat muscle, Bosboom et al. (2001) proposed a material model based on the nearly incompressible Ogden rubber model. The model was based on the experimental data measured on two rats, from both hind limbs. The results were presented in Table 2-8.

Subject	TA muscle	μ [kPa]	α [-]	δ [-]	τ [s]
Rat 1	**left**	20.6	19.0	0.538	6.53
	right	19.6	17.2	0.63	6.07
Rat 2	**left**	9.32	29.8	0.498	5.50
	right	12.7	19.7	0.529	5.94
Average +/- SD		15.6 +/- 5.4	21.4 +/- 5.7	0.549 +/-0.056	6.01 +/- 0.42

Table 2-8. Ogden rubber material parameters (adapted from Bosboom et al., 2001)

The model also addressed the viscoelasticity of the muscle by implementing the viscoelastic parameters. This model followed the experimental data reported in the same paper.

In a study by Oomens et al. (2003), the authors described a model of a rat TA muscle in both: passive and active states. The passive muscle model was modelled as a nearly incompressible material. Whereas the active muscle properties were implemented with the Huxley active muscle model. The authors have developed a geometry of the TA muscle and provided model parameters. However, they did not provide a comparison of experimental data and simulation results. There is a note in the text which says that there was a good qualitative agreement between measured and computed strains, but the measured strains were higher.

An in-depth analysis of modelling was presented by Hedenstierna et al (2008). Based on the experimental data measured from the rabbit TA muscle, the authors proposed an Ogden rubber model with viscoelastic parameters. The model was based on the experimental data measured at three strain rates: 1, 10, and 25 s^{-1}. However, the experimental response covered only the muscle

in tension. Because of that, the model proposed by Hedenstierna provides a symmetrical response in tension and compression. Experimental observations reported by other sources have demonstrated that muscle response is asymmetrical in tension and compression. This can be verified with the experimental data assembled in Figure 2-3 and Figure 2-4. Therefore, even though the presented model provides a quite reasonable response in tension, the stress magnitude of the compressive response is much higher than the measured response in the muscle. This model was implemented in the commercial FE software using the hyperelastic Ogden model (*MAT_OGDEN_RUBBER in LS-DYNA).

Iwamoto et al. (2012) implemented a muscle model in LS-DYNA using the Du Bois hyperelastic model. This constitutive model allows for the input of a continuous tension-compression stress-strain curve based on the experimental uniaxial data. However, this model did not include viscoelastic effects. Moreover, the authors stated that they have used data on tension only. This fact makes the response of the model symmetrical. Which replicates the limitation found in the model proposed by Hedenstierna, that the model response in compression was too stiff.

Böl et al (2012). have proposed a muscle model used for compression of the muscle tissue. The researchers compressed the muscle tissues at three different directions: 0°, 45°, and 90°. Although the simulation response tended to resemble the experimental response, even the authors have mentioned that the simulation response was far from satisfactory, especially for the 90° (or cross-fibre) direction.

Calvo et al. (2010) proposed a muscle and tendon unit (MTU) model to recreate the *ex-vitro* behaviour of MTU. The proposed material was defined as transversely isotropic. This model provided a good fit in the tensile conditions: coefficient of determination R^2 close to 1. In a further study, Calvo and colleagues investigated the behaviour of the abdominal muscle tissue (Calvo et al., 2014). Based on the experimental results, the authors modelled the relaxation behaviour of the muscle. This model provided insight into the viscoelastic properties of the muscle tissue.

Moerman addressed the tension-compression asymmetry of the skeletal muscle. He used the modified Ogden methodology. However, the paper only reported experimental data on compression compared with the model response. The model followed the experimental data in both fibre and cross-fibre directions (Moerman et al., 2016). However, the asymmetry level was not appropriate for the one encountered in the muscle response.

Grasa et al. proposed a muscle model based on the active and passive response of the rat TA muscle *ex-vivo*. The geometry of the TA muscle was based on magnetic resonance imaging. The authors noticed an important point, that in order to obtain feasible results, the geometry of the muscle has to be accurate and resemble the geometry of the modelled part (Grasa, 2011).

Östh et al. have developed a whole body model of a 50^{th} percentile female. In their model, they implemented the passive muscle using the Ogden constitutive model (*MAT_OGDEN_RUBBER in LS-DYNA). The viscoelasticity effects were provided by the means of the Prony series (Östh, 2017).

Karthikeyan proposed a viscoelastic model to represent the skeletal muscle. It included the strain rate effects; however, the measured response of the proposed muscle model was linear, and not hyperelastic (Karthikeyan, 2009). Chawla used Genetic Algorithms to generate the best fit for muscle tissue behaviour at higher strain rates (136, 183, and 262 s^{-1}). This model proved capable of representing the muscle behaviour of single element samples at higher strain rates. However, the linearity of the model may be a limitation in the case of large deformations (Chawla, 2009).

Rehorn et al. have proposed a quasi-linear viscoelastic (QLV) model of the muscle including the behaviour of muscle fibres. The researchers also noticed that the viscoelastic behaviour of the muscle depends significantly on the velocity of the deformation, especially at lower strain rates between 0.1-3 s^{-1}. This model addressed this issue, however at the higher strain rates ($\dot{\varepsilon} > 3\ s^{-1}$) the discrepancies between predicted and experimental results were observed (Rehorn, 2014).

Based on the experimental results, Van Loocke et al. proposed a model for muscle tissue compressive behaviour. This model follows the experimental results across a range of strain rates from quasi-static to static 0.0005-0.1 s^{-1}. The model predicts the compressive behaviour well (Van Loocke, 2008).

Takaza proposed a muscle model that can be used at higher strain rates: 116, 220, and 378 s^{-1} (Takaza, 2013). The range at which the model was tested is similar to the one proposed by Chawla (Chawla, 2009). According to the authors, this muscle model may be used in bigger scale models at high severity impact scenarios.

Author	Year	Loading mode	Characteristics	Comments
Bosboom	2001	compression	fit to compression only	small size rat muscle
Oomens	2003	compression	fit to compression only	small size rat muscle
Hedenstierna	2008	tension	fit to tension only	rabbit TA muscle
Iwamoto	2012	tension	fit to tension only	
Böl	2012	compression	hyperelastic	small samples (3-6 mm), may be inaccurate
Calvo	2010	tension	hyperelastic	Full Rabbit TA MTU
Calvo	2014	tension	relaxation test	abdominal muscles
Moerman	2016	tension/compression	asymmetrical/hyperelastic	not appropriate for the muscle asymmetry
Grasa	2011	tension	hyperelastic	rat TA muscle
Östh	2017	N/A	linear, elastic	
Karthikeyan	2009	compression	linear	
Chawla	2009	compression	linear	
Rehorn	2014	tension	hyperelastic	single fibres tested
Van Loocke	2008	compression	hyperelastic	fresh sample, before *rigor mortis*
Takaza	2013	tension	hyperelastic	fresh sample, before *rigor mortis*

Table 2-9. Main characteristics of muscle models

2.8.2 Numerical Models of the Skin Tissue

THUMS is an HBM with human geometry and material parameters. The skin in THUMS was implemented using the linear elastic material model. This model was assigned Young's modulus of 22.02 MPa and Poisson's ratio of 0.45 (Iwamoto, 2012). A similar approach was used in the OpenVIVA model. The linear elastic model was used, with Young's modulus of 1 MPa and Poisson's ratio of 0.40 (Östh, 2017). This material is strain-rate independent, therefore it does not address the non-linearity and viscoelasticity of the skin tissue. Skin tissue in the GHBMC HBM was implemented with a linear viscoelastic model (Gayzik, 2011). This model provides the strain rate effects, but the response is linear, which does not address the hyperelasticity of the skin.

2.8.3 Numerical Models of the Adipose Tissue

Engelbrektsson investigated a set of material models appropriate to model the adipose tissue: *MAT_OGDEN_RUBBER, *MAT_SOFT_TISSUE, *MAT_SIMPLIFIED_RUBBER, and *MAT_VISCOELASTIC (Engelbrektsson, 2011). Based on the performed research, the author proposed to use the Ogden rubber formulation with strain rate effects. This implementation allowed to recreate the experimental behaviour of the adipose tissue observed by the author. However, this particular fit covered only low and intermediate strain rates.

Sommer performed tensile and shear experiments on the abdominal human adipose tissue (Sommer, 2013). The authors proposed constitutive parameters for which the model followed the experimental curves.

Naseri performed two types of experiments on the adipose tissue: rheometer and ramp test (Naseri, 2017). The experimental results from shear tests were used to formulate a viscoelastic material model describing the behaviour of the adipose tissue for three strain rates: 0.01, 0.1, and 1 s-1.

Gepner investigated the adipose tissue in a shear loading test (Gepner, 2018). The authors identified the shear response of the adipose tissue as an important factor influencing the kinematics of obese car occupants.

The THUMS HBM used the linear viscoelastic model to represent the adipose tissue. This model is strain rate dependent, but the response is linear, which does not take the hyperelasticity of the adipose tissue into account (Iwamoto, 2012).

The Open VIVA F50 HBM is an open-source project which represents the geometry and material properties of a 50th percentile female in the FE environment (Östh, 2017). The material model of the AT used in this HBM was based on the discoveries made by Engelbrektsson. Therefore, the AT is modelled with the hyperelastic Ogden model (Engelbrektsson, 2011).

The GHBMC body model uses the hyperelastic Du Bois model to represent the hyperelastic behaviour; however, this model does not take the strain rate effects into account (Gayzik, 2011).

2.9 The GHBMC Human Body Model

The Global Human Body Models Consortium HBM is the state-of-the-art model representing a human body in the finite element environment. The geometry of the model was based on the posture of a young male (26 years old) of average size (78.6 kg weight, and 174.9 cm height), 50th percentile of the male population (referred to as M50 model) (Gayzik, 2011). It also consists of the geometry of the internal body organs, as well as the material properties of the tissues in the body. The GHBMC body model consists of material models developed for hard and soft tissues (Figure 2-9).

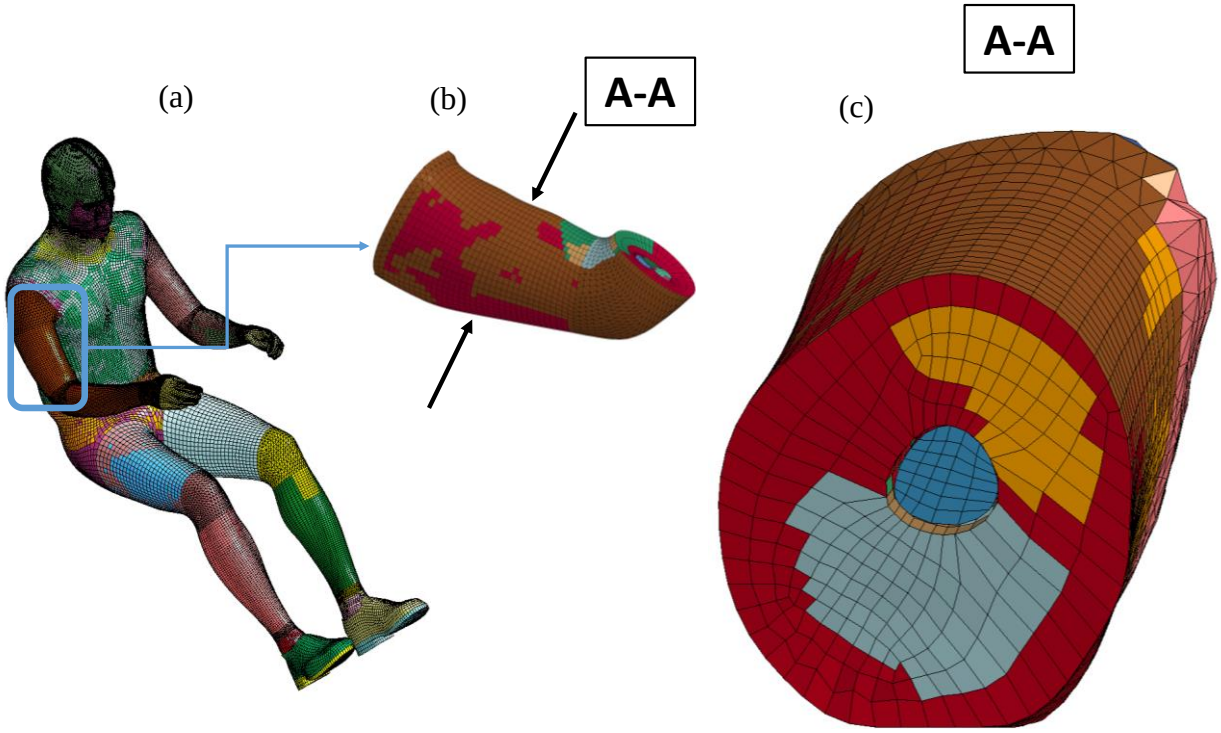

Figure 2-9. (a) Full GHBMC Body Model; (b) GHBMC arm model; (c) cross-section of the GHBMC arm model

Mechanical properties of skin, skeletal muscle, and adipose tissue were summarized in Table 2-10 Material properties of the muscle tissue for the GHBMC HBM were based on the literature (Karthikeyan, 2009).

	Skeletal muscle	**Skin**	**Flesh**
Material model	*MAT_VISCOELASTIC	*MAT_VISCOELASTIC	*MAT_SIMPLIFIED_RUBBER
Density (kg/m^3)	1000	1000	1060
Poisson's ratio	–	–	0.3
Bulk modulus (GPa)	0.00329	2.0	2.0
Shear modulus (GPa)	G_0 = 5.10E-5; G_i=2.60E-5	G_0 = 5.431E-3; G_i=1.086E-3	–

Table 2-10. GHBMC material properties of the soft tissues

Each soft tissue is represented by a different material model. Not all material properties required by those models are shared. Therefore, a parameter may be specified for one tissue and not for the other.

The upper arm segment in the GHBMC HBM consists of bone, skeletal muscle (bicep and triceps muscles), skin, and adipose tissue (Figure 2-10).

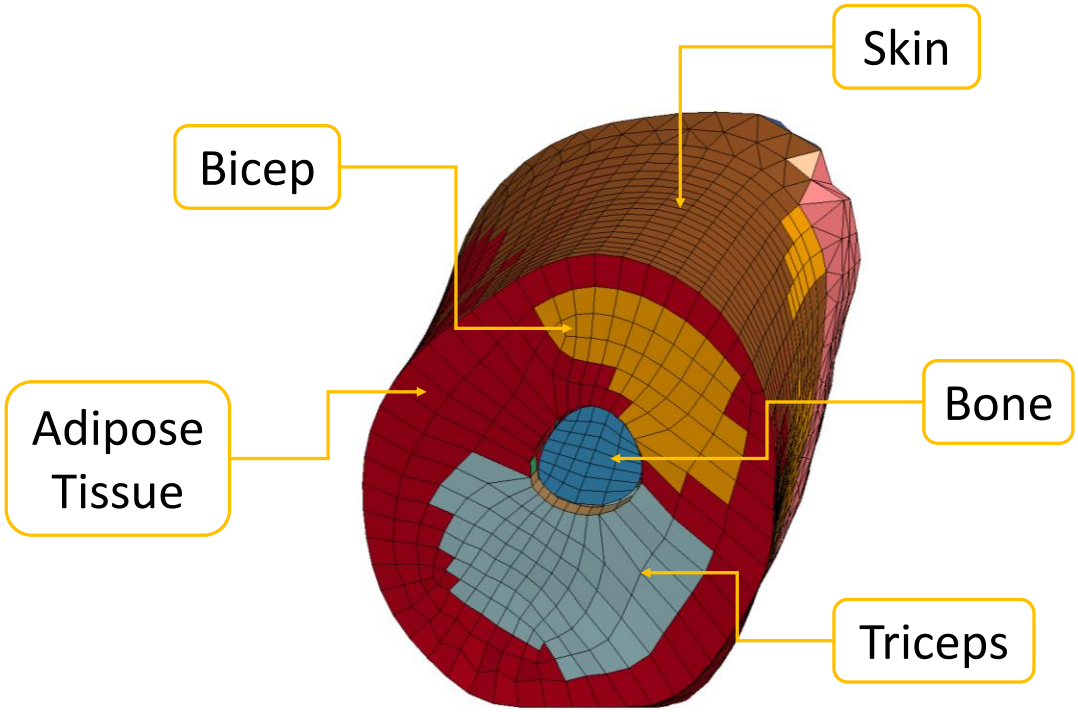

Figure 2-10. Cross-section of the GHBMC arm model

In the GHBMC model, adipose tissue is referred to as *flesh*. Properties of the soft tissues in the upper arm segment followed those from the whole human body (Table 2-10).

2.10 Experimental Studies on Soft Tissue Indentation *in-vivo*

Transverse indentation of muscle at quasi-static strain rates can provide insight into the behaviour of the muscle and surrounding tissues (adipose tissue and skin) *in-vivo*. This section of the document covers the indentation experiments performed *in-vivo* on human volunteers.

Vannah and Childress performed a series of *in-vivo* experiments to estimate the stiffness change among multiple subjects, with and without muscle activation (Vannah, 1996). Tests have been performed using a special setup, which supported the buttocks, knees and feet. The tip of the indenter was located above the posterior part of the lower limb (Figure 2-11). The muscle stiffness

of each subject was measured in the right leg. The tests were divided into two parts: (a) relaxed leg muscles; and (b) voluntarily activated leg muscles.

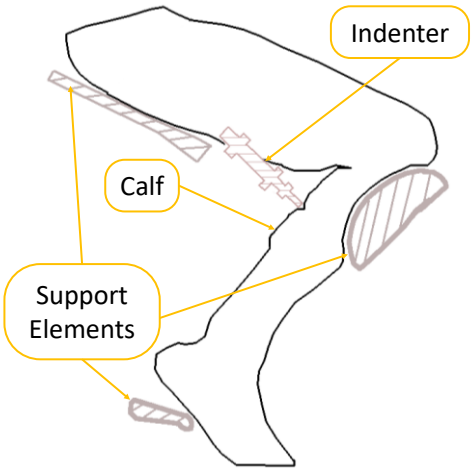

Figure 2-11. Experimental setup for indentation (adapted from Vannah & Childress, 1996)

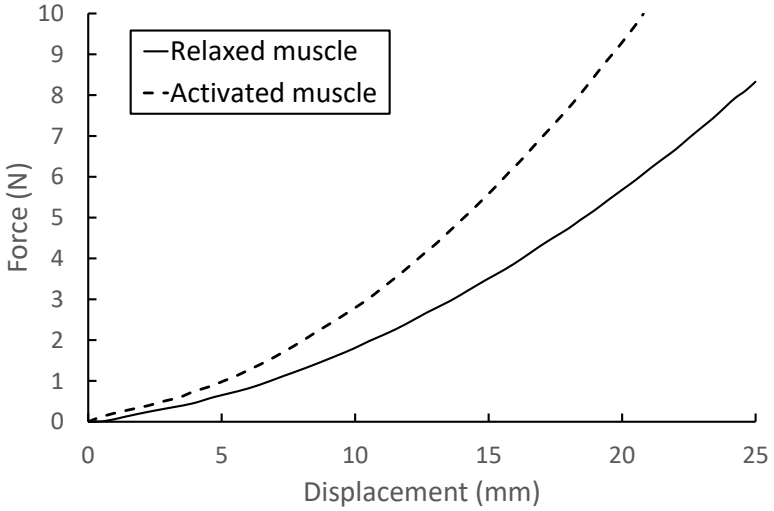

Figure 2-12. Experimental results on indentation (adapted from Vannah & Childress, 1996)

The test results were reported as force-displacement (Figure 2-12); however, the muscle activation level was not provided. Due to the lack of more detailed data, the activation level also could not be computed. However, the reaction force measured in the transverse direction shows a stiffer response for the activated muscle than for the relaxed one. In addition, the data collected in this study was not suitable for high severity impact modelling, since the experiments were performed in quasi-static conditions.

Dhaliwal et al. measured the response of lower leg muscles to compression in order to provide parameters for pedestrian impact modelling (Dhaliwal, 2002). In total, two types of impact, i.e. lateral and posterior, in four experimental setups were performed: volunteer with relaxed muscle, volunteer with tensed muscle, PMHS, and Hybrid-III dummy. Most interesting are the reports on the *in-vivo* volunteer response. The impact velocity was gradually increased between the experiments from 1 – 2.5 $m \cdot s^{-1}$. The experiments were performed according to the scheme presented in Table 2-11.

	Impact type	
Muscle state	**Posterior**	**Lateral**
Relaxed	the foot of the tested leg was suspended and plantarflexed, while the other leg held the entire body weight	the foot of the tested leg was suspended and plantarflexed, while the other leg held the entire body weight
Tensed	the foot of the tested leg was dorsiflexed and held whole body weight	the foot of the tested leg rested flat on the ground and held whole body weight

Table 2-11. Impact scenarios (adapted from Dhaliwal et al., 2002)

A major limitation of the described study is that the authors have not recorded the activation level of the tested muscles. However, since the tensed leg supported whole body weight, it may be assumed that the activation may be reaching a submaximal level (up to 91% of the muscle contraction level in a standing position, (Matkowski et al., 2011)). The effect of muscle tension influences the response of the muscle, especially in the posterior leg impacts. Reported data may serve as a baseline for the constitutive modelling of muscle compression at higher strain rates.

Muggenthaler et al. performed *in-vivo* tests on biceps brachii muscle on seven volunteers. This study investigated the behaviour of a skeletal muscle to a dynamic impact. Specifically, for those tests, a drop tower setup was used (Figure 2-13). In total, six test cases were designed and performed on every subject (Muggenthaler, 2006; Muggenthaler et al., 2008). An impactor in the drop tube hit muscle belly of biceps brachii at three different levels of activation: relaxed (F_0), half ($F_{max}/2$) and fully activated (F_{max}). The maximum force, F_{max}, was measured for each subject at maximum voluntary contraction (MVC). In all cases, the impactor was dropped from two height levels: 20 cm and 40 cm.

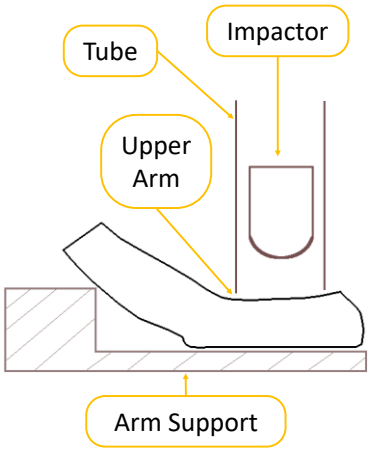

Figure 2-13. Experimental drop tower setup (adapted from Muggenthaler et al., 2008)

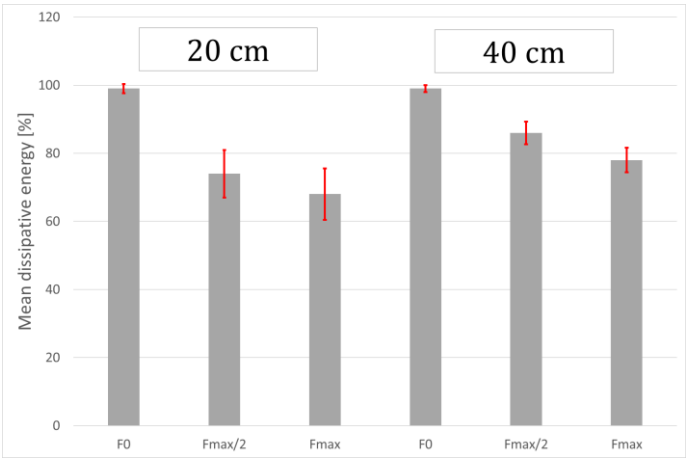

Figure 2-14. Experimental response to drop test (as reported by Muggenthaler et al., 2008)

The response of the muscle was measured by the means of rebound height and the amount of dissipated energy (Figure 2-14). Relaxed muscle does not display any rebound, whereas half and fully activated muscles show significant differences in the rebound height. Relaxed muscle absorbs all impact energy and the activated muscle stores some of the energy. Then, this energy is returned to the impactor, thus making it rebound. This phenomenon is caused by the increase of the transverse stiffness of the muscle tissue with the activation. Conclusions may be drawn that higher muscle activation results in stiffer muscle response in the transverse direction, and less energy is dissipated during the impact.

Clemen et al. (2017) also used the biceps brachii muscle to demonstrate the stiffness increase in the transverse direction. The experimental setup developed for those test cases consisted of the upper arm support, indenter, force sensor and a pulley allowing to control the external load (Figure 2-15).

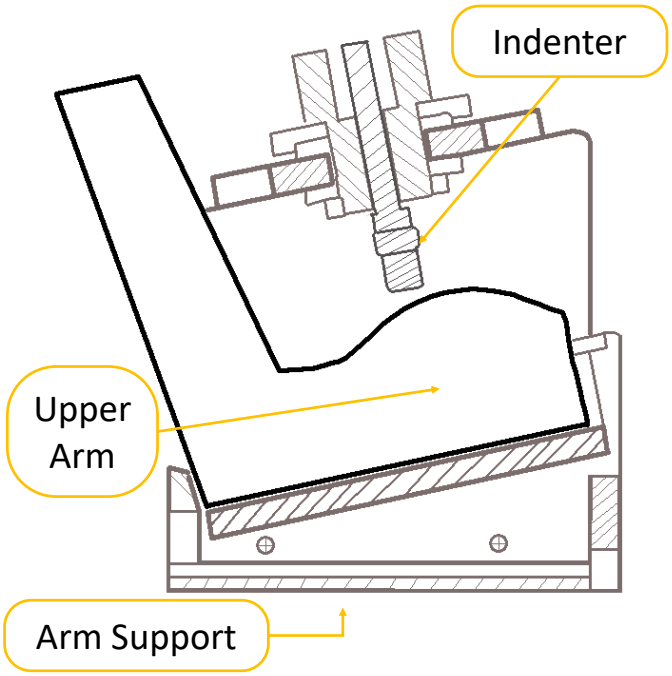

Figure 2-15. Experimental indentation setup (adapted from Clemen et al., 2017)

The experiment assumed isometric contraction of the muscle at three different external load levels: 0, 20, and 40 N. The indenter penetrated the muscle in the transverse direction at the velocity set to v = 0.75 mm·s^{-1}. The transverse response was measured at the increments of 5 mm in the range of 0-20 mm. Experimental results were reported as force-displacement. The results clearly show the dependency between the activation level and the transverse stiffness of the muscle (Figure 2-16). In the case of isometric contraction, the muscle has to generate the force equal in magnitude and opposite to the direction of the external load.

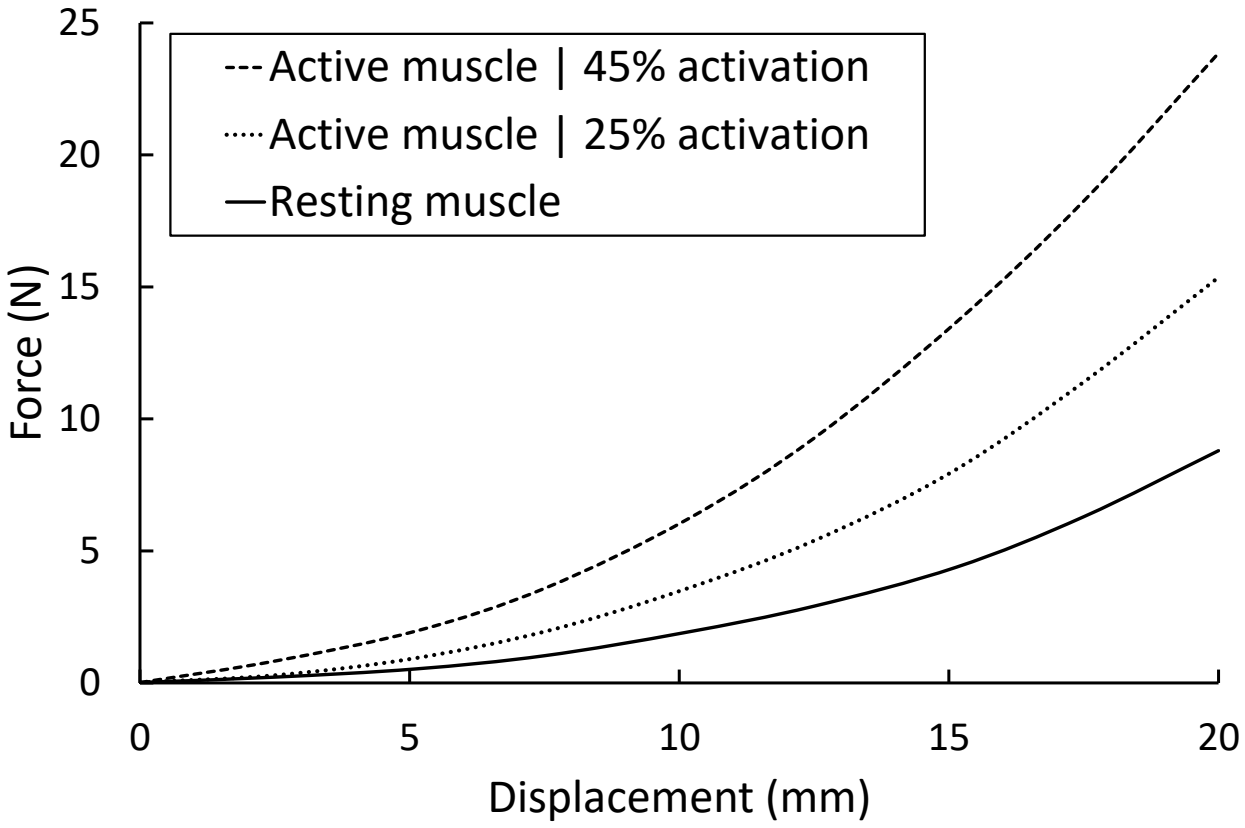

Figure 2-16. Experimental results reported by Clemen et al. (2017)

2.11 Section Summary

This section provided an overview of the existing experimental data on the soft tissue. It described the mechanical properties of the soft tissues. It is known that the response of the soft tissue to tensile and compressive deformations is highly non-linear and strain rate dependent. This chapter described the existing GHBMC arm model, which was used for a comparison with the model developed throughout this study. Moreover, this chapter identified the limitations of the existing models. In the next chapter, these limitations were addressed, first on the single element level for each tissue, and then assembled into the full-arm model indentation scenario.

3 Methods

This study investigated the contribution of the soft tissues to the response of the upper arm to indentation under quasi-static conditions. The study was performed according to the following plan (Figure 3-1). In the first phase of this study, the experimental responses of the soft tissues to mechanical loading were retrieved. Then, potential constitutive models were identified to represent the behaviour of the individual tissues. Next, the responses of the material models were verified with the experimental data on the single element level for each tissue individually. The constitutive models that could predict the experimental response most accurately were selected. These material properties are referred to as NST. In the next step, the verified NST properties were implemented in the SAM. Finally, the response of SAM to indentation was validated against another independent data set. The variability among the human population was addressed by performing parametric studies (skin thickness, skin age, arm diameter).

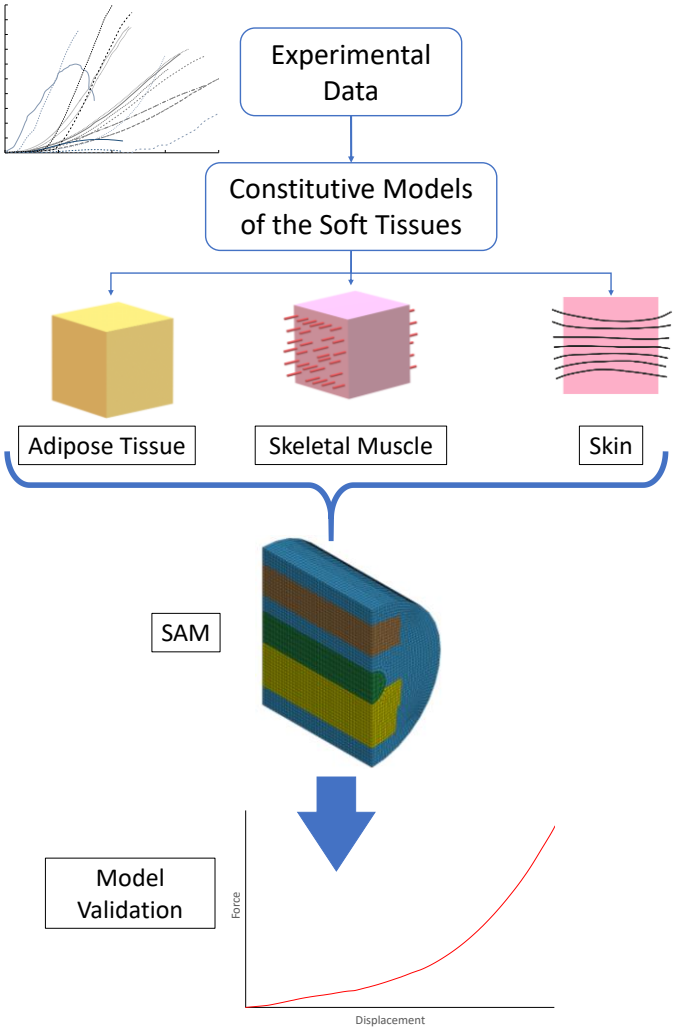

Figure 3-1. Research road map followed in the current study

3.1 Single Element Test Cases

One of the goals of this study was to find the appropriate constitutive models to represent the mechanical behaviour of the soft tissues. To achieve that, a series of single-element test cases were conducted for each tissue. A single element test case is a quick and effective way to verify that a given constitutive model is capable of reproducing the experimental response of the particular tissue. Single element test cases were designed according to the following scheme. First, an experimental data set was selected (Section 3.2). Then, an appropriate constitutive model was selected. In the next step, boundary conditions were applied to the single element. Next, a loading mode was applied to the single element (tension or compression). Finally, the numerical response

was compared with the experimental response and the goodness of fit was provided (Figure 3-2). This scenario was performed for all the soft tissues investigated in the current study, i.e. muscle, skin, and AT.

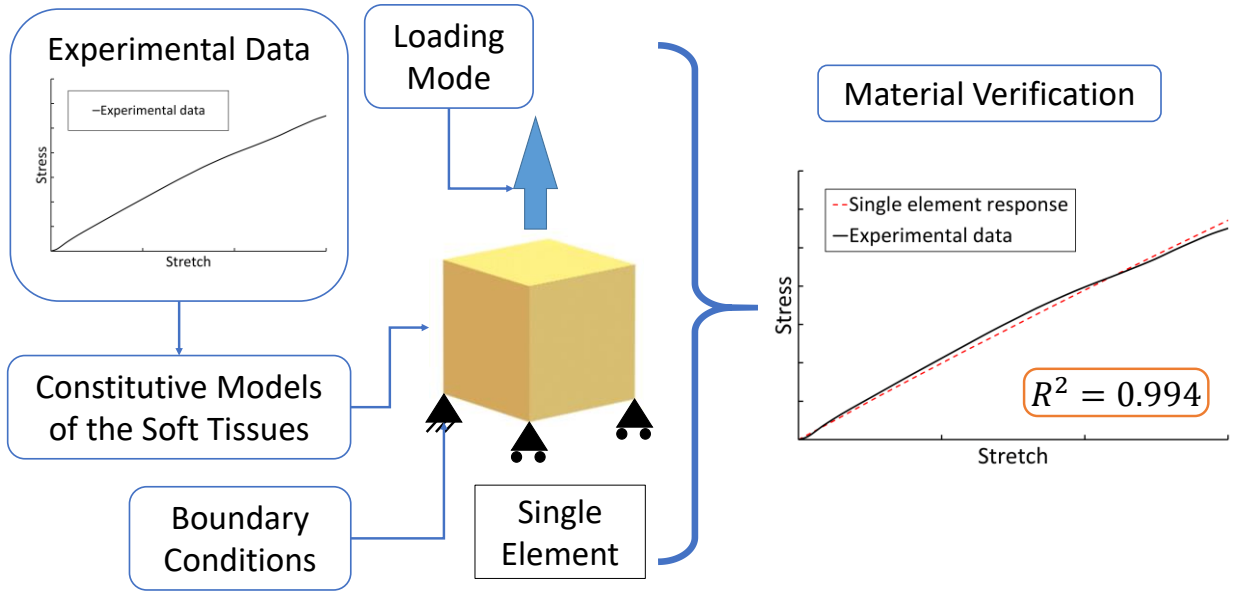

Figure 3-2. Single element test

3.1.1 Skeletal Muscle

The verification of the material models used to represent the skeletal muscle adhered to the following scheme. A hexahedral solid element with eight nodes and 1x1x1 mm dimensions was defined. Then, the model was tested in two conditions: compression and tension (Figure 3-3). In tension, the elements were stretched up to a stretch ratio of $\lambda_f = 1.3$. In compression, the elements were compressed down to a stretch ratio of $\lambda_f = 0.7$. The responses of the simulations were recorded and compared to the experimental data.

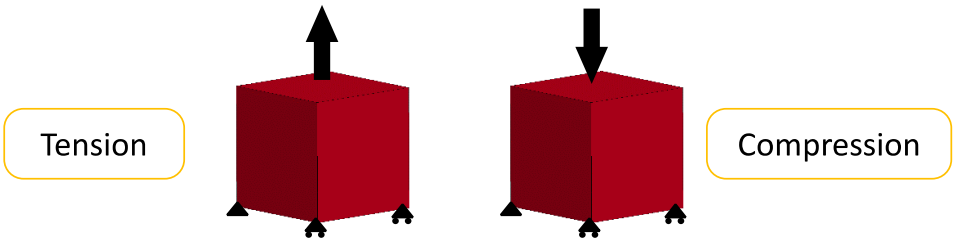

Figure 3-3. Single hexahedral element testing modes for the muscle tissue

The hyperelastic Ogden material was used as a baseline for this study. This choice was dictated by the fact that this material was primarily implemented in the GHBMC neck model. Properties for this model were adapted from the study by Hedenstierna (Hedenstierna, 2008). This model provided an accurate response in tension. However, it was not validated for the compressive loading. The authors assumed that these properties can be used also in compression. However, they failed to identify that the compressive response of the muscle is much more compliant than the tensile response. This assumption resulted in a muscle model that exhibits almost symmetrical behaviour in tension and compression, which is inconsistent with the experimental data.

The isotropic viscoelastic material model is a material model that can provide the strain rate dependent response (*MAT_VISCOELASTIC in LS-DYNA). However, as this response is linear, the simulation response followed the experimental data only in the initial stretch phase. Moreover, the response of this material is symmetrical in tension and compression. This material model was used in the GHBMC HBM with the exception of the neck region. Muscle properties for this material model were adapted from the literature (Karthikeyan, 2009).

A hyperelastic model proposed by Du Bois is a material model that requires bulk modulus, Poisson's ratio, the density of the material, and the experimental stress-strain curve or a set of load curves to account for the strain rate dependency (Du Bois, 2003). In the current study, this material was chosen to represent the mechanical behaviour of the muscle. This choice was dictated by the fact, that the response of the muscle in tension and compression is highly asymmetrical. Currently, no constitutive model in LS-DYNA library can recreate the level of asymmetry represented by the muscle tissue. Therefore, it can be represented as a single stress-strain curve and implemented in the described model. The values of bulk modulus, Poisson's ratio, and density are presented in Table 3-1. A high value of the Poisson's ratio was chosen to assure the nearly incompressible behaviour of the muscle tissue.

Density ρ ($^{kg}/_{m^3}$)	1060
Bulk modulus κ (GPa)	2.687
Poisson's ratio ν $(-)$	0.499978

Table 3-1. Mechanical properties of the muscle tissue

To represent the tensile and compressive behaviour of a modelled material, the hyperelastic Du Bois model requires a continuous stress-strain curve to cover the appropriate strain range. Experimental data used in this study for modelling the skeletal muscle was based on two sources. The compressive part of the load curve was based on the data reported by Van Loocke, whereas the tensile part of the load curve was based on the response reported by Takaza. In both cases the experiments were performed on the porcine muscle tissue under the quasi-static conditions: $\dot{\varepsilon} = 0.0005\ s^{-1}$ (Takaza, 2013; Van Loocke, 2008). These two data sets were selected for the current study because they cover a wide range of deformation, in both cases, the responses were obtained from the same species (porcine muscle tissue), and the quasi-static properties are relevant for the loading conditions used in this study. The compressive loading of the muscle tissue in the arm indentation scenario occurs in the direction transverse to the muscle fibres. Therefore, for further investigation, the tensile and compressive response of the muscle tissue in the cross-fibre direction was selected. To provide a continuous stress-strain curve in tension and compression, the following approach was used. First, tensile and compressive responses were digitized and represented as separate curves. In the next step, each curve was approximated by the Ogden function. Using the obtained analytical fit, each curve was represented as a set of stress-stretch data points at regular intervals. Then, tensile and compressive curves were joined at the (0, 0) point to provide a continuous response. Finally, the analytically obtained curve was implemented into the hyperelastic Du Bois constitutive model. This material model was proposed and developed by a colleague from the author's research group (Evans, 2018).

3.1.2 Skin

Two independent data sets of the skin properties were investigated in this study. The first one was reported by Ní Annaidh and consisted of responses from elderly PMHS (Ní Annaidh, 2012). The seconded data set was reported by Gąsior-Głogowska and was obtained from a young PMHS (Gąsior-Głogowska, 2013). These two data sets were used to assess the differences caused by the age of the skin tissue.

Ní Annaidh reported a data set of 56 skin samples excised from the back of PMHS. The excised samples were tested in tension under quasi-static conditions (Ní Annaidh, 2012). The tensile response was reported in the form of engineering stress-stretch curves. The experimental data was adapted for the FE simulations according to the following scheme. First, the response curves were

digitized. In the next step, the engineering stress was converted to the Cauchy (true) stress. To assure the regular shape of the curve, the experimental data were fitted to a hyperelastic function proposed by Ogden (Ogden, 1984; Ogden et al., 2004). Ogden material parameters are presented in Table 3-2. Fit provided by the Ogden equation was satisfactory: $R^2 = 0.9917$ (Figure 3-4).

μ (GPa)	α
1.324E-03	6.623

Table 3-2. Ogden fit parameters for the experimental data from Ní Annaidh (2012)

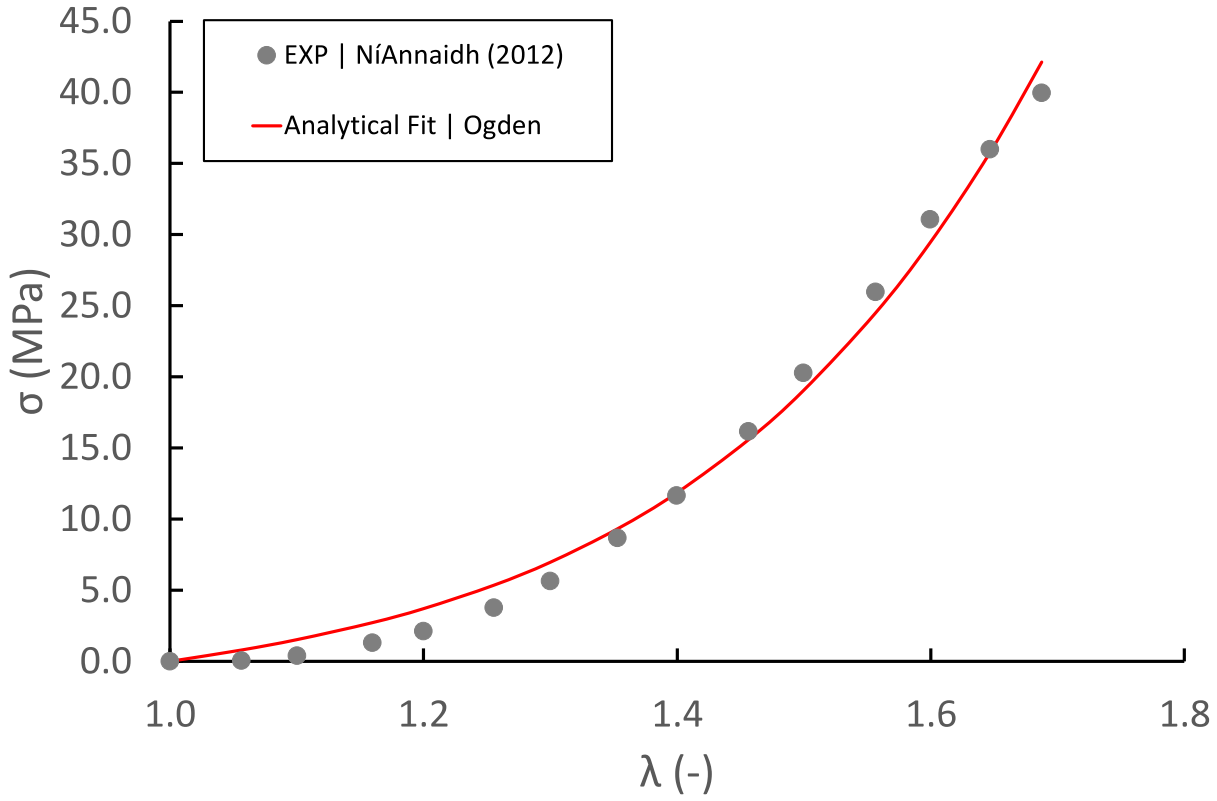

Figure 3-4. Experimental data from Ní Annaidh (2012) and analytical fit (R^2=0.9917)

Based on the obtained equation, the true stress-stretch curve with equal increments was prescribed. Then, the true stress was converted to engineering stress (3-1) and stretch was converted to engineering strain (3-2).

$$\sigma_{eng} = \frac{\sigma}{\lambda}$$

σ_{eng} – engineering stress

σ – trues stress

λ – stretch ratio

3-1. True to engineering stress conversion

$$e = \lambda - 1$$

e – engineering strain

λ – stretch ratio

3-2. Stretch ratio to engineering strain conversion

The new curve was implemented by using the Du Bois hyperelastic constitutive model. Additional mechanical parameters used to describe skin were density and Poisson's ratio: $\rho_s = 1000\ kg \cdot m^{-3}$ and $\nu = 0.495$ respectively (Gahagnon, 2012). Based on the reported data, the skin thickness was set to t = 2.0 mm (Section 2.4).

As indicated by the experimental data, the skin displays wide variability in the tensile response. To assess the influence of the skin on the indentation model, another skin model was developed in this study. This skin model was based on the experimental data set reported by Gąsior-Głogowska (Gąsior-Głogowska, 2013). This data set included the tensile response of the skin tissue in directions parallel and perpendicular to the Langer's lines. The responses were reported in the literature in the form of Cauchy stress-engineering strain curves. The provided curves were digitized and converted to engineering stress – engineering strain. In this form, those curves were implemented into the hyperelastic Du Bois constitutive model. Similarly to the previously described model, additional mechanical parameters were assigned the following values: density $\rho_s = 1000\ kg \cdot m^{-3}$ and Poisson's ratio $\nu = 0.495$ (Gahagnon, 2012). The skin thickness was set to t = 2.0 mm. In this case, two models were proposed representing both directions: parallel and perpendicular to Langer's lines.

From the two described data sets, the one presented by Gąsior-Głogowska was preferred over the one reported by Ní Annaidh. This choice was justified by the following factors: age of the subjects, body region of the excised sample, and the direction of the Langer's lines. Ní Annaidh has reported data from the specimens aged 85-97 years old. It is known, that the hydration of the soft tissues decreases with age, causing the same increase in stiffness (Schmitt, 2019). Gąsior-Głogowska has reported data from a 53 years old male. This was a significantly younger sample than those from Ní Annaidh. Secondly, the samples reported by Ní Annaidh were taken from the back region on the body, whereas in the other data set the samples were excised from the thigh. It was reported that the skin thickness on the human back may greater than the arm skin thickness by the factor of ca. 2. In contrast to this finding, the skin on the thigh represents a similar thickness to the skin on

the arm. Lastly, skin is orthotropic. Both sources acknowledged this fact. However, in the study reported by Ní Annaidh the orientation of the Langer's lines in the excised skin samples was not specified. The data reported by Gąsior-Głogowska clearly distinguished the results from both tested directions: parallel and perpendicular to Langer's lines. Based on the factors described in this paragraph, the data reported by Gąsior-Głogowska was deemed more appropriate to develop the skin model.

Skin in the FE code was implemented as a four-node shell with 1x1 mm dimensions. Then, the shell element was exercised in tension (Figure 3-5) and compared with the experimental data reported in the literature.

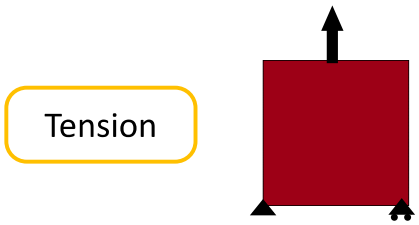

Figure 3-5. Single shell element testing mode for the skin

3.1.3 Adipose Tissue

Tensile and compressive responses of the adipose tissue are hyperelastic and viscoelastic (Comley & Fleck, 2012; Then, 2012). Therefore, from the modelling point of view, AT can be represented as a nearly incompressible hyperelastic material. In contrast to the muscle tissue, the AT is characterized by considerably lower stiffness. To recreate the behaviour of the AT, a number of hyperelastic constitutive models from the LS-DYNA library were investigated. The experimental data for the compression tests were available in abundance for a wide range of strain rates (Comley, 2012). The referred data set can be used in future studies to account for the strain rate effects. In contrast, tensile experiments on the AT do not seem common. The literature review performed in this study identified three sources reporting the tensile response of the AT. All of the tensile experiments were performed at a quasi-static rate. Orbital fat was not considered suitable for this study, because it is specific to the eye and not to the arm of the human (Chen, 2011). Alkhouli reported the tensile response of two types of the AT: omental and subcutaneous (Alkhouli, 2013). The omental fat is specific to the stomach region of the human body. The response of the subcutaneous AT was considered appropriate for this study because it is found in the region of

interest of this study (upper arm). Sommer also tested the omental AT from the human body. Although it was not used in the simulations, it was used to represent the available experimental data and provide boundaries for the comparison (Sommer, 2013).

To recreate the tensile and compressive responses of the AT, the Ogden rubber constitutive model was selected. Ogden rubber parameters were fitted to the experimental response in compression (Comley, 2012) and tension (Alkhouli, 2013). The fit for the curve was achieved by three pairs of the Ogden rubber parameters, μ and α (Table 3-3). The number of pairs of the material model parameters was set to three, because this allowed to recreate the asymmetrical behaviour of the AT in tension and compression. The density of the AT was set to $\rho_s = 920$ kg·m^{-3} (Comley, 2009; Farvid, 2006).

μ (kPa)	α (-)
8.67	4.899
-0.59	-3.377
-13.06	3.318

Table 3-3. Ogden parameters for the AT fit in quasi-static conditions

Similar to the skeletal muscle, the adipose tissue was also modelled as a hexahedral eight-node element with the dimensions of 1x1x1 mm. The adipose tissue was tested in compression and tension simulations (Figure 3-6).

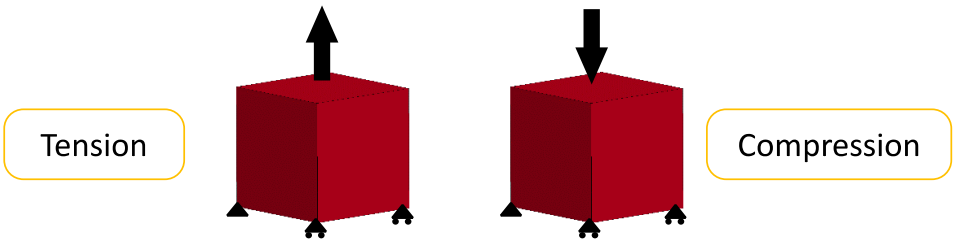

Figure 3-6. Single hexahedral element testing modes of the adipose tissue

3.2 Identification of the Experimental Data Sets used to validate the Model in the Arm Indentation Scenario

The experimental data used for the validation of the arm model was taken from the study performed by Clemen (Clemen, 2017). The experiments were performed on five human volunteers, with n = 9 measurements for every volunteer. However, in their report, the authors reported only a single force-displacement curve. Courtesy of one of the co-authors, the additional experimental data was provided in private communication (Benderoth, 2019). With this experimental data, additional insight into the experimental setup was provided. In their report, the authors stated that the population of volunteers exhibited varying body height, physique, and constitution. However, the exact anatomical dimensions were not disclosed in the report. The additional information obtained via the private communication revealed that the volunteer subjects were males between 23 and 25 years old who did not perform physical training.

The indentation experiments were performed according to the following steps. First, the arm of the volunteer was placed in the testing device. The indenter was aligned with the surface of the upper arm and further displaced by 5, 10, 15, and 20 mm into the upper arm of the volunteer. These points were referred to as relaxation termination points (RTP). Once the indenter reached an RTP, it was kept constant for 30 sec allowing the soft tissue to relax. Then, the indenter was displaced by an increment of 5 mm. This was repeated until the indenter reached the displacement of 20 mm. For the need of this study, a curve was fitted to the relaxation points of every measurement. There were 45 measurements in total. Due to the lack of additional information about the anatomical dimensions of the subjects, these experimental responses were considered as individual measurements. This allowed calculating the average and standard deviation for all curves (Figure 3-7). Such a prepared force-displacement curve was used for the comparison with the numerical responses.

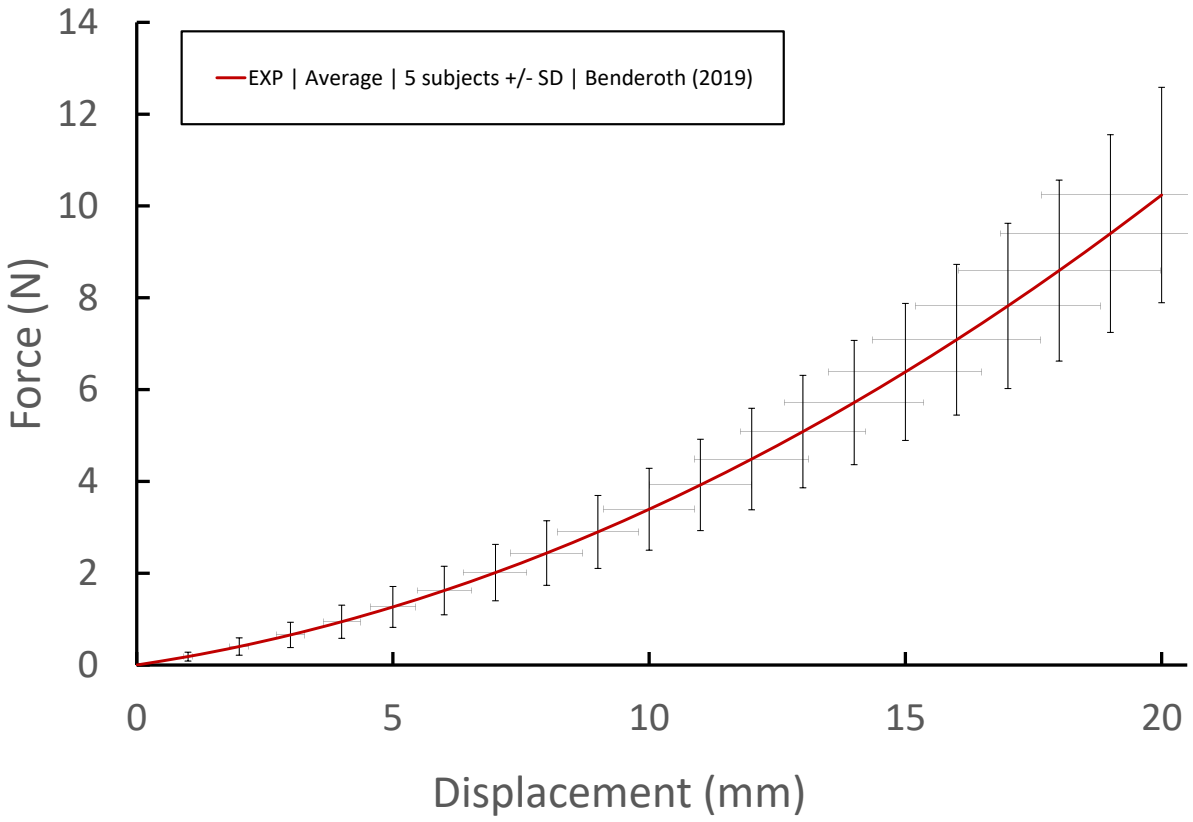

Figure 3-7. Average experimental force-displacement response with SD

Moreover, two additional metrics were used for the validation of the arm model. The first one was the peak force at the displacement of 20 mm. In this case, the average experimental response and SD were calculated for all curves (Figure 3-8).

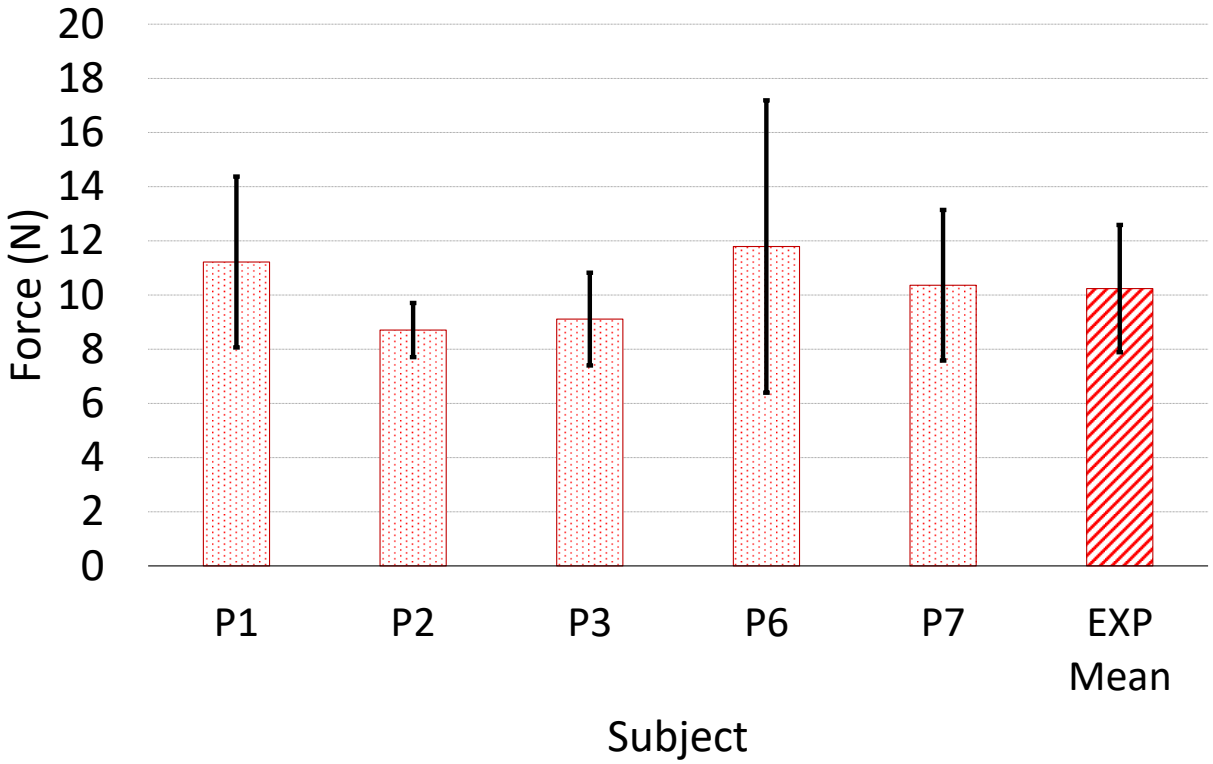

Figure 3-8. Maximum force at 20 mm displacement for experiments and average value with SD

The second metric was indentation energy. This energy was calculated as the area under the force-displacement curve. This value was obtained for each experimental measurement. Then the average of all experimental data with SD was provided. The numerical responses were all compared to the average indentation energy.

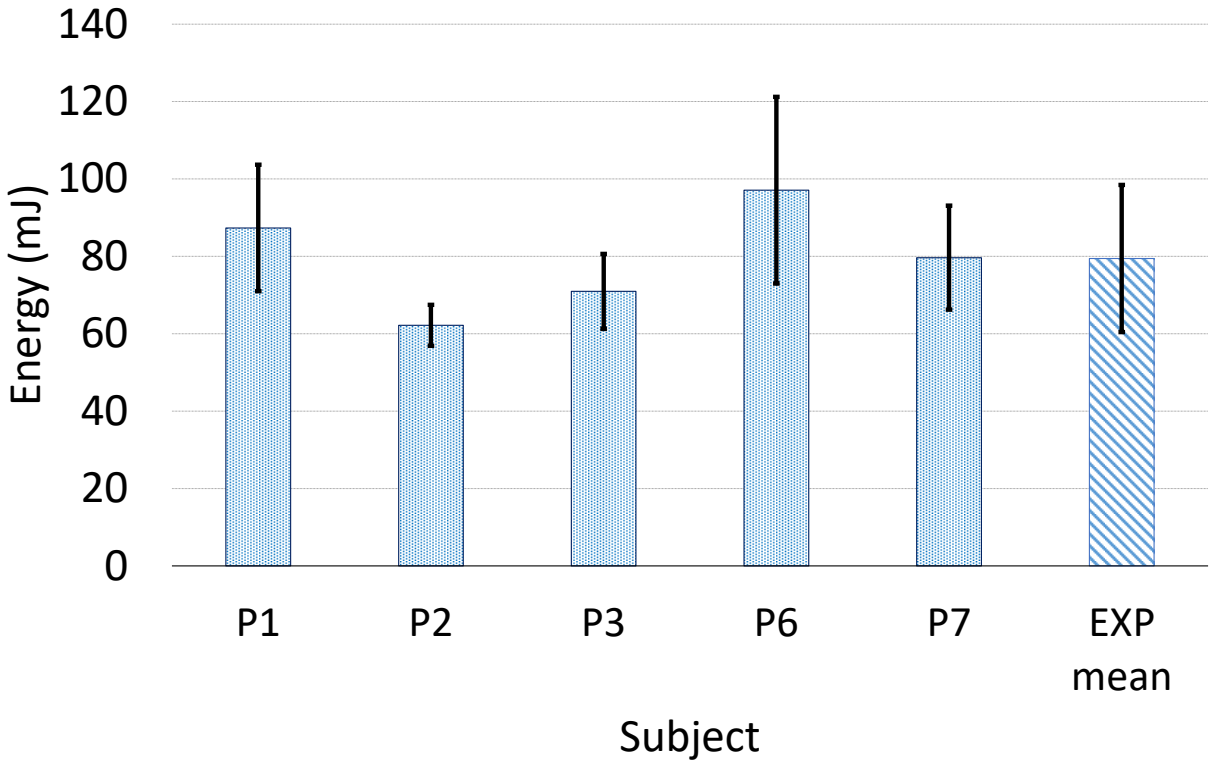

Figure 3-9. Indentation energy for experiments and average with SD

The numerical responses were compared with the experimental data by providing the range of percentage differences between the numerical and experimental results. The differences were calculated based on the relative error formula (3-3). The differences were calculated for both metrics: the indentation energy and the peak force.

$$\delta = \frac{|EXP_{avg} - SIM|}{EXP_{avg}} \times 100\%$$

EXP_{avg} average experimental value

SIM compound standard deviation

3-3. Relative error formula

3.3 Development of the Arm Model used in the Indentation Simulation

The arm model in this study was represented in two ways: a simplified arm model developed from data in the literature, and the existing GHBMC arm model. These two models differ in terms of geometry and mesh density. Both of the models were investigated to assess the change in response

stemming from their differences. The indentation simulation test case was adapted from the study presented by Clemen (Clemen, 2017).

To avoid confusion and lengthy descriptions, a certain naming convention was assumed for the two main topics of this study. First, a simplified arm model was developed. Further on, this model is referred to by the acronym SAM. Second, the set of new soft tissue models (i.e. skin, muscle, and adipose tissue) is referred to by the acronym NST. This acronym stands for *New Soft Tissues.*

3.3.1 Simplified Arm Model (SAM)

For the need of this study, a testbed was developed. It represented a simplified geometry of the upper arm. For this, the geometry of the GHBMC arm model was analyzed. The GHBMC arm included the geometrical representations of two muscles in the human upper arm: *biceps brachii* and *triceps brachii*, adipose tissue, and skin. The cross-section areas of those muscles were measured and then implemented within SAM. Thus, the cross-section of SAM resembled the one of the GHBMC arm model (Figure 3-10). Dimensions for the SAM were taken from the experimental measurements reported in the literature and the GHBMC arm model. Based on the literature review, the diameter of SAM was set to 100 mm (Ahmadi et al., 2007; ElMaraghy et al., 2008; Robbins, 1983; Wang et al., 2006). Also based on the literature review, the diameter of the humeral bone in SAM was set 20 mm (Dr.Gayatri & H. R. Sharada, 2014; Murdoch et al., 2002; Singh et al., 2014). Dimensions used in this study are summarized in Table 3-4.

Bone diameter [mm]	Arm diameter [mm]	Length [mm]	Length (quarter model) [mm]
20	100	160	80

Table 3-4. Anthropometric dimensions of the upper arm model

Finally, quarter symmetry boundary conditions were applied to SAM, and the response of the quarter model was recorded and compared with the full model response. The responses used for comparison were the force-displacement curves. It is important to note that in the case of the quarter symmetry model, the reaction force is only the quarter of the value of the full model. Therefore, to perform the comparative study, the reaction force of the quarter model had to be multiplied by the factor of 4. The comparison of the reaction forces for both cases displayed good similarity ($R^2 = 0.9824$). Therefore, the quarter model was used for the remaining part of this study. To provide consistent analysis, the rigid indenter was also modelled as a quarter model.

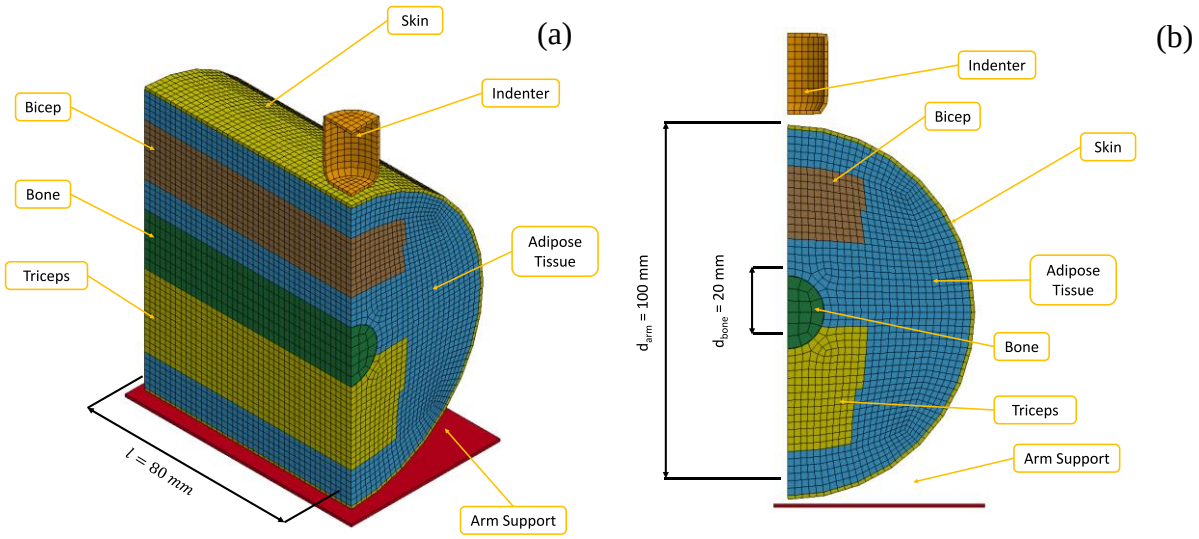

Figure 3-10. SAM: (a) isometric view, (b) cross-section view

The most accurate model of each tissue from the single element tests was implemented in the arm model, and the arm model with the newly developed soft tissue models was tested in the indentation scenario. The soft tissue models used in the final test cases were based on the identified experimental material test data (Table 3-5).

Tissue	Loading	Reference	Selected material model
Skeletal muscle (cross-fibre direction)	Tension	Takaza et al. (2013)	*MAT_SIMPLIFIED_RUBBER
	Compression	Van Loocke et al. (2008)	
Adipose Tissue	Tension	Alkhouli et al. (2013)	*MAT_OGDEN_RUBBER
	Compression	Comley & Fleck (2012)	
Skin (parallel to Langer's lines)	Tension	Gąsior-Głogowska et al. (2013)	*MAT_SIMPLIFIED_RUBBER

Table 3-5. Sources of the soft tissue material properties

Anthropometrical studies provided the outer diameter of the upper arm. As it was shown in Table 2-6, the variability in the dimensions is significant. The numbers representing minimal, average, and the maximal value were rounded to the values presented in Table 3-6.

Dimension	Diameter (mm)
low	70
average	100
high	120

Table 3-6. Diameters of the upper arm used for the parametric study simulation

The baseline value of the diameter was d = 100 mm. The baseline model was scaled to the reported experimental data on upper arm diameters. Based on the reported anthropometrical data for the upper arm tissue, the lower and upper bound were set to d_{low} = 70 mm and d_{up} = 120 mm, respectively. Further, the dimensions of the internal tissues were scaled using the same factor. Thus, prepared models were exercised in the indentation simulation. The responses of all three models were recorded and reported in the results section (Section 4.3.4).

The initial design of the arm model was based on a full cylindrical shape. Due to the quasi-static nature of the test, this approach was computationally very expensive. In the course of work and the model analysis, it was discovered that the model can be analyzed using quarter symmetry conditions to reduce calculation time. Quarter symmetry boundary conditions imply that the nodes placed in the symmetry plane, cannot move in the direction normal to this plane. To follow the symmetrical conditions, the nodes in the symmetry plane can rotate around the axis normal to the plane of constraint. Identical quarter symmetry conditions were also applied to the indenter model. Quarter symmetry is useful from the computational point of view because it decreases the computational time by ca. 75%.

3.3.2 Mesh Refinement Study

A mesh refinement study was performed to analyze the effect of discretization on the model response. The initial mesh size of the model was 2 mm. Based on the Grid Convergence Index study (Roache, 1994), this mesh size was defined as the *medium* size. Two additional mesh sizes were investigated: *coarse* mesh: 4 mm, and *fine* mesh: 1 mm. The single split of the coarse mesh resulted in the medium mesh. The second split resulted in the *fine* mesh.

Mesh convergence is important to quantify the effect of discretization on the response. The mesh size used in the computational model can influence the simulation results. In the case of a coarse mesh (large elements relative to the model geometry), the detail level may be inadequate to predict localized stresses and deformations in the model. This may provide an unphysical result. On the other hand, in case of a too fine mesh (small elements relative to the model geometry), the computations may become numerically expensive, consuming extensive resources and time to finish the simulation. The size of the mesh is unique to the given problem. It should be chosen through the mesh refinement study. The mesh convergence study determines if a certain metric converges, as the mesh size is refined. This study begins with a coarse mesh size and the metric

response is stored. Then, the mesh size is halved and the metric is recorded again. This process is repeated until the model response converges to a value within the acceptable limit. Richardson Extrapolation is a mathematical method used to quantify and compare the response of different mesh sizes. This method is also related to the Grid Convergence Index (GCI) (Roache, 1994).

The GCI is a standardized method of measuring the convergence in numerical models. The rationale behind this method assumes that as the mesh becomes finer, the model response is closer to the actual value. To investigate the GCI, results from three simulations are required. Next, an extrapolated value is calculated. This is called the Richardson Extrapolation and determines the response as the mesh size approaches zero. The metric for the zero mesh size is calculated:

$$f_0 \cong f_1 + \frac{f_1 - f_2}{r^p - 1}$$

Where f_1, f_2, and f_3 are the metrics of fine, medium, and coarse mesh, r is the grid refinement ratio (usually r = 2, when the elements are halved), and p is the order of convergence.

$$p = \frac{\ln\left(\frac{f_3 - f_2}{f_2 - f_1}\right)}{\ln(r)}$$

Then, the mesh error is calculated:

$$A_1 = \frac{f_1 - f_0}{f_0}$$

The next step allows verifying if the metric value is in the asymptotic zone of the convergence. For that, two values of the GCI have to be calculated: fine to medium (GCI_{12}) and medium to coarse (GCI_{23}) meshes. These equations also include the safety factor, F_s, which is recommended to be 1.25-1.5 for a high confidence level in the three mesh analysis (Roache, 1998).

$$GCI_{12} = \frac{F_s\left(\frac{f_2 - f_1}{f_1}\right)}{r^p - 1}$$

$$GCI_{23} = \frac{F_s\left(\frac{f_3 - f_2}{f_2}\right)}{r^p - 1}$$

To check if the response is in the asymptotic region, the following equation is used:

$$GCI_{23} - r^p GCI_{12} \approx 0$$

When this condition is satisfied, then the metric values are in the asymptotic region and converge.

In the course of this research, the mesh refinement study was conducted for three mesh sizes. The characteristic element length was set to 1, 2, and 4 mm for fine, medium, and coarse mesh, respectively (Figure 3-11).

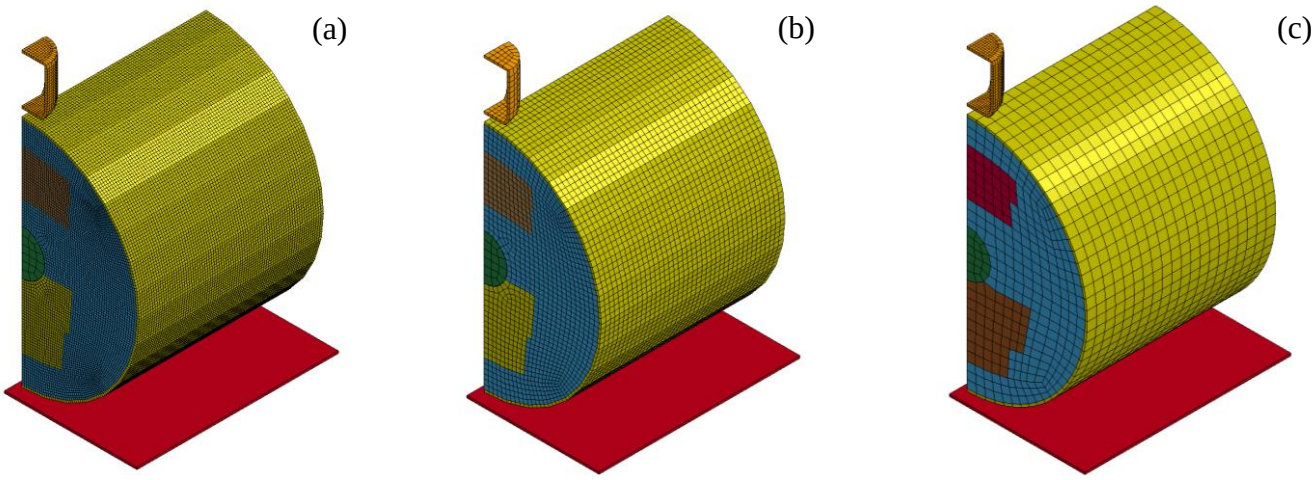

Figure 3-11. Models used in the mesh convergence study: (a) fine mesh, 1 mm; (b) medium mesh, 2 mm; (c) coarse mesh, 4 mm

The number of elements in the FE simulation (Table 3-7) is an important factor for two reasons. First, it affects the size, and thus, the computational time of the simulation. Fine mesh requires much more time to complete than the medium and coarse mesh. The second reason is the accuracy of the response. Fine mesh provides may provide a more accurate response. However, due to certain constraints, long computation time may be undesirable. Mesh refinement study is a tool that allows determining the compromise between the accuracy of the response and the computational time.

	Fine		Medium		Coarse	
	Nodes	**Elements**	**Nodes**	**Elements**	**Nodes**	**Elements**
Skin	13041	12800	3321	3200	861	800
Adipose Tissue	297027	279360	39401	34920	5922	4700
Bicep	40905	36800	5658	4600	819	540
Triceps	58239	53120	7954	6640	1386	1000
Bone	984	640	984	640	504	320
Indenter	553	512	149	128	53	40
Total	410749	383232	57467	50128	9545	7400

Table 3-7. Number of nodes and elements for three mesh sizes

Mesh convergence study requires choosing a metric value. The metric selected for this study was the reaction force at the final displacement. For each mesh density, the value of the reaction force was collected and then input to the mesh convergence formulas reported in this section of the document.

3.3.3 GHBMC Arm Model

The GHBMC HBM provides a biofidelic response of the human body during various impact scenarios. The scope of this research was the response of the upper arm to the indentation. For the need of this research, the upper arm between the shoulder and elbow was extracted from the GHBMC HBM (M50-O, Version 4.5, GHBMC). To provide numerical stability of the extracted portion of the upper arm model, the following boundary conditions were introduced. Node sets were created for the cross-sections at which the arm was extracted from the full-body model. To assure the numerical stability of the extracted arm model, the nodes in both cross-sections were allowed to move only in the Z direction, which is consistent with the experimental boundary conditions (Clemen, 2017). In the described setting, the Z direction is perpendicular to the longitudinal axis of the upper arm. With these conditions, a pre-simulation was performed. The gravitational load was applied to the upper arm to let it settle on the support. The support was defined as a non-deformable rigid wall (*RIGID_WALL in LS-DYNA). After the upper arm settled, new nodal positions were extracted and saved. These new nodal positions were further used to represent the resting arm during the indentation simulation. The extracted arm model is presented in Figure 3-12.

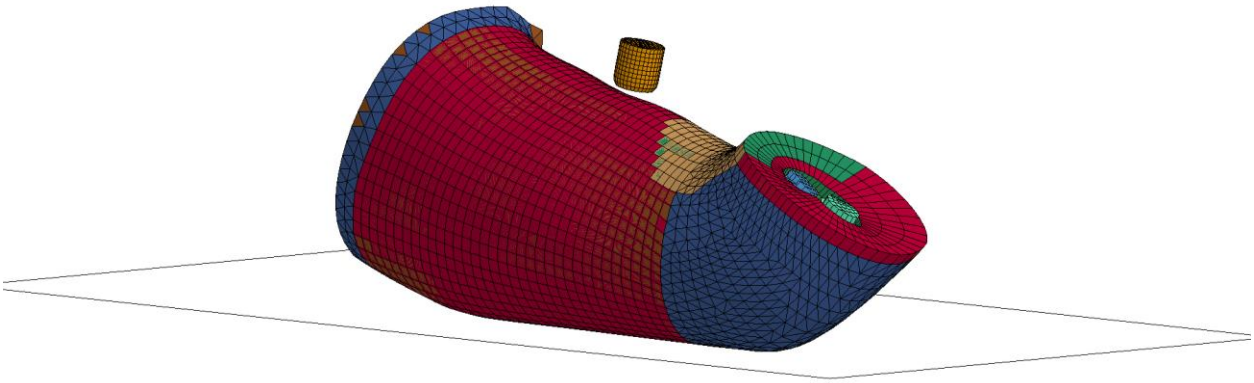

Figure 3-12. Extracted arm from the GHBMC HBM with indenter

Two simulation test cases were performed with the GHBMC arm model. In the first case, the extracted GHBMC arm model with the original GHBMC soft tissue properties was indented. In the second case, the GHBMC soft tissue models were replaced with the soft tissue models developed in this study, retaining the original geometry and composition of the GHBMC arm model. In both cases, the force-displacement responses were collected.

Finally, the responses of the GHBMC arm were compared with the arm model developed in this study, as well as with the experimental data.

3.3.4 Bone Model Used in the Simulations

In both arm models, SAM and GHBMC, the humeral bone material was taken from the GHBMC HBM. This material is linearly plastic and in comparison to the soft tissues does not deform considerably. In the simulation environment, the bone was connected to the surrounding soft tissues with a tied contact. This type of contact allows for connecting parts with different mesh density. It was preferable to use this type of contact as the bone and surrounding soft tissues were modelled with different mesh sizes.

3.3.5 Indenter Model

The experimentalists performed the experiment by indenting the bicep with an indenter. However, they did not report the exact size, nor material properties of it. Based on the available image data, the visual inspection led to the conclusion that the indenter has a similar diameter to the bone. Therefore, the diameter of the indenter was defined as 20 mm.

The indenter was modelled as a non-deformable rigid body (*MAT_RIGID in LS-DYNA). This approach assured that the indenter maintained the original shape throughout the simulation. The rigid model requires the definition of Young's modulus (Hallquist, 2015). In the indentation scenario, the rigid indenter interacted with the soft tissues (skin, muscle, and adipose tissue). To avoid numerical instabilities, Young's modulus was set to a low value, similar to the value exhibited by the soft tissue. The indenter was located above the arm model with a small gap to avoid any initial penetrations between the parts, i.e. indenter and the skin surface.

3.3.6 Boundary Conditions used in the SAM indentation Scenario

The boundary conditions were applied to SAM to recreate the experimental conditions. The quarter boundary conditions were described in Section 3.3.1. In the simulated experiment, the arm was indented in the vertical direction (downwards in the Z-direction). Because of that, the nodes at both ends of the bone were allowed to move in the Z-direction and were restrained from motion in the X- and Y-directions. This condition prevented the model from sliding over the supporting surface.

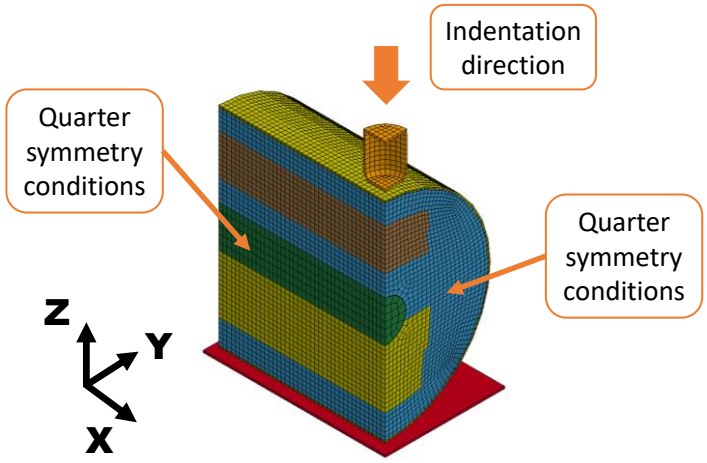

Figure 3-13. Quarter boundary conditions for SAM

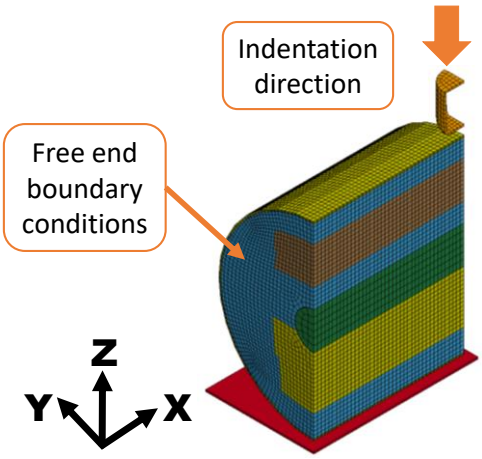

Figure 3-14. Free end boundary condition for SAM

The additional boundary conditions were applied to the free end of SAM (Figure 3-14). The nodes at the free end of SAM were restrained from movement in the X-direction.

To recreate the boundary conditions of the experiment, SAM had to be first subjected to the gravitational preloading. Thus, the simulation scenario was divided into two phases. In phase I, the gravitational acceleration was applied to SAM (Figure 3-15). After the model settled, the

gravitational acceleration was kept constant and stresses and strains were retained from the pre-simulation (Figure 3-16). In phase II, SAM was indented (Figure 3-17). This approach allowed for recreating the boundary conditions of the reported experiment.

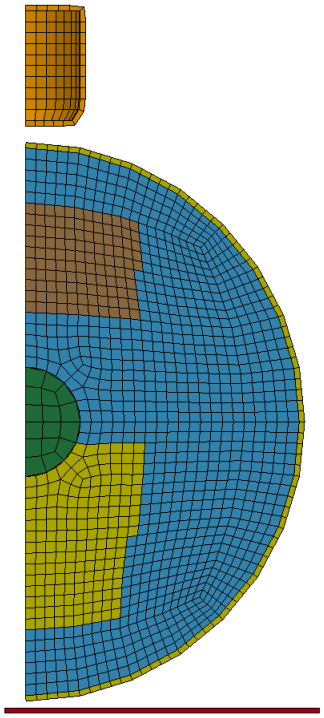

Figure 3-15. Phase I: Pre-loading under gravitational force

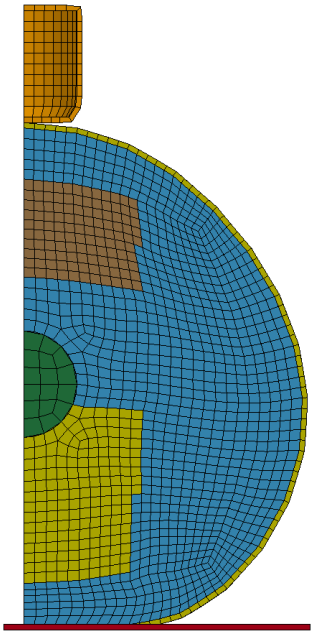

Figure 3-16. SAM after gravitational pre-simulation

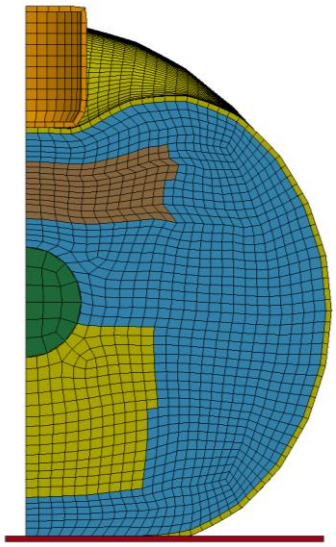

Figure 3-17. Phase III: After indentation

Indentation conditions were based on the experimental setup described by Clemen (Clemen, 2017). The indenter penetrated the arm model down to 20 mm at a quasi-static speed of v = 0.75 mm·s^{-1}. This condition was implemented in LS-DYNA using *BOUNDARY_PRESCRIBED_MOTION_SET keyword. Nodes used to describe the indenter were assembled in a set. Consequently, displacement at a constant rate was assigned to this node set. This allowed the indenter to penetrate the arm model.

The testbed with the applied boundary conditions described above allowed testing the model with different properties of the soft tissues. Those test cases used different material models and allowed to assess their contribution to the model response.

3.4 Parametric Studies of the on the Arm Indentation Model

Each of the tissues investigated in this study displayed own, characteristic mechanical properties. Part of the investigation was to analyze their response in an isolated test environment (single element test cases). However, it is also important to investigate how they behave in a complex model where they all contribute to the final response. For this reason, the developed model testbed was used to perform a set of parametric studies.

3.4.1 Comparison of the GHBMC and the NST Properties

In the course of this study, the soft tissue properties of the GHBMC arm model were considered as a baseline. Results on the single element level have proven that these properties were stiffer than the majority of the experimental responses of the particular tissues (Figure 4-1, Figure 4-3). Nevertheless, these properties were implemented in the SAM and tested in the indentation scenario. The response of the model with the GHBMC tissue properties was recorded and then compared with the response provided by the model with new material properties.

3.4.2 Skin Thickness

In the FE model, the skin was represented by shell elements with a specific constant thickness and mechanical properties. As reported in section 2.4 of this document, the thickness of the skin varies across the human body. It also depends on the age of the subject (Reihsner, 1995). The study by Reihsner reports the average skin thickness at 1.88 +/- 0.22 mm However, other studies mention 1.50 mm (Gąsior-Głogowska, 2013) or 2.00 mm (Ottenio, 2015). Moreover, the skin model currently used in the GHBMC body model is 2.00 mm. To consider this variability, a parametric study on the skin thickness was performed. The indentation test cases were performed for three different values of the skin thickness: 1.50, 2.00, and 2.50 mm. Force-displacement responses for all test cases were collected and compared.

3.4.3 Mechanical Properties of the Skin

Two data sets have been selected from the plethora of experimental data on the tensile response of the human skin. The first data set was reported by Gąsior-Głogowska and consisted of the tensile response of the skin from the thigh of the young specimen, 53 years of age (Gąsior-Głogowska, 2013). The second data set was reported by Ní Annaidh and showed the tensile response of the skin from the back of the elderly specimen, 87-95 years of age (Ní Annaidh, 2012). These two data

sets were analyzed to assess the influence of the aged material properties on the indentation response.

The skin of the elderly subject displayed stiffer tensile response than the skin of the younger subject by almost an order of magnitude. It was then hypothesized that the skin model may have an influence on the response of the upper arm to indentation. Therefore, both the skin models were implemented in SAM and tested in the indentation scenario. Force-displacement response of both simulations was collected and compared.

3.4.4 Arm Dimensions

As mentioned in section 3.4.1 diameter of the upper arm varies among the population. This variability was addressed in the current study. Three upper arm diameters were selected for this parametric study. The lower bound diameter was set to 70 mm (Figure 3-18), the baseline diameter was set to 100 mm (Figure 3-19), and the upper bound diameter was set to 120 mm (Figure 3-20). The cross-sectional dimensions of bone, skeletal muscle and AT were scaled by 0.7 and 1.2 for the 70 mm and 120 mm arm models, respectively. The skin thickness remained unchanged (t = 2.0 mm).

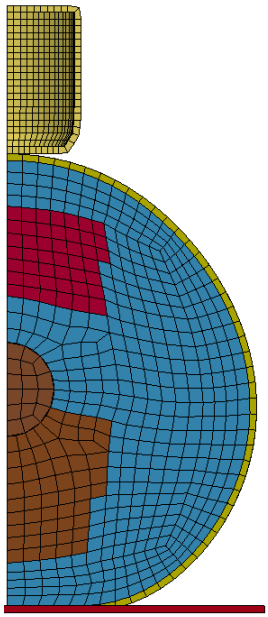

Figure 3-18. Arm diameter d=70 mm (adipose tissue - blue, bicep - red, triceps - brown, skin - yellow)

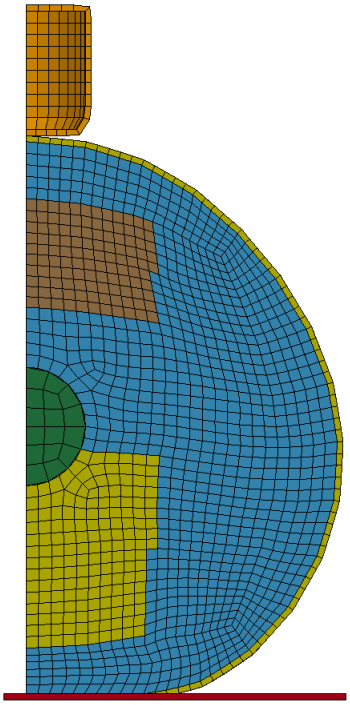

Figure 3-19. Arm diameter d=100 mm (adipose tissue - blue, bicep – light brown, triceps - yellow, skin – dark yellow)

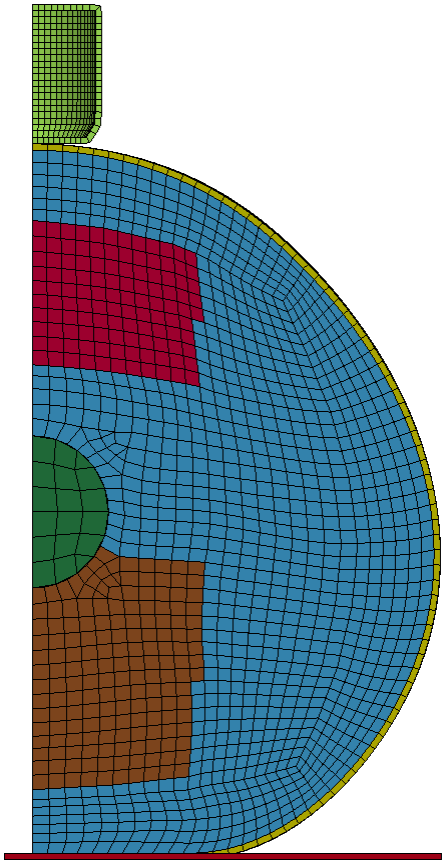

Figure 3-20. Arm diameter d=120 mm (adipose tissue - blue, bicep - red, triceps - brown, skin - yellow)

3.5 Reporting the Simulation Results

In the experimental study used for validation of SAM, only a single force-displacement curve was reported as the response to the arm indentation (Clemen, 2017). It is not possible to observe variability between the subjects based on a single response. Courtesy of one of the co-authors of the mentioned study, additional experimental data was made available (Benderoth, 2019). This data provided more insight into the response of the upper arm to indentation and showed variability among the subjects. For each of the five volunteer subjects (P1, P2, P3, P6, P7), n = 9 measurements were performed, resulting in 45 responses in total. The experimental results were reported in the form of force-displacement curves. The volunteers participating in the experimental study were of different postures and body dimensions. However, these details were

not disclosed in the report. Therefore, although the force-displacement curve is a reasonable way of reporting the measurements, it will display variability between subjects. The force response may vary based on the arm dimensions and different amounts and distribution of soft tissues within the arm. In the current study, another metric was employed to compare the simulation response with the experimental data. This metric is the amount of energy absorbed by the upper arm during indentation. The energy value was calculated as the area under the force-displacement curve. The energy was calculated for all experimental responses and reported as a mean value +/- standard deviation for every subject. These data were then plotted on a bar chart and compared with the simulation responses obtained from the parametric studies. In the results section, the mean values and SD were provided. Moreover, the error margins were calculated for the simulation responses.

An additional metric used to compare the simulation responses to the experimental data was the peak force, measured at the final displacement of the indenter. Similar to the absorbed energy, the peak force value of each measurement was collected. Then, for each subject, the mean and SD were calculated. The experimental results were then plotted on a bar chart allowing for comparison with the peak force obtained in the simulations. Error margins were provided for the peak force value.

4 Results

This chapter of the thesis presents the results obtained from the simulations, beginning with the single element test cases for individual soft tissues (skin, muscle, and adipose tissue). Next, the results of the mesh refinement study on the arm finite elements are presented. Finally, the responses of the indentation simulations are covered, including parametric studies investigating the effect of different factors, i.e. skin thickness, skin age, arm diameter.

4.1 Single Element Test Cases Compared to Experimental Data

4.1.1 Skeletal Muscle

Two models of skeletal muscle were implemented in the GHBMC HBM. The first model was implemented using the hyperelastic Ogden material with the material properties based on the study by Hedenstierna (Hedenstierna, 2008). The second model was implemented using the linear viscoelastic model with the material parameters based on the study by Karthikeyan (Karthikeyan, 2009). Both these materials were used for the comparison with the experimental data and models developed in this study. However, both of these models exhibit certain limitations. The Ogden material with properties by Hedenstierna was only validated in tension, thus not taking the asymmetry in compression into account. The viscoelastic model with parameters reported by Karthikeyan is linear, therefore it fails to grasp the hyperelastic behaviour of the muscle. Single element simulation results were compared with the available experimental data.

Tension

The current skeletal muscle model within the GHBMC HBM was implemented with an Ogden hyperelastic constitutive model (*MAT_OGDEN_RUBBER in LS_DYNA) with material model parameters proposed by Hedenstierna (Hedenstierna, 2008). (Figure 4-1). Alongside the simulation response of the baseline model, the experimental data is also presented.

As mentioned earlier, the muscle acts as a nearly incompressible material. Therefore, constitutive models used to describe nearly incompressible behaviour were analyzed and compared with the experimental data (Figure 4-1, Figure 4-2).

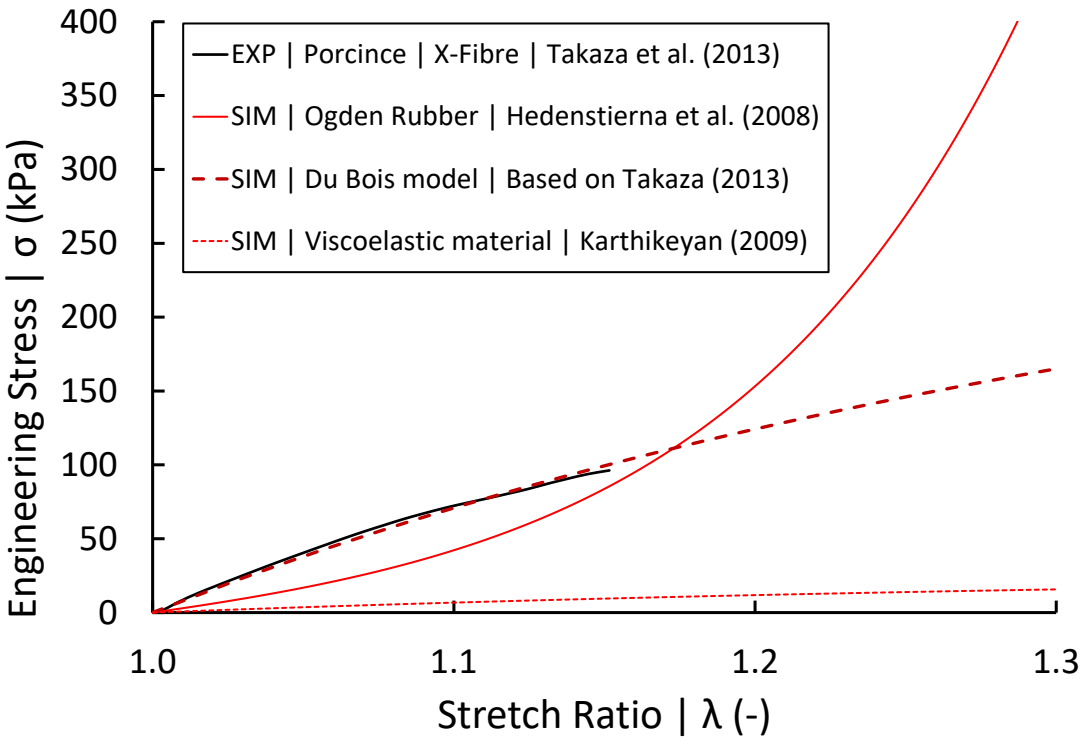

Figure 4-1. Tensile response for the single element simulations and experimental data of the muscle tissue

It can be observed that the stiffness of the Ogden material with parameters by Hedenstierna increases rapidly. After a stretch of ~1.17, the response of this model demonstrated higher stresses compared to the experimental data. For clarity, Figure 4-2 shows the same response without the baseline model.

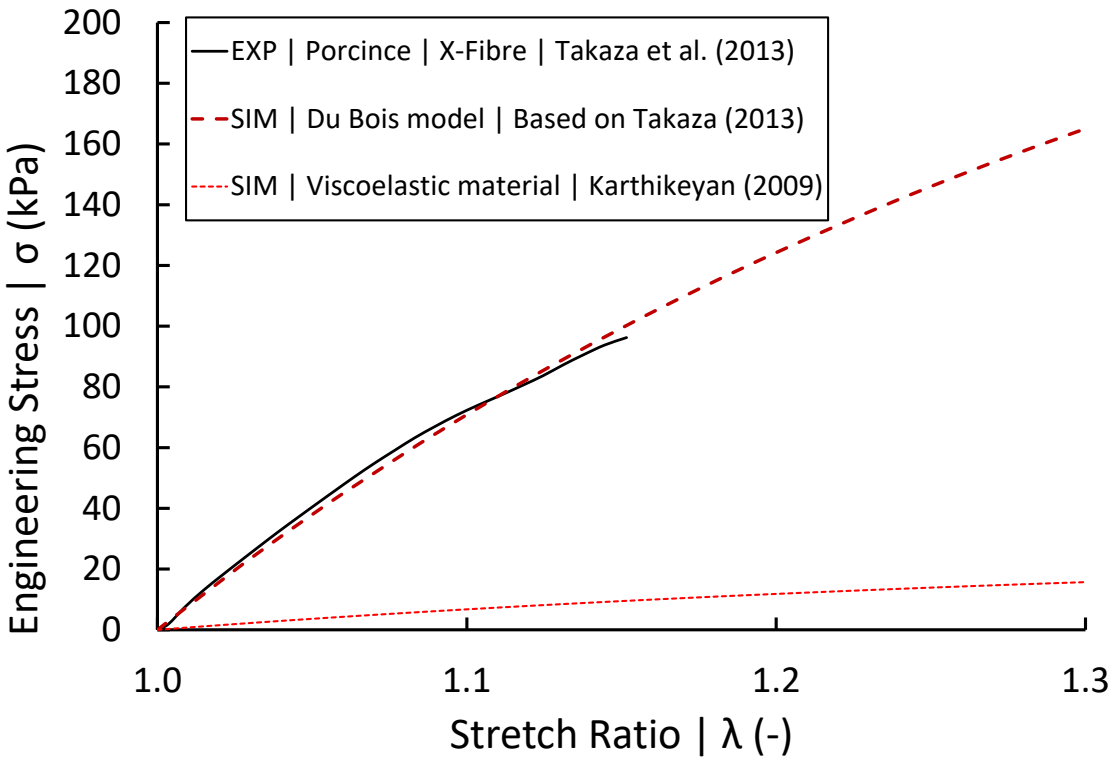

Figure 4-2. Single element in tension. Simulation response and experimental data (detailed view)

The viscoelastic model proposed by Karthikeyan showed a linear response to tension. This result is contradictory to the majority of the experimental reports on the tensile response of the muscle (Section 2.3.4). The Blatz-Ko rubber required the shear modulus of the muscle in tension. This modulus was based on the linear portion of the experimental response reported by Takaza (Takaza, 2013). The goodness of fit for this model was quite high, $R^2 = 0.899$. The hyperelastic Du Bois model was capable of recreating the experimental tensile response and provided a high goodness of fit, $R^2 = 0.955$. Therefore, it was selected for further use.

Compression

The baseline model and other models were also investigated for compression loading. As discussed earlier, muscle tissue is more compliant in compression than in tension (Figure 2-3 and Figure 2-4). The comparison of the baseline model, selected experimental data, and other constitutive models was presented in Figure 4-3.

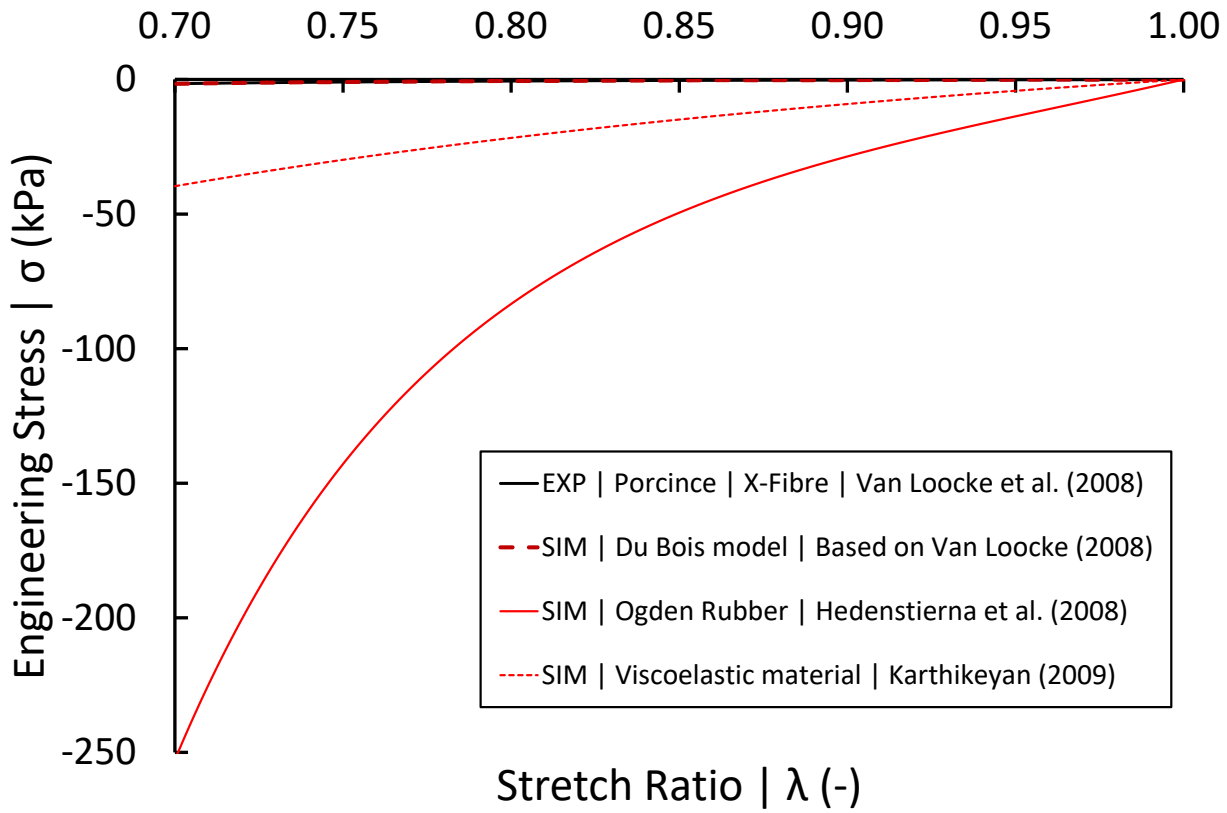

Figure 4-3. Passive muscle single element in compression. Simulation response and experimental data

The stress response of the Ogden material with the Hedenstierna parameters model was two orders of magnitude higher than the stresses reported in the experimental data. Also, the response provided by the viscoelastic model proposed by Karthikeyan exhibited behaviour stiffer than other than known experimental data (Figure 4-3). To show the compressive responses of the muscle tissue in detail, another plot was provided (Figure 4-4).

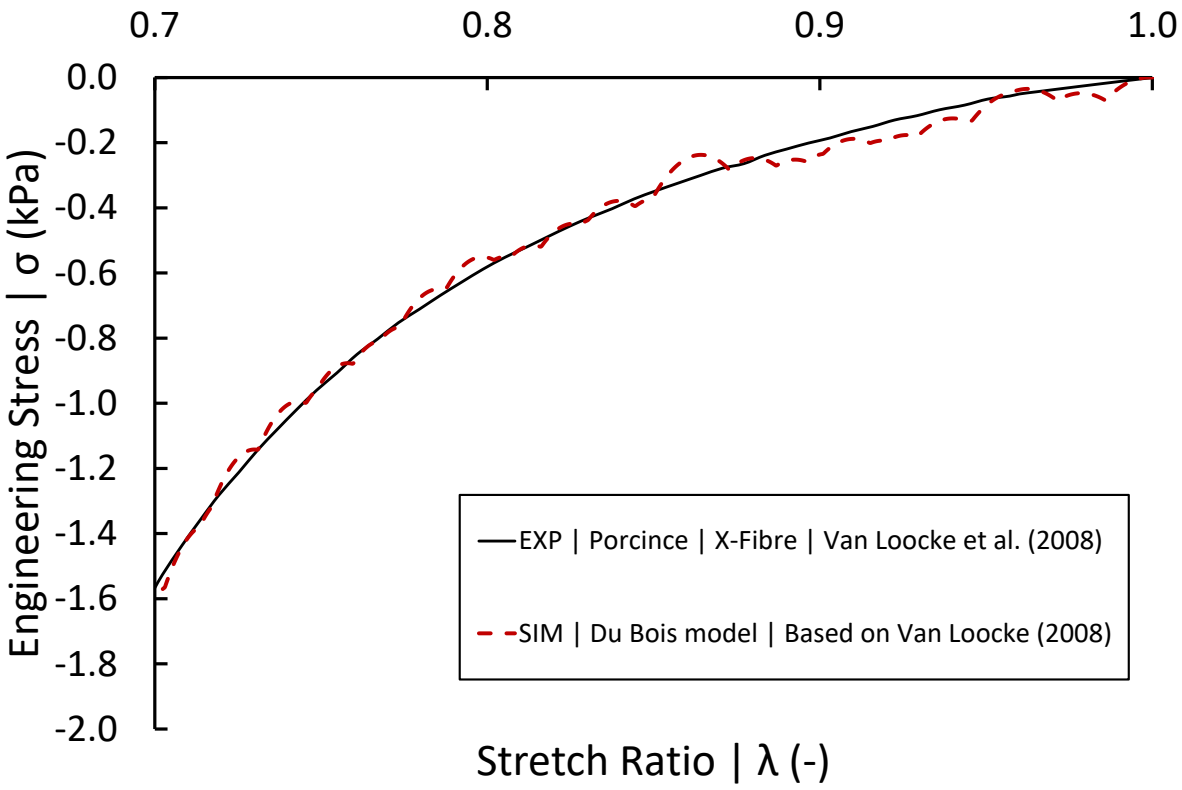

Figure 4-4. Single element in compression. Simulation response and experimental data (detailed view)

The value of shear modulus required by the Blatz-Ko material model was calculated based on the linear portion of the compressive response of the muscle reported by Van Loocke. The goodness of fit provided by this model was quite high, $R^2 = 0.92$. The hyperelastic Du Bois model based on the parameters reported by Van Loocke provided the highest goodness of fit ($R^2 = 0.994$) and was therefore used to represent the passive muscle tissue in compression.

Comment on the Continuity of the Tension-Compression Stress-Stretch Response

The literature review on the passive muscle emphasizes the high level of asymmetry of this tissue in tension and compression. This implies that the shear and elastic moduli for the tensile and compressive loading modes are inconsistent. One of the consequences of this finding is that the tension-compression response of the muscle cannot be described by a single modulus. The shear modulus in tension was $G = 253$ kPa, whereas the same modulus was only $G = 0.94$ kPa in compression. To address this limitation, the hyperelastic Du Bois material model was selected for use with the continuous tension-compression response.

4.1.2 Skin

A selection of constitutive models was tested to recreate the experimental curves of the skin (linear elastic, linear viscoelastic, Blatz-Ko rubber, and Du Bois hyperelastic). Due to the atypical shape of the experimental response of the skin, some constitutive models were incapable of recreating the experimental response of the skin. In that case, the best match was provided by the Du Bois hyperelastic model. The experimental stress-strain response was provided as the input to the model, which allowed the numerical model to recreate the complex behaviour of skin in tension.

Two independent data sets of skin properties were investigated in this study. Both of them were implemented in the FE model with the Du Bois constitutive model. The first set of skin parameters was based on the experimental data reported by Gąsior-Głogowska (Gąsior-Głogowska, 2013). This parameter set was based on the skin excised from a young subject (53 years old). The second set of skin parameters was based on the experimental data reported by Ní Annaidh (2012). This skin was excised from an elderly subject (97 years old). The goodness of fit between the single element model and the experimental data was $R^2 = 0.999$ and $R^2 = 0.998$ for the young and aged models, respectively, demonstrating a good fit (Figure 4-5).

Even though both of the experimental studies were performed on the excised human tissue, the responses demonstrated differences up to 1.97 at a stretch of $\lambda = 1.3$ (Figure 4-5). In general, these discrepancies can be explained by the age difference between the data sets (Section 3.1.2) where the response of the aged tissue was generally stiffer than the younger tissue. The material properties used in the current GHBMC model (Figure 4-5) demonstrated an-initially higher stiffness, and higher stresses up to a stretch of ~1.1. At higher stretches, the stress predicted by the GHBMC model was much lower than both of the reported data sets.

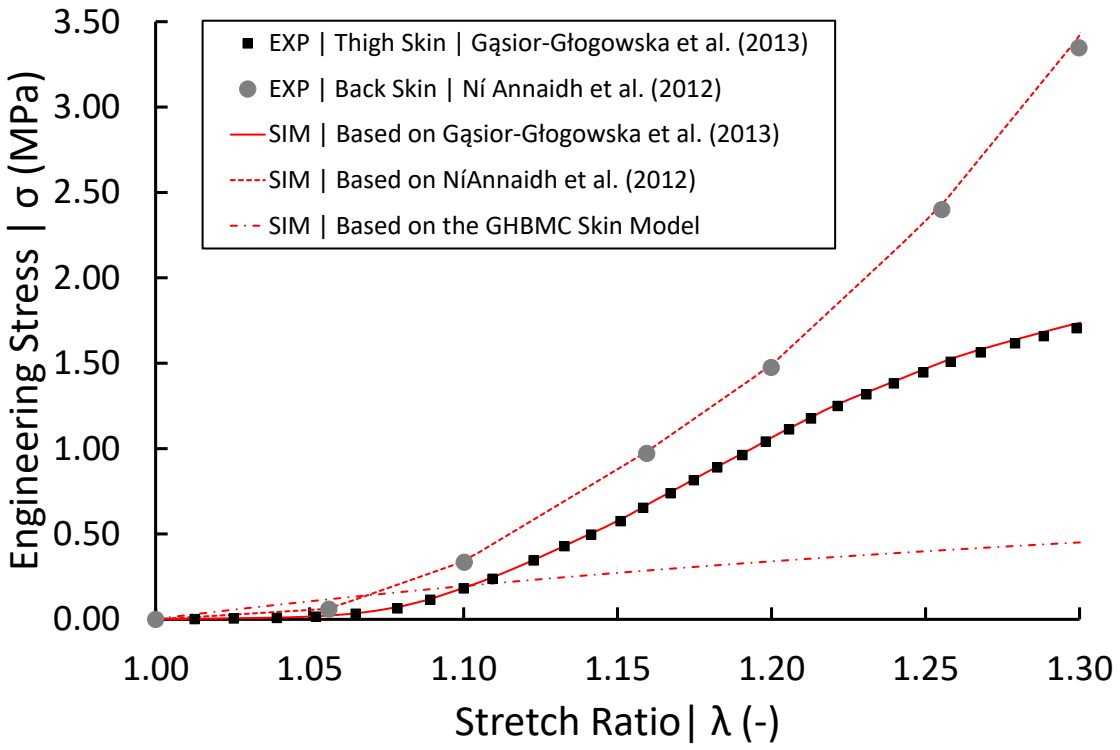

Figure 4-5. Tensile response of the skin: experimental data vs. simulation results (engineering stress-stretch)

4.1.3 Adipose Tissue

The baseline model of the AT was implemented within the GHBMC model using the hyperelastic Du Bois material model. The experimental data showed that the response of the AT to tension and compression is asymmetrical, similar to the behaviour of the skeletal muscle. In the current study AT was modelled using the hyperelastic Ogden model.

The response of the AT implementation from the GHBMC model was stiffer than the available experimental data for both cases, tension and compression. Results of the single element test cases in compression and tension were compared with the experimental data (Figure 4-6). The response of the new model proposed in this study (solid red line) followed the experimental data (solid black line), whereas the currently existing GHBMC AT model (dashed blue line) showed response stiffer than the experimental data of the subcutaneous AT.

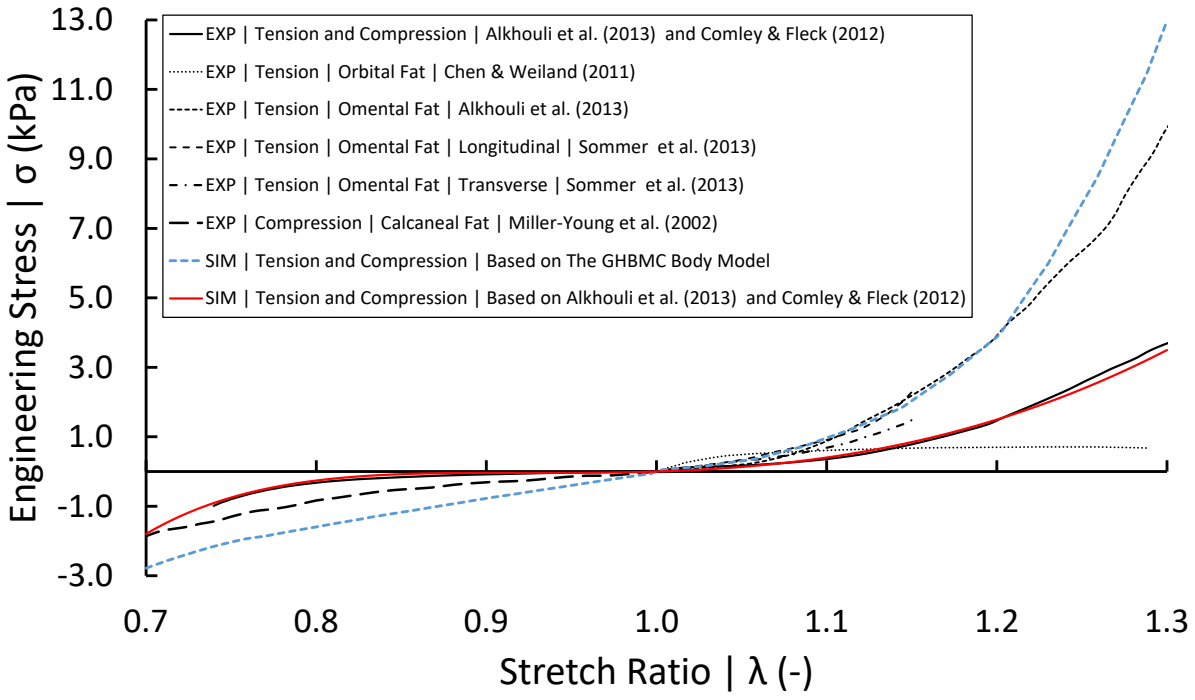

Figure 4-6. Single element response and experimental data | Adipose Tissue

The hyperelastic Ogden model (solid red line) provided very high goodness of fit ($R^2 = 0.998$) with the tensile (Alkhouli, 2013) and compressive (Comley, 2012) experimental data and was therefore used to model the tensile and compressive responses of AT.

4.2 Finite Element Mesh Refinement Study for the SAM

In the current study, the mesh convergence study was performed on SAM for three mesh densities: coarse, medium, and fine, with characteristic elements lengths of 4, 2, and 1 mm, respectively (Figure 3-11). The mesh convergence study was performed based on the methods described in Section 3.3.2. The metric used to calculate the Grid Convergence Index (GCI) was the value of the reaction force at the final displacement of the indenter, d = 20 mm (Table 4-1).

Mesh type	Mesh size [mm]	F_{max} (N)
mesh 0	0	17.13
fine	1	17.28
med	2	17.64
coarse	4	18.87

Table 4-1. Metric used for the mesh refinement study

Mesh 0 presented in Table 4-1 is a representation of an idealized model in which the mesh density tends to zero. The metric value for the theoretical mesh (in this case the peak force at final displacement) is calculated according to the methodology described in Section 3.3.2 of this document.

The results of the mesh convergence study were obtained by using the factor of safety $F_S = 1.25$ that is a recommended value for a three mesh study (Roache, 1994) (Table 4-2).

Grid Refinement Ratio	r	2
Order of Convergence	p	1.773
Factor of Safety	F_S	1.25
Fine-to-Medium Index	GCI_{12}	0.0108
Medium-to-Coarse Index	GCI_{23}	0.0361
$r^P \times GCI_{12}$		0.0368
$r^P \times GCI_{12} - GCI_{23}$		0.000751

Table 4-2. Mesh convergence study results

The values of $r^P \times GCI_{12}$ and GCI_{23} were similar and satisfied the asymptotic regime condition for mesh convergence. A good engineering practice suggests that the error should not exceed 15% (Shah, 2002). In this study, the error associated with the 2 mm FE mesh was 2.97%, therefore the 2 mm mesh was deemed appropriate for simulating the indentation scenario (Figure 4-7).

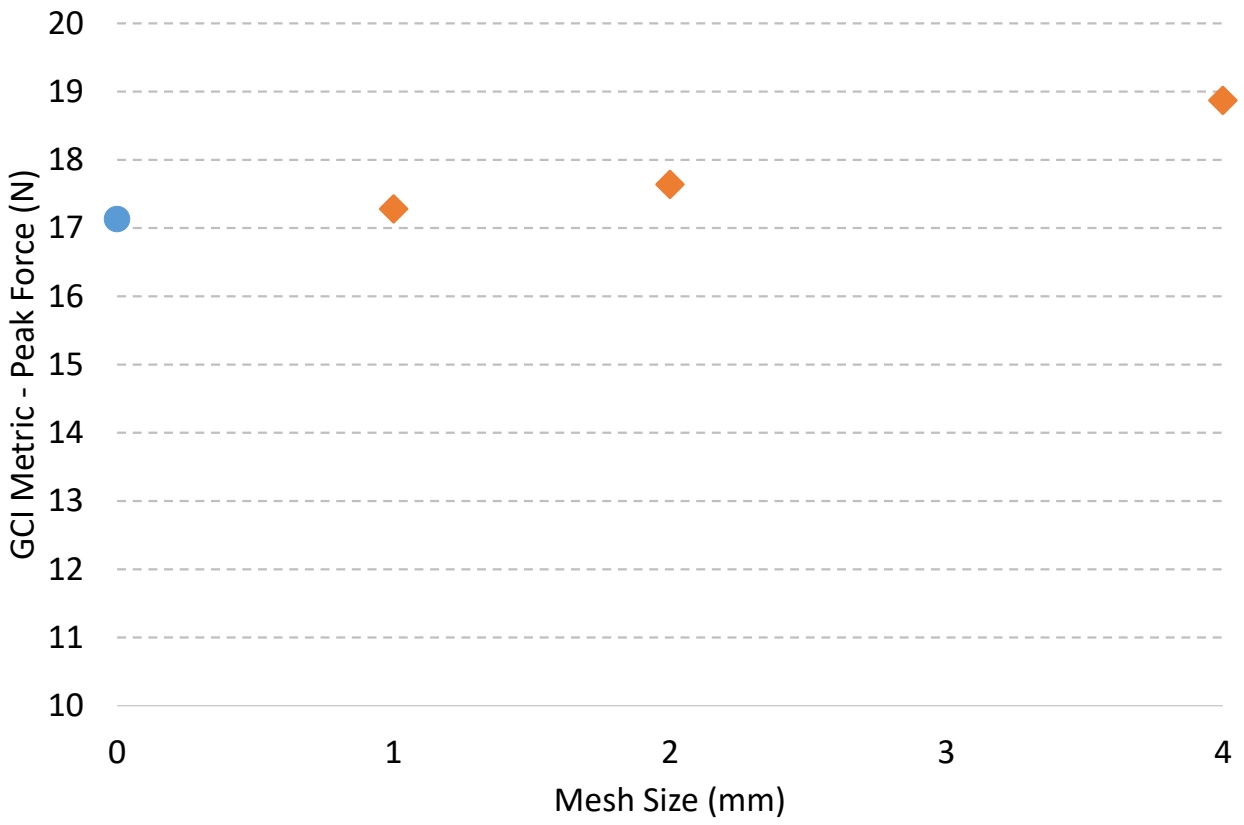

Figure 4-7. Mesh convergence study results. The analytical response of the ideal mesh (blue dot), and simulation responses for 4, 2, and 1 mm mesh size (orange diamond)

4.3 Arm Indentation Simulations

This section describes the results obtained from the arm indentation simulations and presents a comparison of those results with the experimental data. The experimental data which was used to validate SAM was presented by Clemen (Clemen, 2017). The experimental method was repeated in the numerical environment study for all test cases. The SAM was indented, and the force-displacement response was recorded (Figure 4-8).

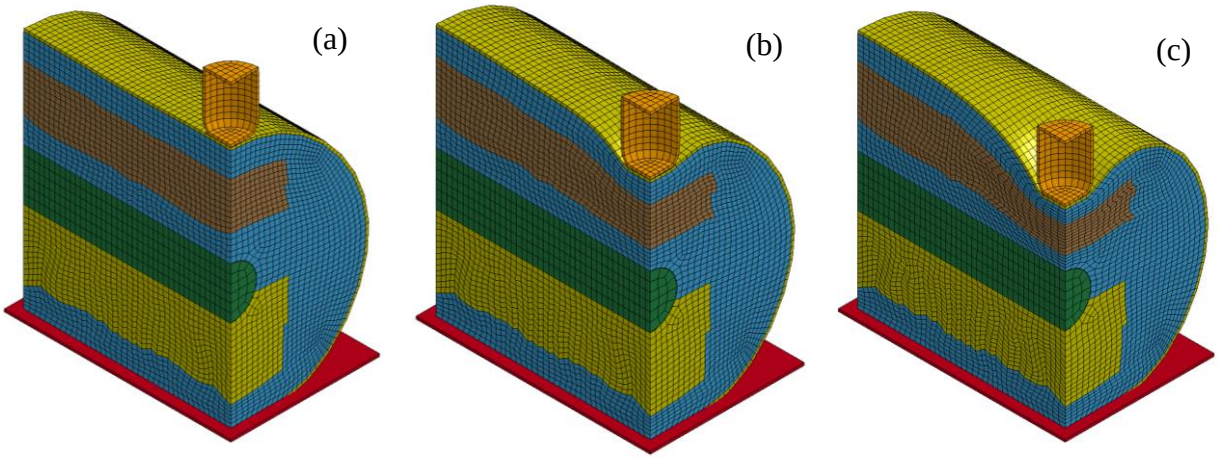

Figure 4-8. Three levels of arm indentation for the SAM: (a) 0 mm; (b) 10 mm; (c) 20 mm

A series of parametric studies were performed to investigate the influence of the following factors on the response of the upper arm to indentation: skin thickness, skin model, skeletal muscle model, and arm diameter.

In the first test series, SAM was tested in two cases: with the original GHBMC soft tissue properties and with the NST properties developed in this study.

Tissue	**Material Model**			
	GHBMC Model	Source	NST	Source
Skeletal Muscle	*MAT_VISCOELASTIC	Karthikeyan (2009)	*MAT_SIMPLIFIED_RUBBER	Van Loocke *et al*. (2008) and Takaza *et al*. (2013)
Adipose Tissue	*MAT_SIMPLIFIED_RUBBER	Gayzik *et al*. (2011)	*MAT_OGDEN_RUBBER	Comley & Fleck (2012) and Alkhouli *et al*. (2013)
Skin	*MAT_VISCOELASTIC	Gayzik *et al.* (2011)	*MAT_SIMPLIFIED_RUBBER	Gąsior-Głogowska *et al*. (2013)

Table 4-3. Data sets used in the indentation simulation

4.3.1 Data Sets used in the Indentation Simulations: GHBMC and NST properties

The first parametric study was performed to compare the response of the arm model to indentation with the soft tissue properties taken from the GHBMC arm model and the NST properties. Both models were indented and the force-displacement was recorded (Figure 4-9).

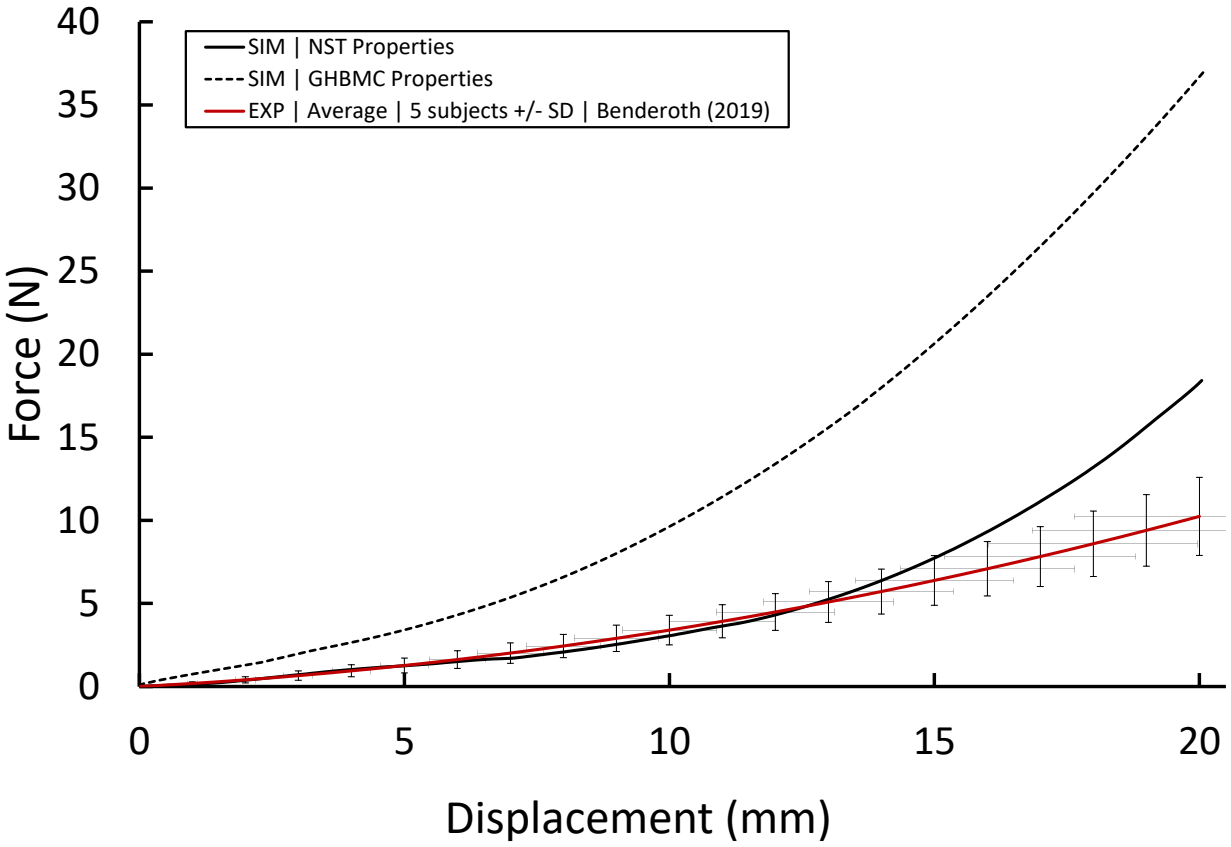

Figure 4-9. Force-displacement response for experiments, and SAM with GHBMC and NST properties

The response of SAM with the GHBMC soft tissue properties was compared with the response of SAM with the NST properties. The work performed by the indenter on the arm model was reported for both simulations (Figure 4-10). Difference ranges between the simulation and average experimental response were provided for both cases (Table 4-4).

It is apparent from this table that the GHBMC tissue properties are stiffer than the experimental data with the difference ranging from 161% to 325%. In contrast, the response provided by SAM with NST properties was found closer to the experimental data, with difference range 2% to 65%.

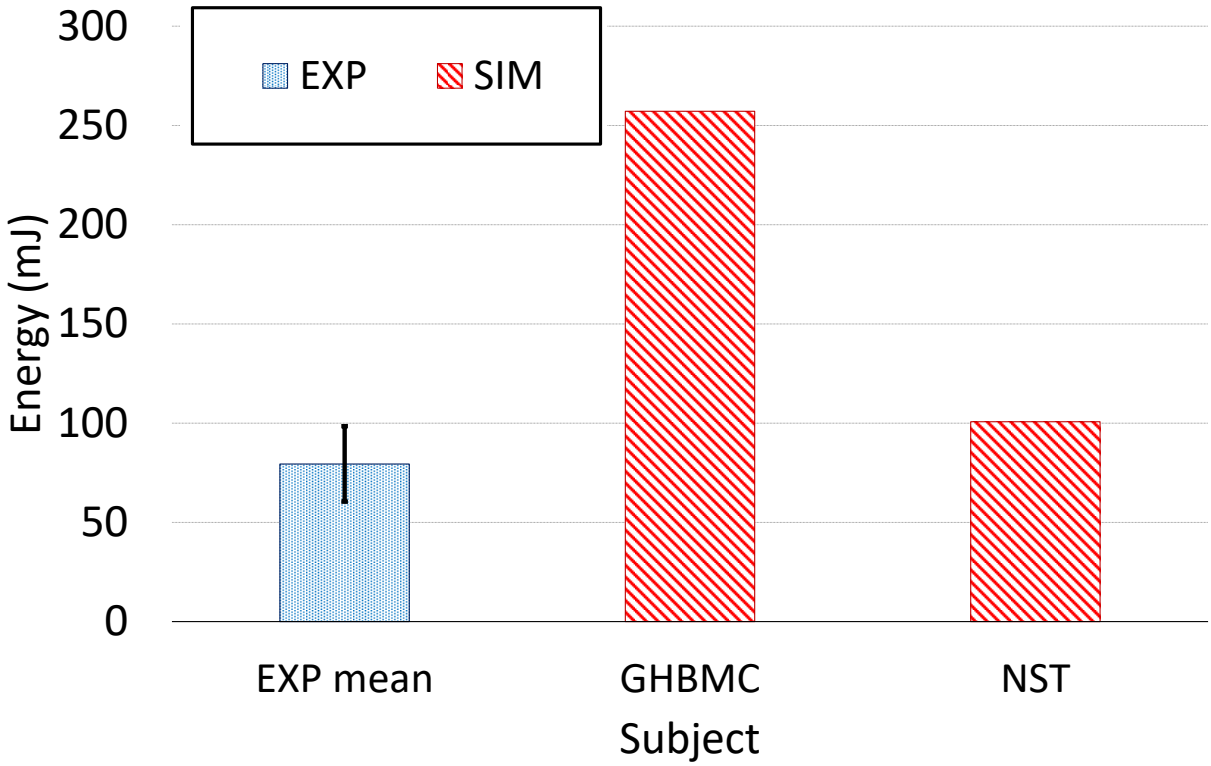

Figure 4-10. Work performed by the indenter for experiments, and SAM using GHBMC and NST properties

Subject	Energy (mJ) (SD)	Error (%) | Mean (range)
EXP mean	79.44 (19.02)	--
SIM | GHBMC	257.13	223.67 (161.14 - 325.56)
SIM | NST	100.69	26.75 (2.27 - 66.65)

Table 4-4. Work performed by the indenter for experiments, and SAM using GHBMC and NST properties

Another metric used for the comparison was the peak force at the final displacement of 20 mm (Figure 4-11). In this case, the GHBMC properties were proven to be overly stiff and overpredicted the force within the error range between 113% and 372% (Table 4-5). On the other hand, the model response with NST properties fit between 33% and 135% of the error margin.

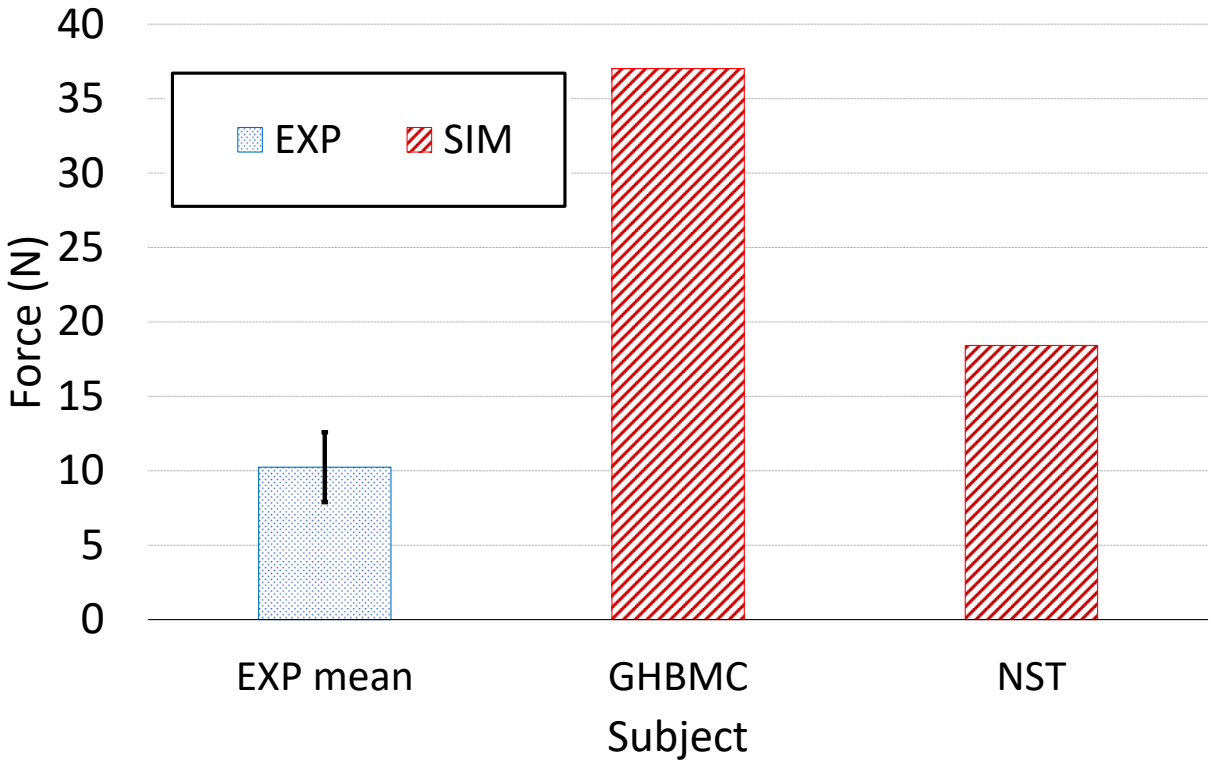

Figure 4-11. Peak force value at the final indenter displacement (20 mm) for experiments, and SAM using GHBMC and NST properties

Subject	F_{max} (N) (SD)	Error (%) | Mean (range)
EXP mean	10.24 (2.35)	--
SIM | GHBMC	37.02	261.55 (194.06 - 369.26)
SIM | NST	18.42	79.88 (46.30 - 133.47)

Table 4-5. Peak force value at the final indenter displacement (20 mm) for experiments, and SAM using GHBMC and NST properties with difference ranges

4.3.2 Influence of the Skin Thickness

In this study, constitutive models were investigated in order to represent the mechanical behaviour of the skin. The influence of those materials was studied. Moreover, the influence of the skin thickness on the indentation response was analyzed.

The most commonly reported thickness of the skin in the human body is t = 2.0 mm. This value depends on the region of the body as well as the age of the subject. The exemplary values were provided in Table 2-3. For the purpose of this study, three thicknesses of the skin were investigated and their influence assessed: 1.5, 2.0, and 2.5 mm.

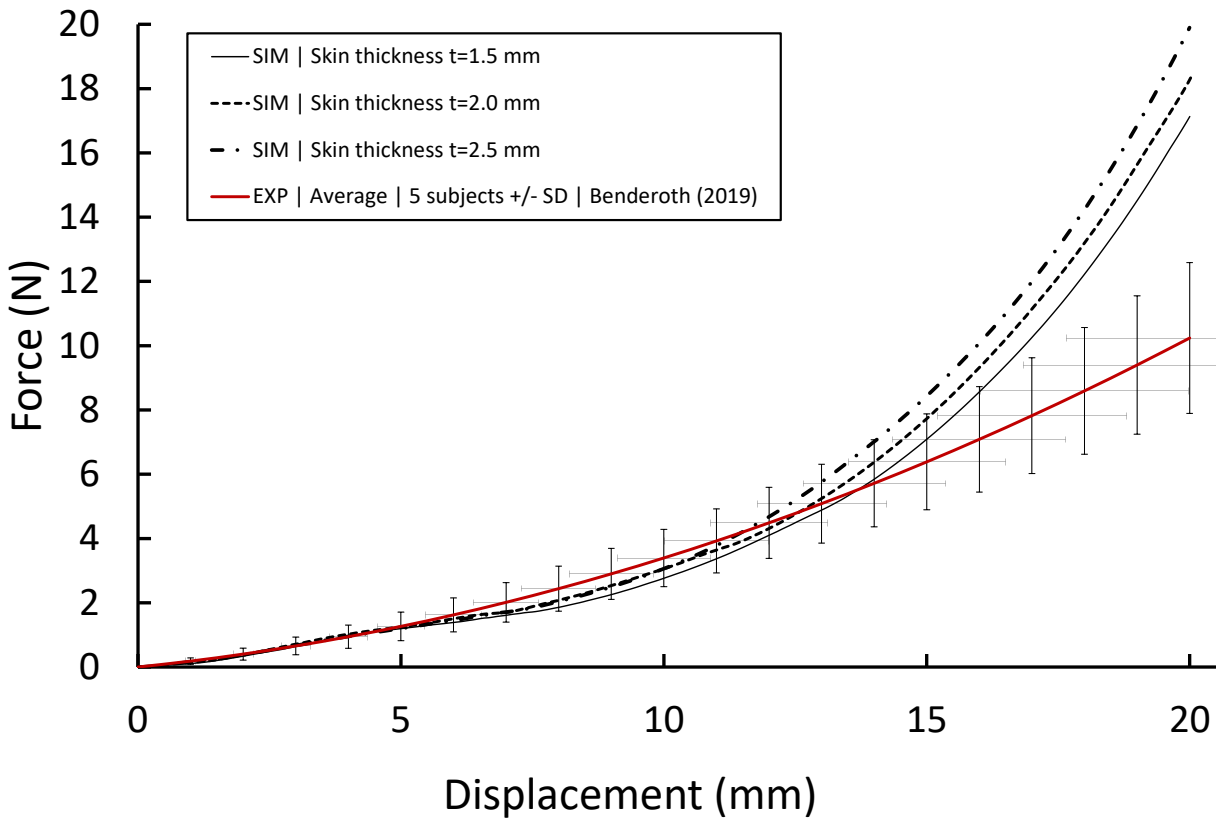

Figure 4-12. Force-displacement response for experiments, and SAM with three skin thicknesses: 1.5, 2.0, and 2.5 mm

The model responses for all cases were reported using two metrics: the work performed by the indenter on the arm model and the peak force at the final displacement of the indenter.

It is clearly seen that the work performed by the indenter increased proportionally to the skin thickness and was equal to 92.34, 100.69, and 106.57 mJ for the model with skin thickness of 1.5, 2.0, and 2.5 mm, respectively (Figure 4-13). In this parametric study, the response of the model with the skin thickness of 1.5 mm was within one SD of the experimental average. The remaining models with skin thicknesses of 2.0 and 2.5 mm overpredicted the experimental response by 2%-67%, and 8%-76%, respectively (Table 4-6).

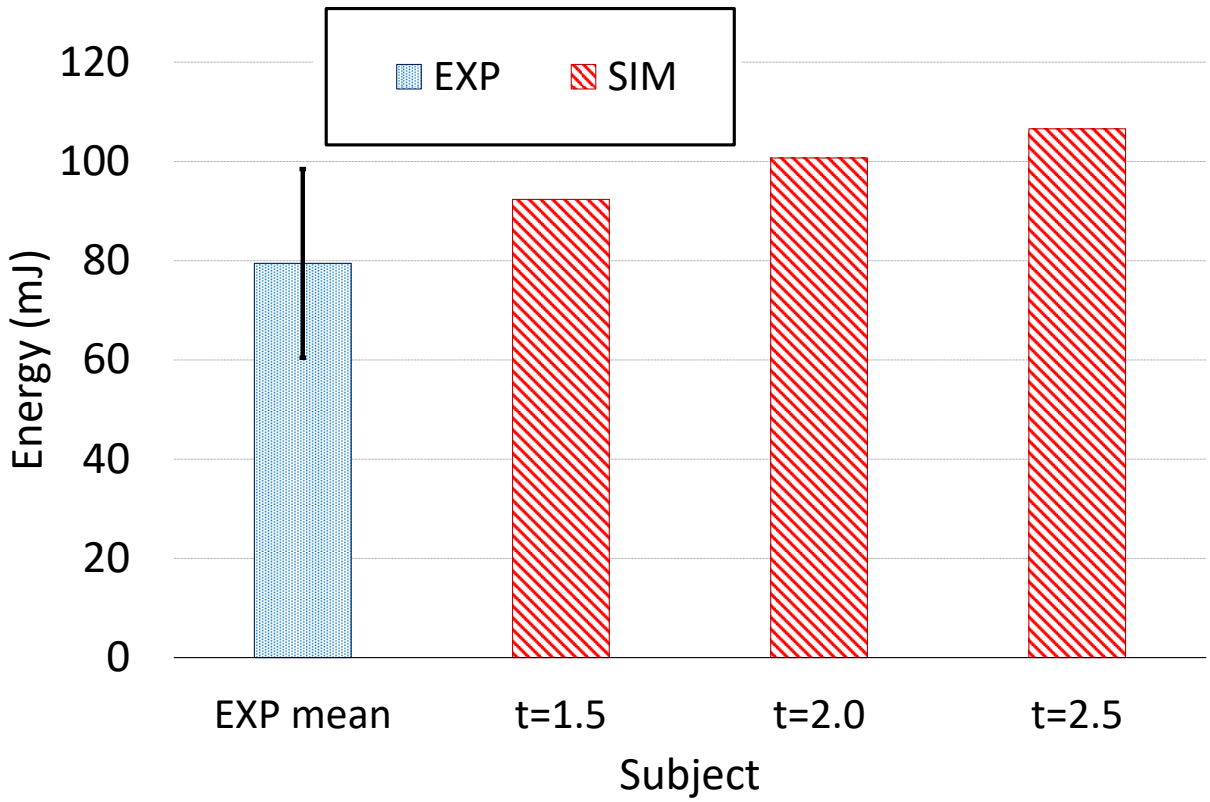

Figure 4-13. Work performed by the indenter for experiments, and SAM with three skin thicknesses: 1.5, 2.0, and 2.5 mm

Subject	Energy (mJ) (SD)	Error (%) | Mean (range)
EXP mean	79.44 (19.02)	
t=1.5	92.34	16.24 (6.21 - 52.84)
t=2.0	100.69	26.75 (2.27 - 66.65)
t=2.5	106.57	34.15 (8.24 - 76.38)

Table 4-6. Work performed by the indenter for experiments, and SAM with three skin thicknesses: 1.5, 2.0, and 2.5 mm

Another metric used to compare the results was the peak force at the final displacement of the indenter (Figure 4-14). In this case, the value of the force increased with skin thickness. The peak force at the final displacement reached 17.13, 18.42, 19.90 N for the skin thickness 1.5, 2.0, and 2.5 mm respectively. All of the simulation responses overpredicted the experimental average. The lowest discrepancy between the numerical response and the experimental data was observed for the model with 1.5 mm skin. In this case, the difference ranged from 36% to 117%. The

discrepancies increased for the model with skin thickness of 2.0 and 2.5 mm, 46%-133%, and 58%-152%, respectively (Table 4-7).

).

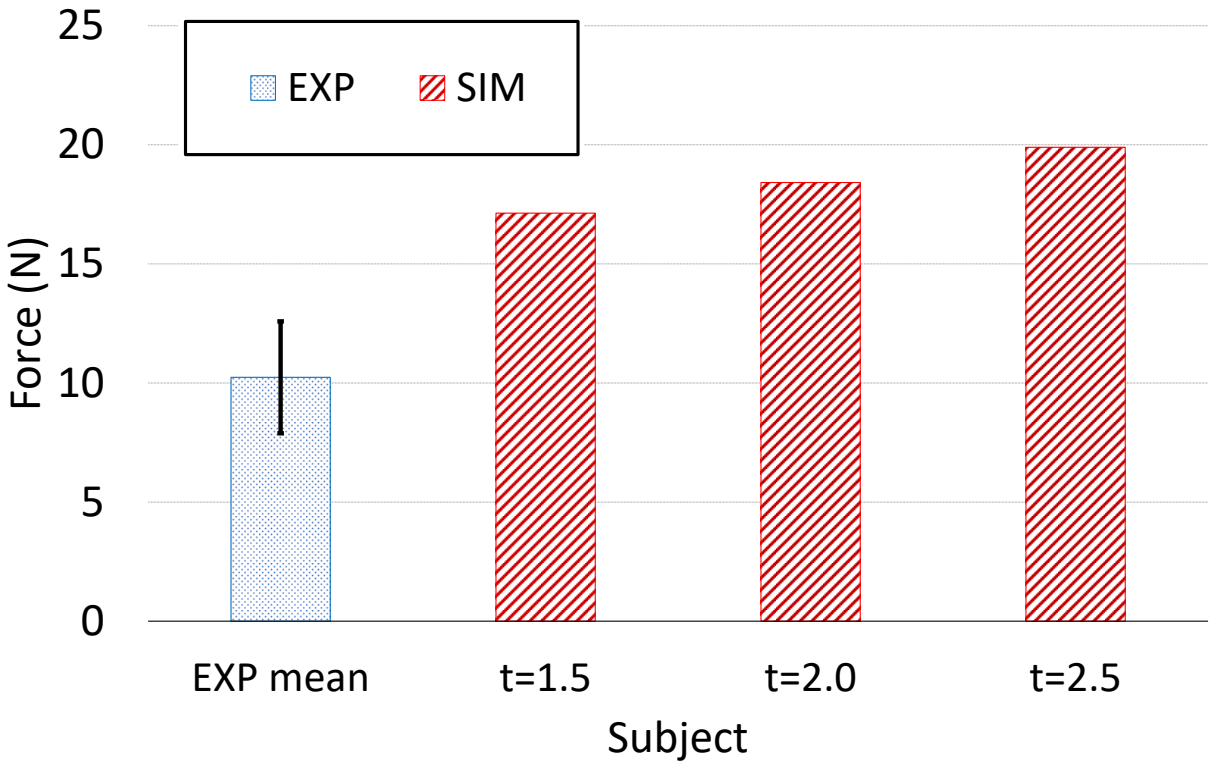

Figure 4-14. Peak force value at the final indenter displacement (20 mm) for experiments, and SAM with three skin thicknesses: 1.5, 2.0, and 2.5 mm

Subject	F_{max} (N) (SD)	Error (%) | Mean (range)
EXP mean	10.24 (3.19)	
SIM | t=1.5 mm	17.13	67.33 (36.09 - 117.18)
SIM | t=2.0 mm	18.42	79.88 (46.30 - 133.47)
SIM | t=2.5 mm	19.90	94.35 (58.07 - 152.25)

Table 4-7. Peak force value at 20 mm indenter displacement for experiments, and SAM with three skin thicknesses: 1.5, 2.0, and 2.5 mm

4.3.3 Influence of the Skin Mechanical Properties with Age

As mentioned earlier, the properties of the human skin alter with age. The hydration level falls from around 70% to 50% in the elderly population (Schmitt, 2019). Moreover, as the skin ages, the amount of elastic fibres decreases causing the loss of skin elasticity (Frances et al., 1990). In this study, two skin models were proposed to assess the differences between young (Gąsior-Głogowska, 2013) and aged (Ní Annaidh, 2012) skin properties.

The properties of the two models were described in detail in Section 4.1.2. The differences between the two skin models were observed on the single element level. This characteristic was carried over to the full arm model. The divergence between the two models was observed right at the beginning of the force-displacement curve. The model with younger skin proved to be more compliant and followed the concave-up curve, a shape similar to the experimental response. In contrast, the response of the elderly skin model was represented by a stiffer curve (Figure 4-15).

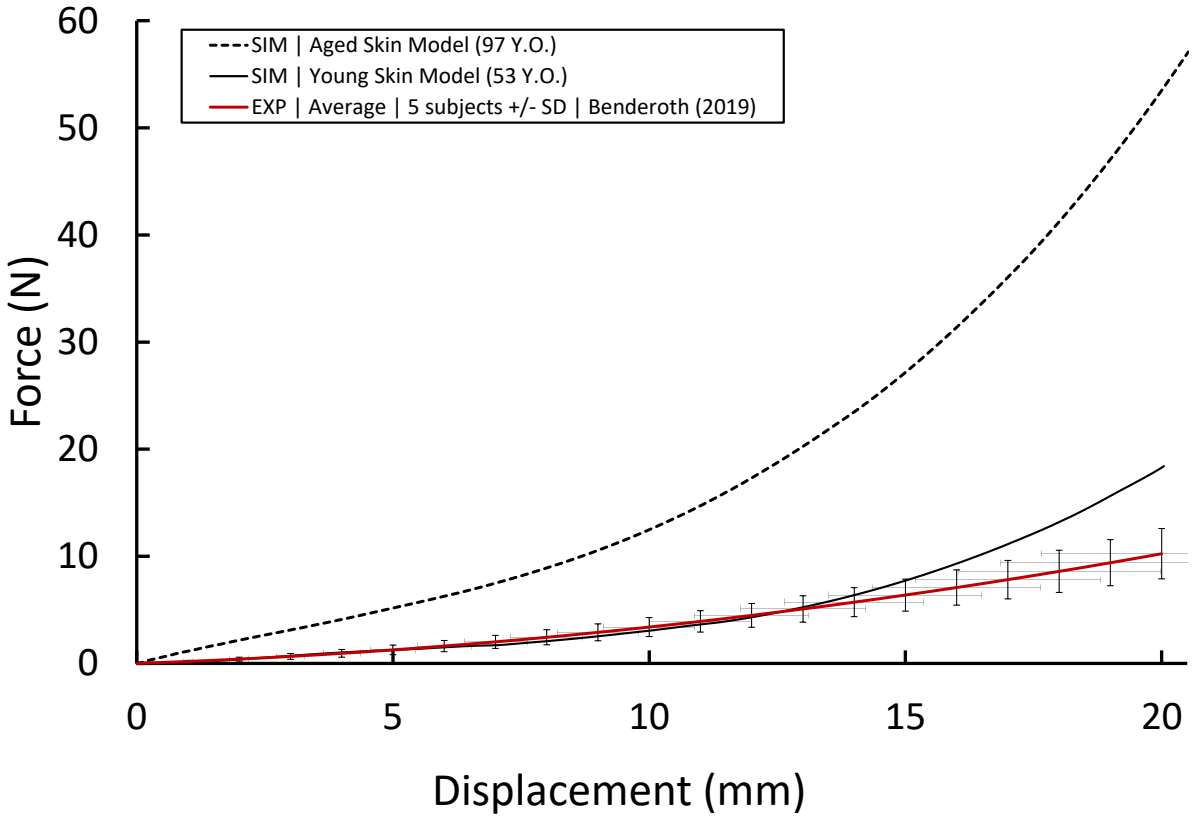

Figure 4-15. Force-displacement response for experiments, and SAM with young and aged skin properties

The work performed by the indenter for the model with aged skin was higher than the work of the model with the young skin by a factor of 3.73 (Figure 4-16). The indenter work for the model with young skin was close to the upper limit of the experimental response with a difference error of 2% (Table 4-8). Surprisingly, this difference is caused only by changing the skin models. The outcomes of this parametric study are further discussed in Section 5.1.2 of this document.

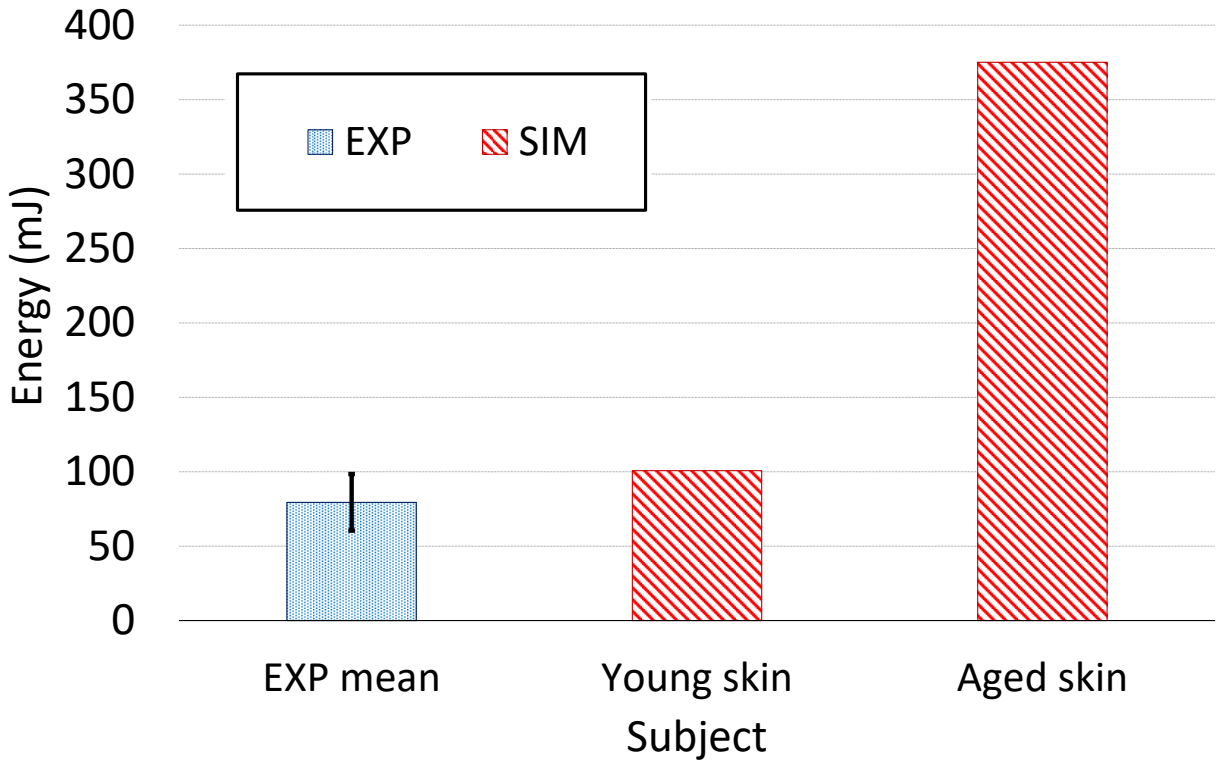

Figure 4-16. Work performed by the indenter for experiments, and SAM with young and aged skin properties

Subject	Energy (mJ) (SD)	Error (%) | Mean (range)
EXP mean	79.44 (19.02)	
SIM | Young skin	100.69	26.75 (2.27 - 66.65)
SIM | Aged skin	375.07	372.14 (280.93 - 520.76)

Table 4-8. Work performed by the indenter for experiments, and SAM with young and aged skin properties

The peak force value was collected from young and aged skin models (Figure 4-17). Both models over-predicted the experimental responses. However, the most surprising aspect of these results is

the scale of the error. The differences between the simulation and experimental responses range between 46% and 133% for the young skin model and 353%-624% for aged skin model (Table 4-9).

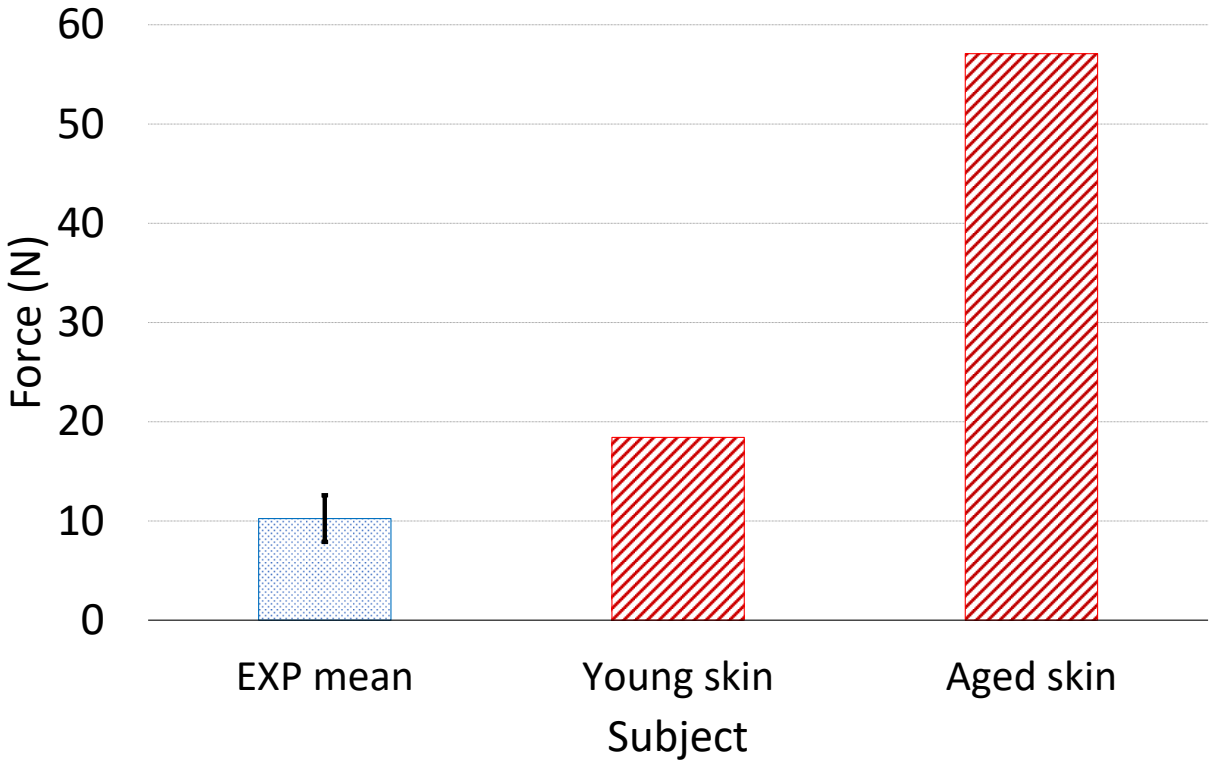

Figure 4-17. Peak force value at the final indenter displacement (20 mm) for experiments, and SAM with young and aged skin properties

Subject	F_{max} (N) (SD)	Error (%) | Mean (range)
EXP mean	10.24 (2.35)	
SIM | Young skin	18.42	79.88 (46.30 - 133.47)
SIM | Aged skin	57.09	457.57 (353.48 - 623.67)

Table 4-9. Peak force value at 20 mm indenter displacement for experiments, and SAM with young and aged skin properties

4.3.4 Influence of the Arm Dimensions for the SAM Model

Arm dimensions display variability among the human population. The variability of the upper arm diameter was described in detail in Chapter 3 (Table 2-6). To assess the influence of different arm dimension a series of three simulations was designed. In this parametric study, three arm models

with different diameters were tested: 70 mm, 100 mm, and 120 mm. Varying arm diameters led to different model responses to indentation. Simulation results for three arm diameters were recorded in the form of force-displacement curves (Figure 4-18).

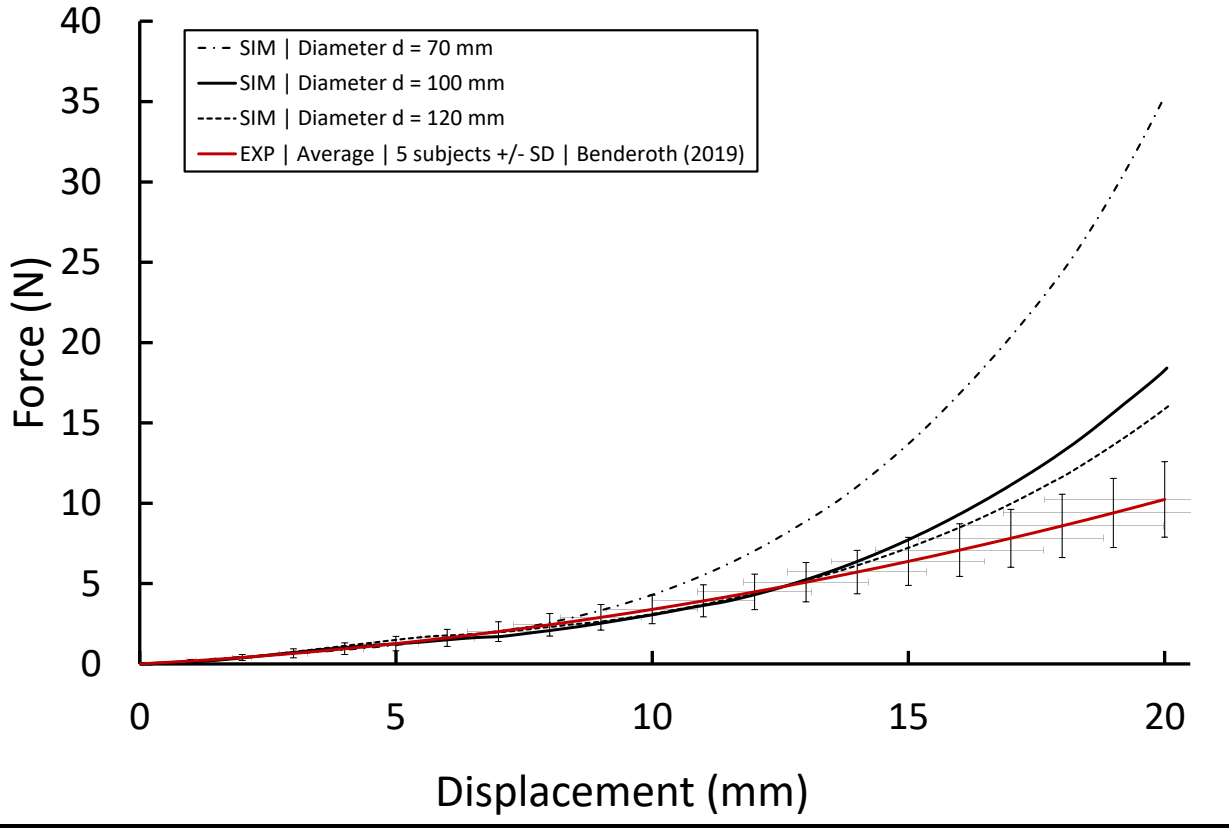

Figure 4-18. Force-displacement response for experiments, and SAM with varying arm diameters: 70, 100, and 120 mm

The simulation results showed an expected trend (Figure 4-19). The work performed by the indenter during indentation decreased as the arm diameter increased. The analysis of the energy chart showed that the 70 mm SAM overpredicted the experimental response 80% to 165%. In contrast, the response of the 100 mm SAM overpredicted the experimental corridors of by 2% to 67%. Finally, the work of the indenter for the 120 mm SAM was within one SD of the experimental data (Table 4-10). Moreover, the force-displacement response of the 120 mm SAM was within one SD of the experimental data up to the 16 mm displacement (Figure 4-18).

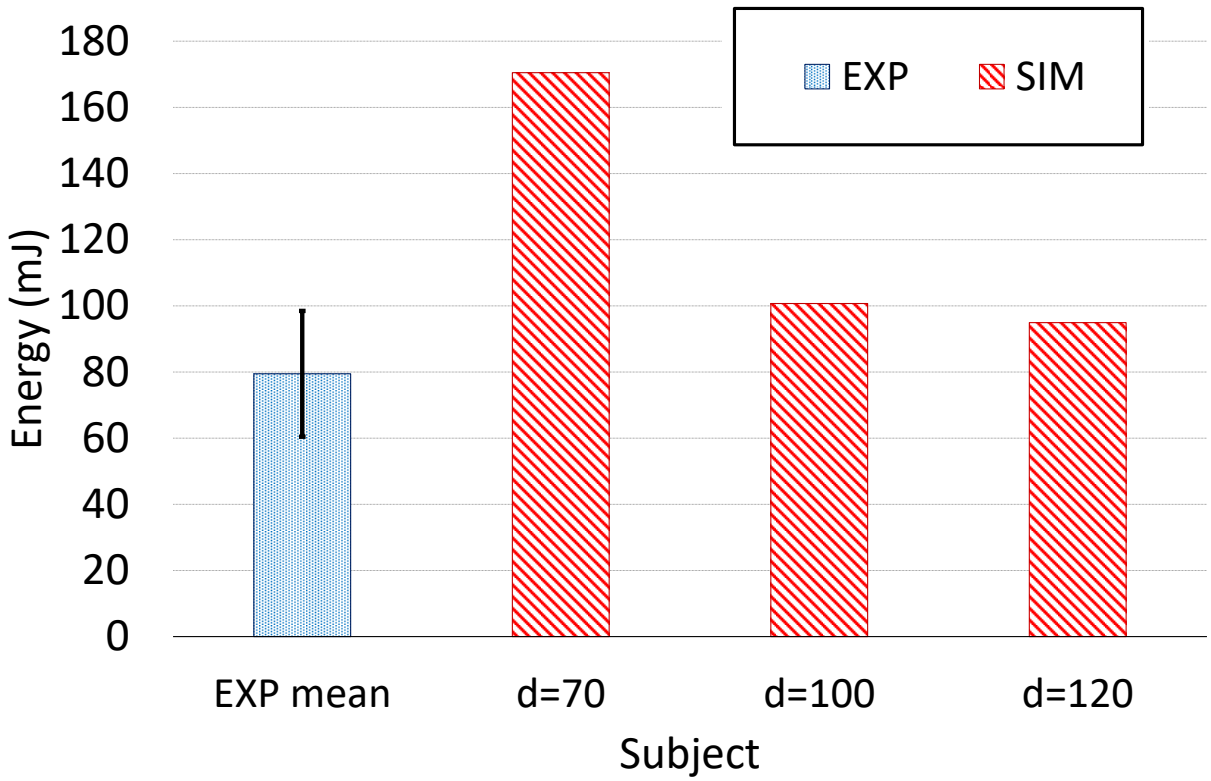

Figure 4-19. Work performed by the indenter for experiments, and SAM with varying arm diameters: 70, 100, and 120 mm

Subject	Energy (mJ) (SD)	Error (%) | Mean (range)
EXP mean	79.44 (19.02)	
SIM | d=70 mm	170.48	114.60 (80.17 - 165.29)
SIM | d=100 mm	100.69	26.75 (2.27 - 66.65)
SIM | d=120 mm	94.91	19.48 (0.31 - 47.70)

Table 4-10. Work performed by the indenter for experiments, and SAM with varying arm diameters: 70, 100, and 120 mm

The value of the peak force decreased as the diameter of the arm increased (Figure 4-20). The highest numerical response was observed for the 70 mm arm model. In this case, the simulation predicted peak force at 35.15 N, whereas the highest experimental value was 12.59 N (upper SD) which yielded a difference of 179%. The peak force value of the 100 mm arm model was 18.42 N which overpredicted the highest experimental value by 46%. The numerical response closest to the experimental data was observed for the 120 mm model. In this case, the difference between

the model (16.03 N) and the highest experimental response (12.59 N) was on the level of 27% (Table 4-11).

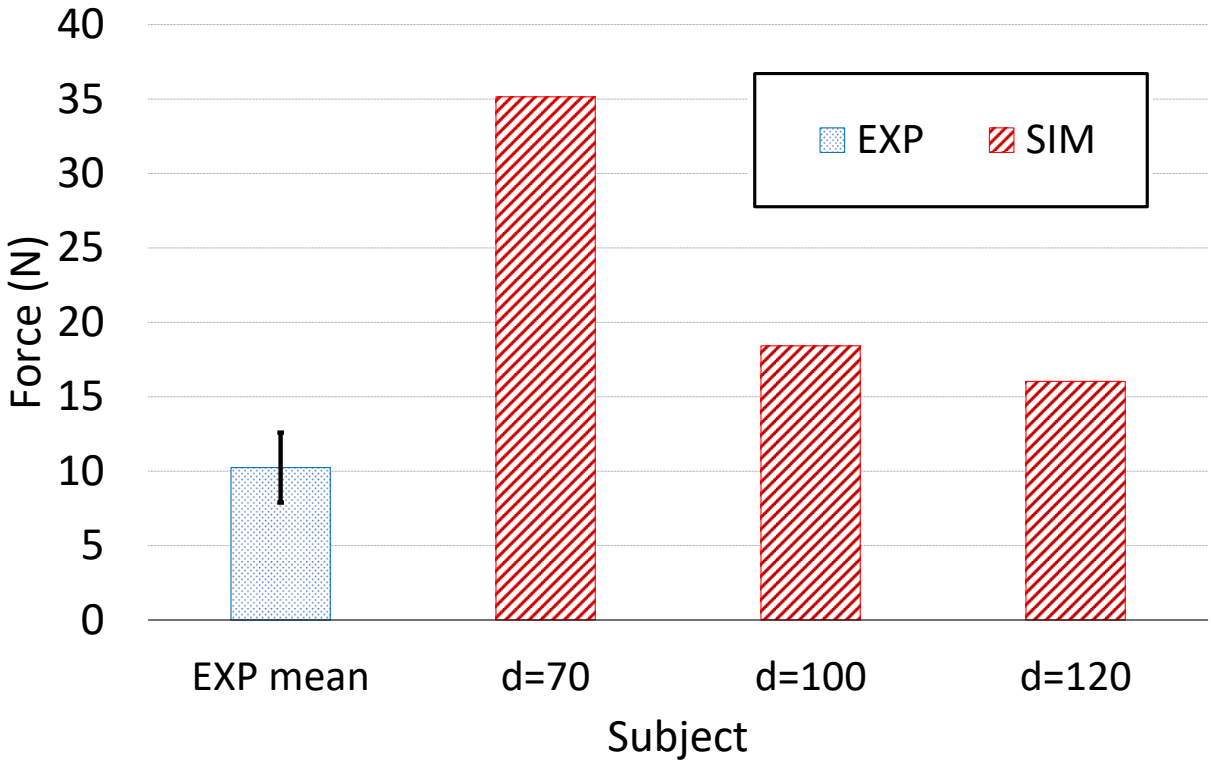

Figure 4-20. Peak force value at the final indenter displacement (20 mm) for experiments, and SAM with varying arm diameters: 70, 100, and 120 mm

Subject	F_{max} (N) (SD)	Error (%) | Mean (range)
EXP mean	10.24 (2.35)	
SIM | d=70 mm	35.15	243.28 (179.20 - 345.54)
SIM | d=100 mm	18.42	79.88 (46.30 - 133.47)
SIM | d=120 mm	16.03	56.58 (27.35 - 103.22)

Table 4-11. Peak force value at 20 mm indenter displacement for experiments, and SAM with varying arm diameters: 70, 100, and 120 mm

4.3.5 Indentation of the GHBMC Arm Model Geometry

Two indentation simulations were performed on the arm model extracted from the GHBMC HBM. In the first simulation, the GHBMC Arm Model with the original GHBMC material properties was used. In the second simulation, the constitutive models were replaced by the NST properties. Both responses were compared with the experimental data (Figure 4-21).

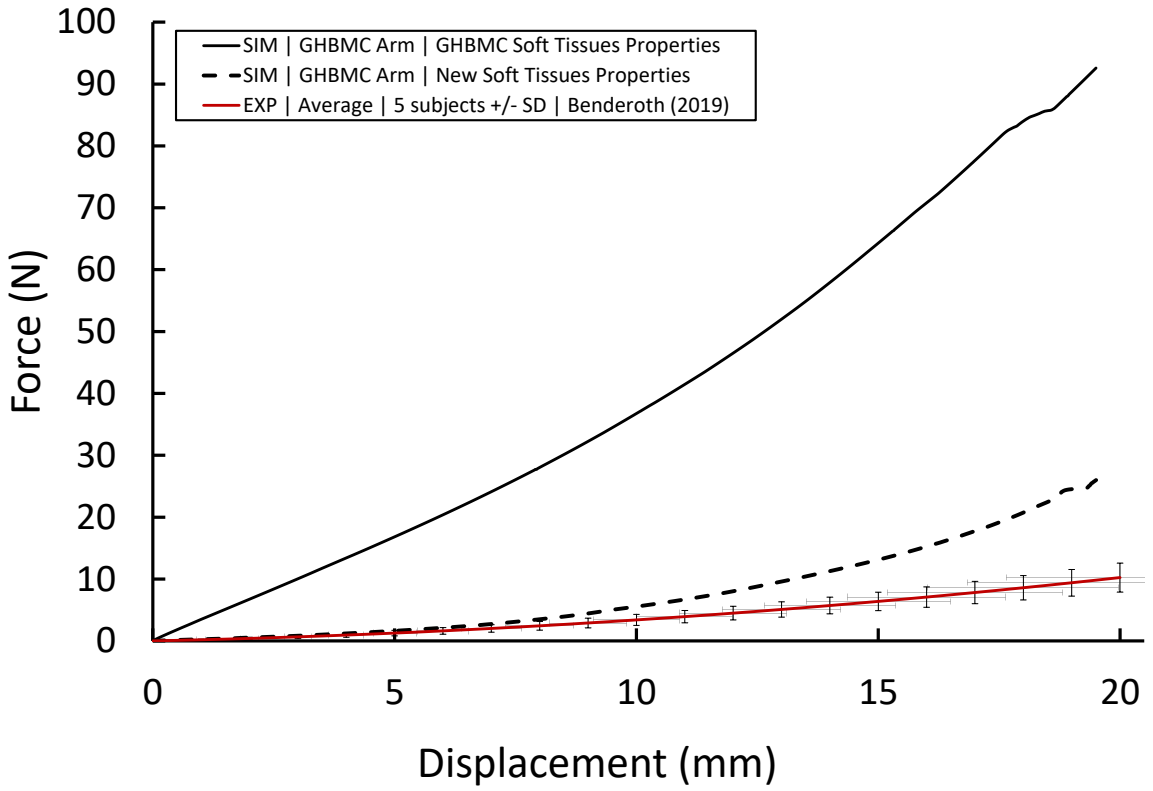

Figure 4-21. Force-displacement response for experiments, and GHBMC arm model with GHBMC and NST properties

The analysis of the energy plot revealed that the GHBMC soft tissue properties were noticeably stiffer than any experimental response (Figure 4-22). The work performed by the indenter for the model with the GHBMC tissue properties overpredicted the highest experimental response by 688%. In contrast, the response of the GHBMC arm model with the NST properties overpredicted the same experimental response by only 56% (Table 4-12).

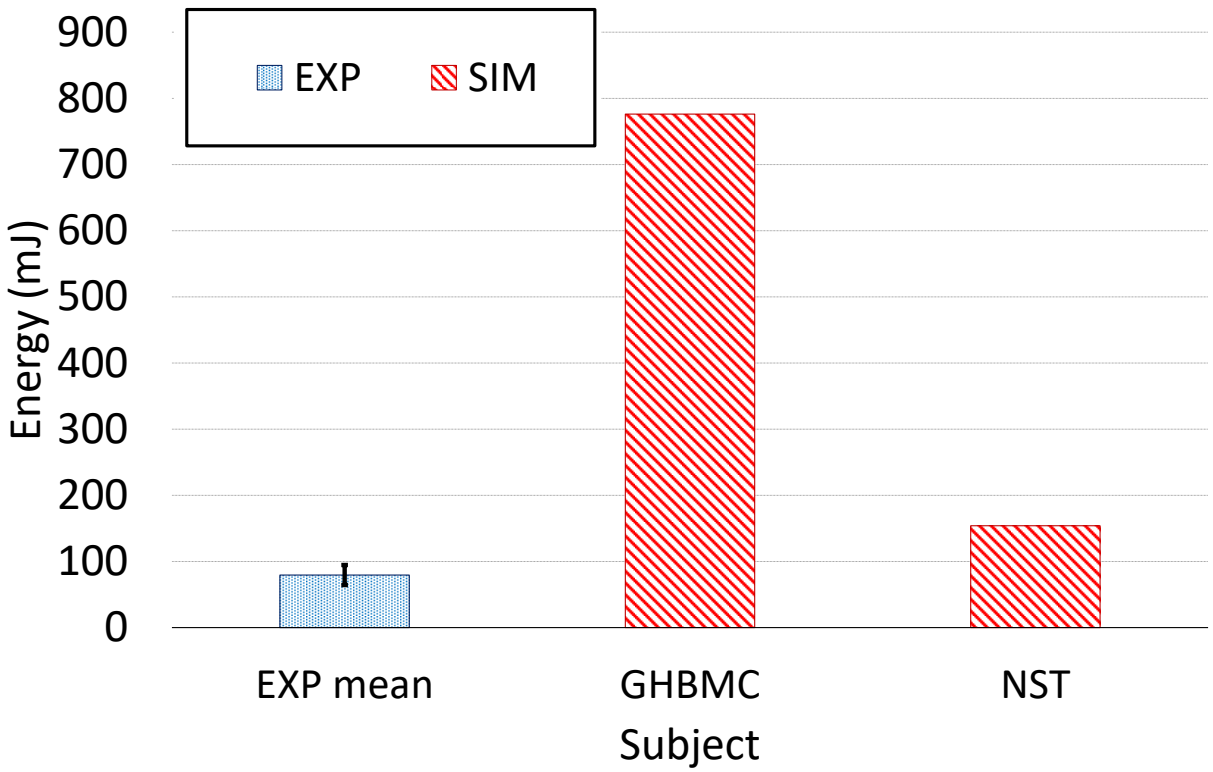

Figure 4-22. Work performed by the indenter for experiments, and GHBMC arm model with GHBMC and NST properties

Subject	Energy (mJ) (SD)	Error (%) | Mean (range)
EXP mean	79.44 (19.02)	
SIM | GHBMC	776.19	877.07 (688.32 - 1184.64)
SIM | NST	153.95	93.79 (56.35 - 154.79)

Table 4-12 Work performed by the indenter for experiments, and GHBMC arm model with GHBMC and NST properties

The peak force value of the model with the GHBMC soft tissue properties was 92.59 N. This value overpredicted the highest experimental value by 635% (12.59 N, upper experimental SD). In contrast, the peak force predicted by the GHBMC arm model with the NST properties was 26.79 N. This value overpredicted the highest experimental response by 112%.

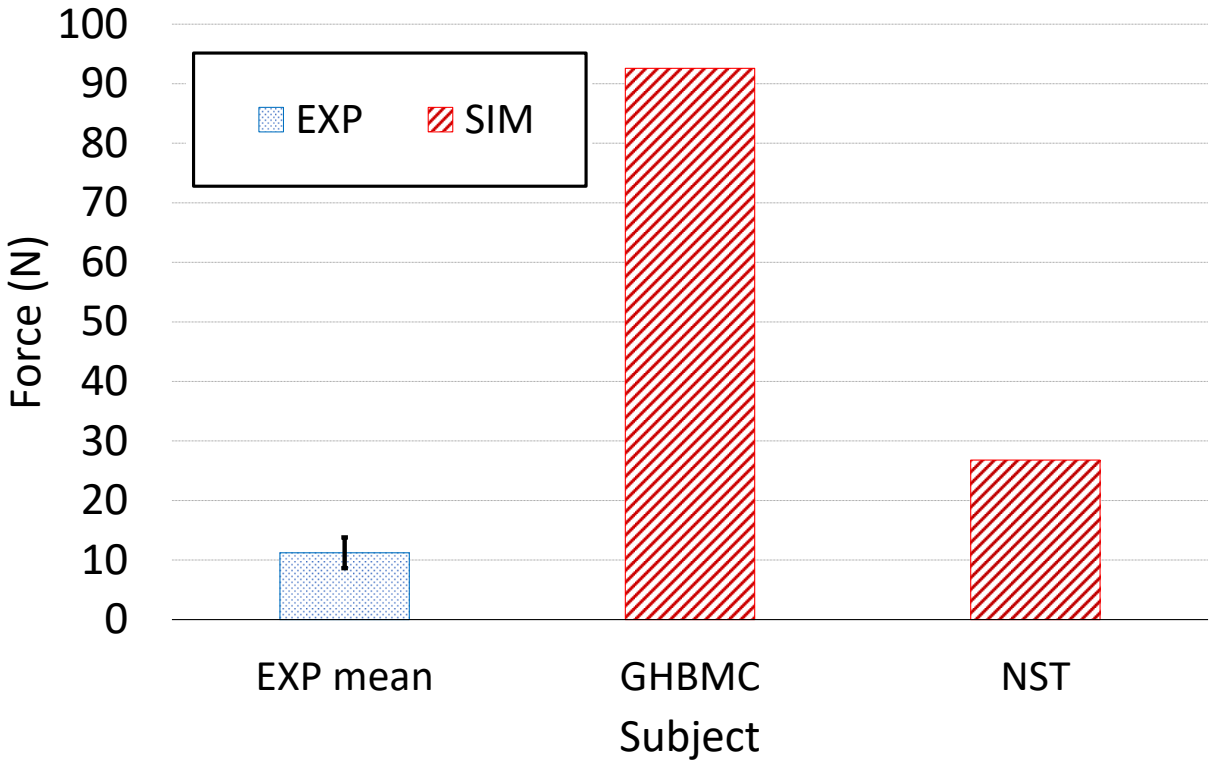

Figure 4-23. Peak force value at the final indenter displacement (20 mm) for experiments, and GHBMC arm model with GHBMC and NST properties

Subject	F_{max} (N) (SD)	Error (%) | Mean (range)
EXP mean	10.24 (2.35)	
SIM | GHBMC	92.59	804.17 (635.40 - 1073.47)
SIM | NST	26.79	161.64 (112.80 - 239.57)

Table 4-13. Peak force value at 20 mm indenter displacement for experiments, and GHBMC arm model with GHBMC and NST properties

This study showed that besides the material properties, the geometry of the model is also an important factor affecting the response of the FE model.

5 Discussion

This study used the FE modelling to assess the behaviour of muscle, skin, and adipose tissue during the indentation loading of the upper arm. The soft tissues were first investigated on the single element level. Then, they were implemented in the arm model. For this study, two types of arm geometry were investigated: SAM, Simplified Arm Model (developed in this study) and GHBMC arm model, which was extracted from the GHBMC HBM. The numerical responses were compared with the experimental data (Benderoth, 2019; Clemen, 2017). Finally, a series of parametric studies were performed using the SAM to address the variability within the human population.

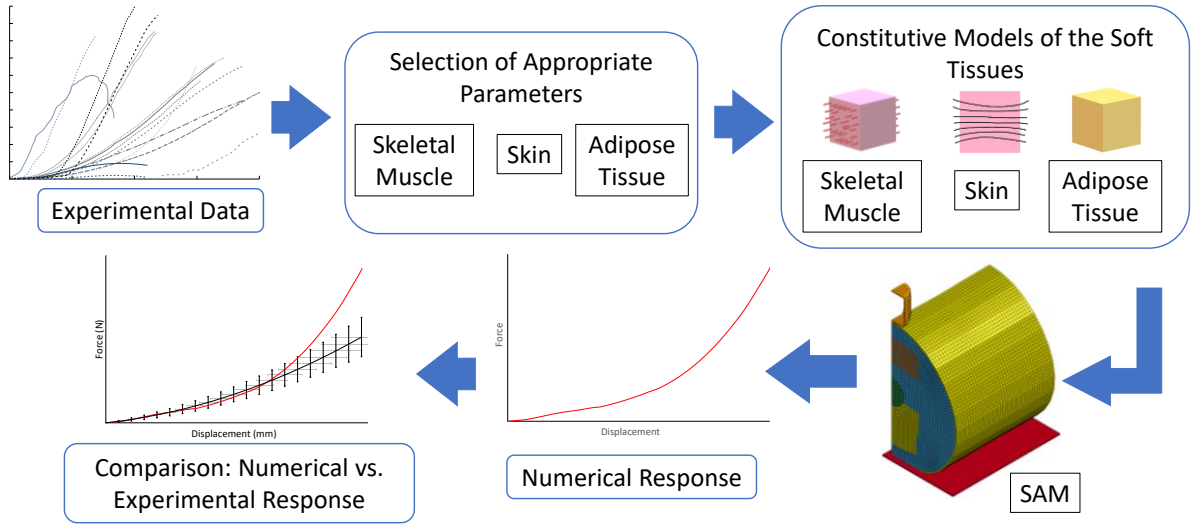

Figure 5-1. The summary of model development

5.1 Contribution of the Individual Soft Tissues to the Upper Arm Indentation

The NST properties were based on five independent data sets retrieved from the literature. To assess their behaviour, the NST properties were compared with the existing GHBMC soft tissue properties. The comparison between the existing GHBMC and NST properties on the individual tissue level revealed that the NST properties exhibit a more compliant compressive response than the GHBMC properties. The reasons for this outcome are described in the following sections.

In the indentation scenario analyzed in this research, the soft tissues of the upper arm were compressed between the bone and the indenter. Therefore, the main type of loading, occurring in the soft tissues, was compression. As a result, it can be concluded that the compressive behaviour

of the investigated tissues has the most influence on the force-displacement response of SAM to indentation.

5.1.1 Skeletal Muscle

In this study, the soft tissues were investigated in the upper arm indentation scenario. During the indentation, the involved tissues were subjected to the compressive mode of loading. Therefore, it was crucial to asses the compressive response of the existing GHBMC muscle properties and the NST muscle properties. As mentioned earlier, the compressive properties of the NST muscle model were based on the literature (Van Loocke, 2008). Data reported by Van Loocke were selected from a plethora of experimental studies on muscle tissue. The major advantages of this data set are: well-described experimental methods, results consistent with other experimental studies and responses recorded at a quasi-static rate. Moreover, this data set reported the compressive responses of the muscle tissue in the fibre- and cross-fibre directions. In the case of this study, the cross-fibre direction was preferred, because the indentation of the upper arm occurs in the direction transverse to the muscle fibres. It can be clearly seen that the compressive response of the GHBMC muscle model is much stiffer than the NST muscle (Figure 5-2).

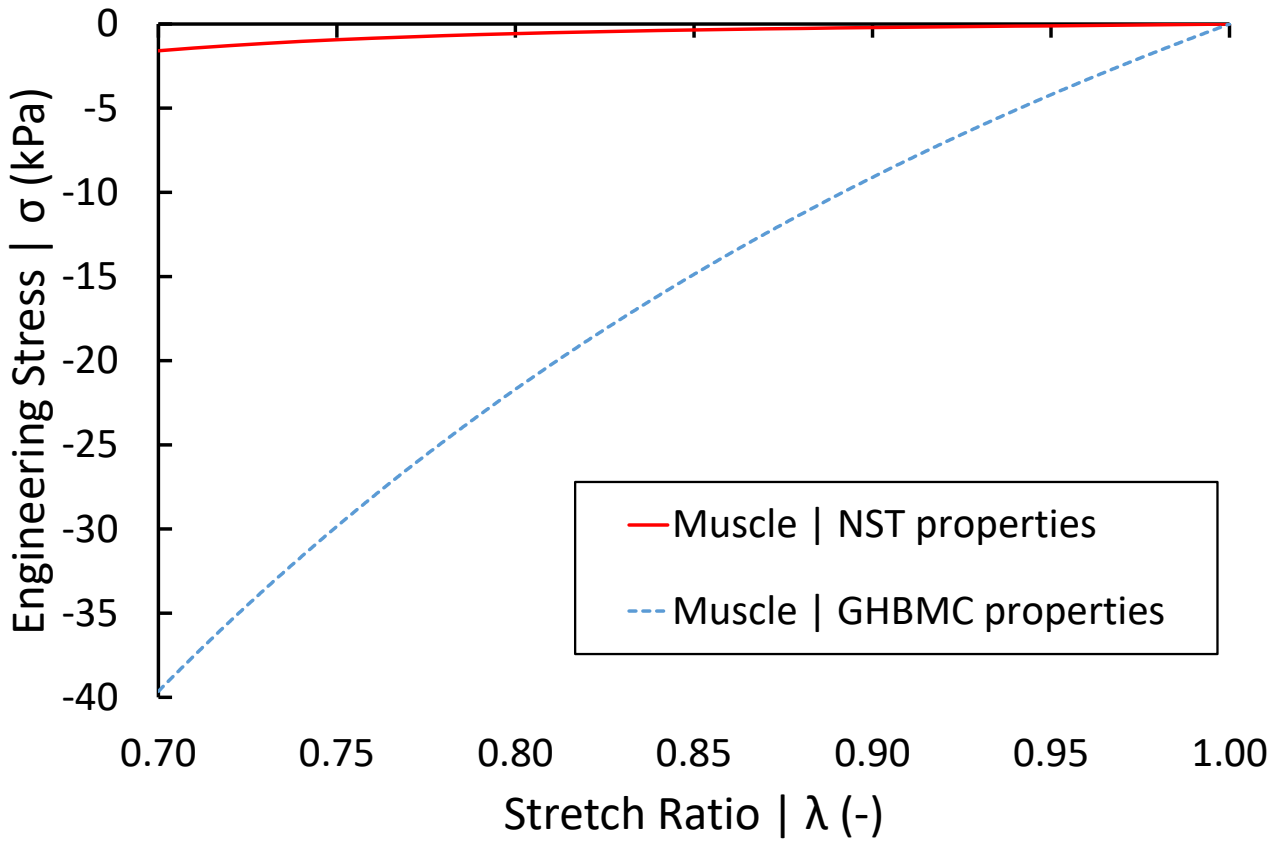

Figure 5-2. Comparison of the compressive stress-stretch response of GHBMC and NST muscle properties

The GHBMC muscle model was proposed by Karthikeyan (Karthikeyan, 2009). Even though it was based on the human tissue, it was inconsistent with other experimental data on muscle compression. Another limitation of this model is the linear response, whereas the actual response of the muscle is hyperelastic. That being the case, the compressive response of the NST muscle was deemed appropriate to be used in the further studies because it was obtained from mammalian muscle tissue and provided a response that remains in agreement with other experimental data performed on the mammalian muscle tissue in compression.

5.1.2 Skin

Skin is the outermost layer of the human body. Therefore, in the case of any external perturbations, skin is the first tissue in contact with an external object. The skin thickness is much smaller than the other dimensions. Therefore, skin can be considered a shell. As such, it was tested in the uniaxial tensile experiment. Skin exhibits orthotropy due to the inclusion of the collagen fibres. The comparison between the GHBMC skin properties and NST skin properties showed that the

response of the GHBMC skin model exhibits linear behaviour and is stiffer than the NST skin, up to a stretch ratio λ ~1.1. However, beyond this stretch ratio, the NST skin response exhibited a complex behaviour described in detail in Section 2.4 (Figure 5-3).

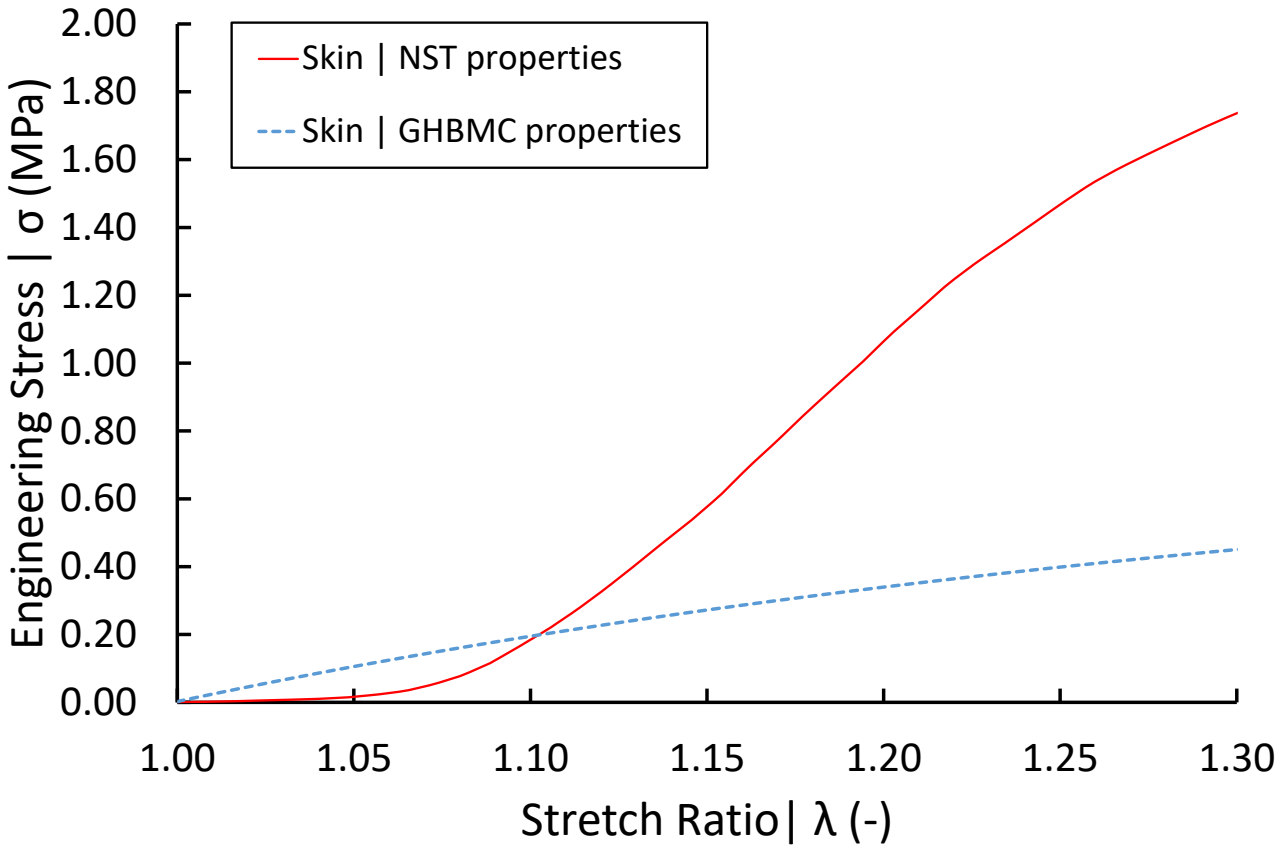

Figure 5-3. Tensile response of skin with GHBMC and NST properties

The NST skin properties were based on the experimental data and are consistent with other experimental findings on skin behaviour (Figure 2-6). Therefore, it was deemed appropriate to use this model for further investigation.

5.1.3 Adipose Tissue

To assess the differences between the GHBMC AT properties and NST AT properties, the compressive responses of both tissues were plotted in a single graph. It is clearly visible that the GHBMC AT is stiffer than the NST AT (Figure 5-4). A possible explanation for this might be the fact that the GHBMC AT model was based on the omental adipose tissue (Gayzik, 2011). The omental AT is localized in the abdomen area and is known to be stiffer than the subcutaneous AT (Alkhouli, 2013). Therefore, to provide a more biofidelic response to be used in the arm

indentation model, the NST AT properties were based on the experimental data reported on the subcutaneous AT.

The upper arm simulation revealed that during the indentation AT was compressed down to a stretch ratio of λ~0.5. Due to the hyperelastic behaviour of AT, the stress developed at this stretch ratio becomes high, thus providing an important contribution to the response of the upper arm to indentation.

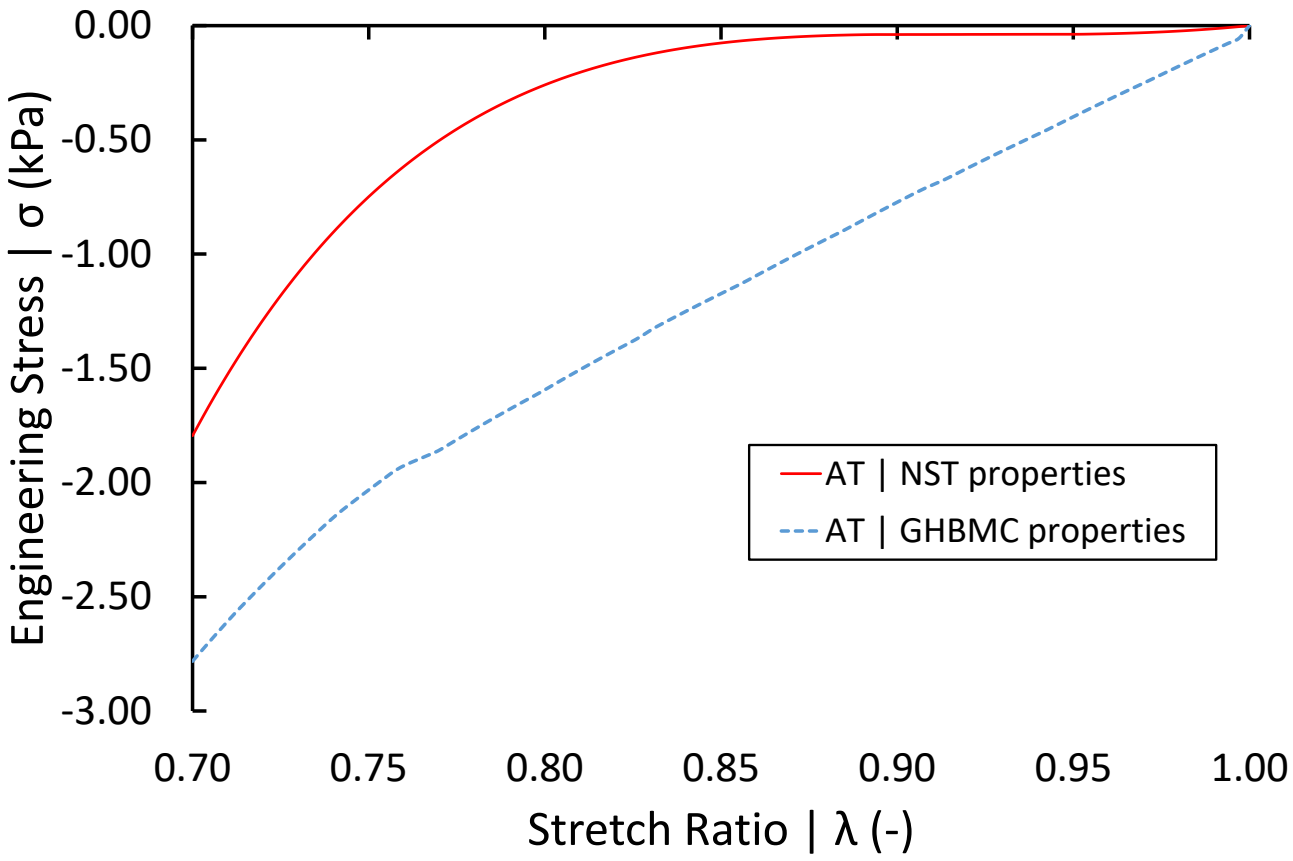

Figure 5-4. Compressive response of the AT with GHBMC and NST properties

5.2 Parametric Studies performed on SAM

To assess the variability within the human population, a series of parametric studies were performed on SAM. These studies addressed the comparison between the existing GHBMC tissue properties and NST properties, skin thickness, skin age, and the diameter of the upper arm.

5.2.1 Comparison between the GHBMC and NST properties

This study set out with the aim of assessing the contribution of the soft tissues to the response of the upper arm to indentation. After being assessed on the single tissue level, these differences were investigated further by testing SAM in the indentation scenario with the GHBMC and NST material properties. The comparison of the force-displacement responses for both simulations (Figure 4-9) demonstrated that the stiffer behaviour of the individual tissues from the GHBMC was carried over to SAM. On the other hand, SAM with NST properties demonstrated a more compliant force-displacement response. As a result, the response of the latter model moved closer to the experimental average. The differences between SAM with GHBMC properties and SAM with NST properties can be explained by the differences on the individual tissue level. The compressive responses of the NST muscle and AT were more compliant compared to the responses of the respective tissues with the GHBMC properties.

In the arm indentation scenario, the main type of loading applied to muscle and AT was compression. The analysis of the simulation revealed that the soft tissues under the indenter were compressed down to the stretch ratio of $\lambda \sim 0.47$ and $\lambda \sim 0.46$ for muscle and AT, respectively. As stated before, the responses of both tissues are hyperelastic. In the case of large compressive stretches, the stress response is very high. Yet still lower than the responses of the GHBMC tissues.

An interesting observation was made on the tissue level. The compressive responses of the NST muscle and AT were plotted on a single graph (Figure 5-5).

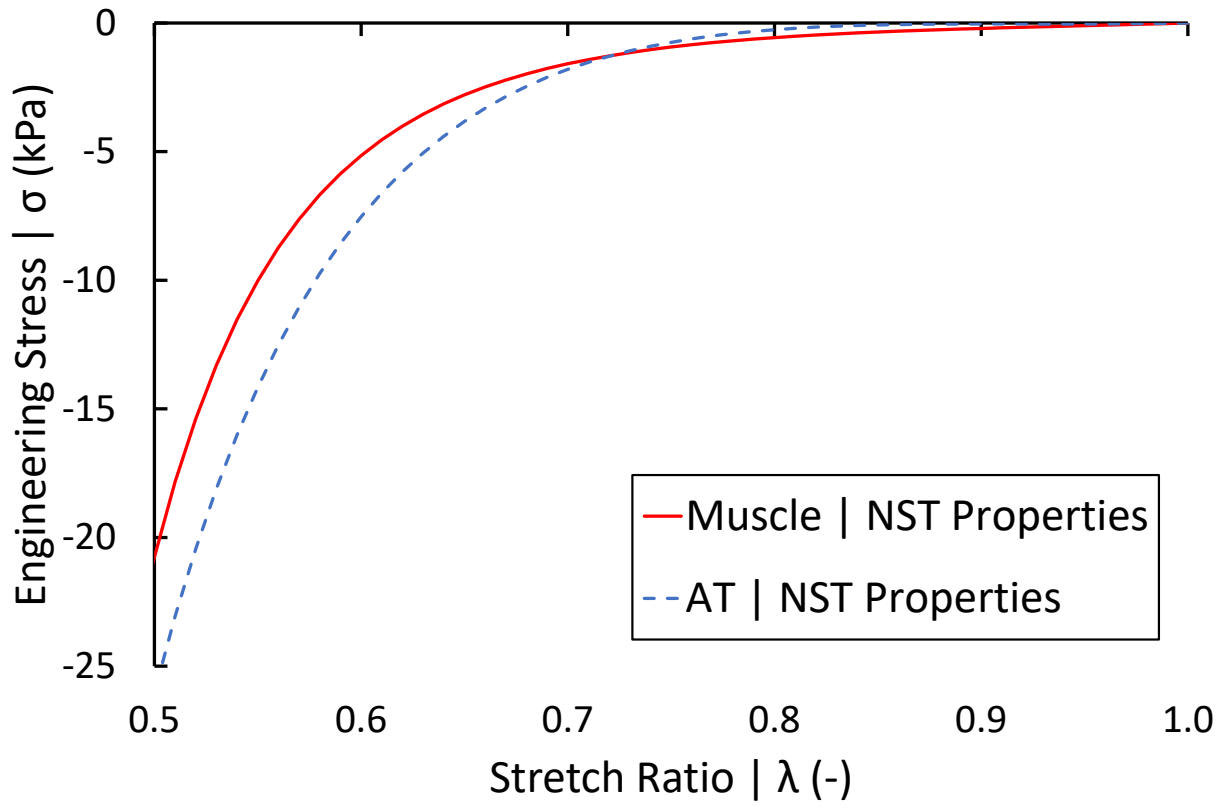

Figure 5-5. Compressive response of NST Muscle and NST AT

The comparison of the stress-stretch responses showed that muscle exhibits a higher stiffness than AT, down to the stretch ratio of λ~0.72. By contrast, these roles changed within the stretch ratio range of λ~ (0.5, 0.72) and AT became a more dominant contributor to the arm indentation response (Figure 5-6).

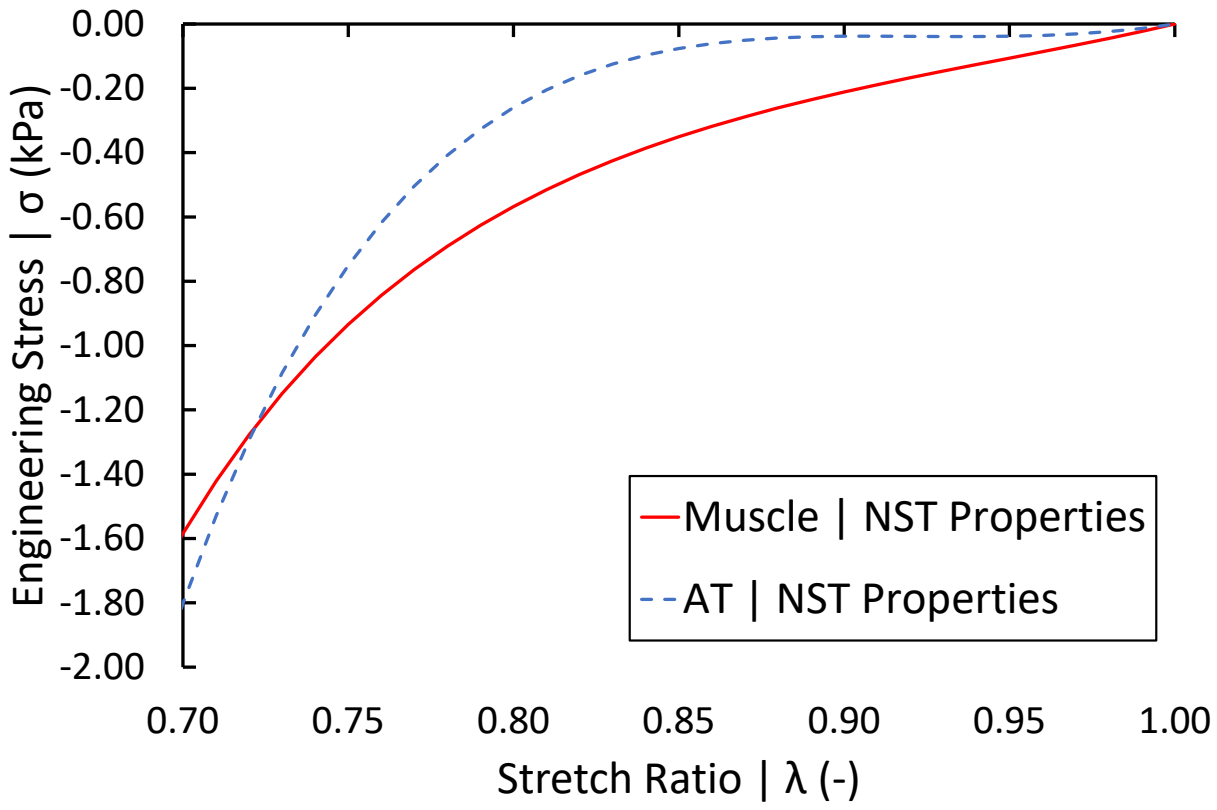

Figure 5-6. Comparison of NST Muscle and NST AT | Stretch ratio 0.7-1.0

Based on this comparison, it was observed that in the indentation scenario both tissues, i.e. muscle and AT, play a similar role. This outcome shows why it is important to select adequate experimental data for the modelled phenomenon. Moreover, the results obtained with SAM and NST properties allow concluding that in this scenario the simplified geometry with appropriate soft tissue properties is capable of predicting the experimental response in a satisfactory manner. The quantitative assessment was presented in Section 4.3.1.

5.2.2 Skin Thickness

The parametric study on the skin thickness revealed that this parameter did not influence the response of SAM to indentation significantly. In the baseline model, the skin thickness was 2.0 mm. To cover the variability within the human population, the thicknesses of 1.5 and 2.0 mm were investigated. These thicknesses were 25% lower and higher than the baseline model (thickness 2.0 mm). However, the percentage change in thickness did not translate to the same percentage change in the response of SAM to indentation. The comparison of the peak force among the three models showed that the skin thickness did not alter the response significantly. Decreasing

the thickness by 25% resulted in a 7% drop in the peak reaction force, whereas increasing the thickness by 25% resulted in an 8% rise in the peak reaction force. A possible explanation for this result might be the mode of loading applied to skin during the indentation. The simulation showed that the stretches in skin during the indentation occur mainly due to the tensile and bending loading. The tensile stretches of skin are relatively small, reaching a maximum stretch of $\lambda \sim 1.1$. Within this stretch ratio, the stress developed by skin remains mostly in the toe region (Figure 5-3) meaning that the stress is low. It was therefore found that changing the skin thickness by +/- 25% will not affect the force-displacement response of SAM significantly (Table 5-1).

Test Case	F_{max} (N)	Difference w.r.t. baseline (%)
SIM | t=1.5 mm	17.13	6.99
SIM | t=2.0 mm	18.42	-
SIM | t=2.5 mm	19.90	8.03

Table 5-1. Peak force difference for SAM with different skin thicknesses (1.5, 2.0, and 2.5 mm)

5.2.3 Comparison between Young and Aged Skin Model

Two independent data sets were investigated to model skin behaviour (Gąsior-Głogowska, 2013; Ní Annaidh, 2012). The selection of these particular experimental responses was dictated by the following factors. In both cases, the skin samples were excised from the PMHSs. Since this study focused on the indentation of the human upper arm, it was deemed more appropriate to use the human skin properties, instead of the animal samples. The literature review indicated differences in mechanical responses between human and animal skin tissue. In most cases, the tensile response of the animal skin was inconsistent with the response of the human skin (Shergold, 2006). Another reason for selecting these data sets was to assess the differences between young (Gąsior-Głogowska, 2013) and aged (Ní Annaidh, 2012) skin properties.

The comparison of these two data sets on the tissue level showed that the tensile response of the aged skin exhibits higher stiffness than the response of the young skin properties (Figure 4-5). This behaviour can be attributed to the fact that the hydration of the human body decreases with age, thus decreasing the elasticity of the skin. The loss of elasticity of the skin is also related to the decreased amount of elastin fibres in the aged skin (Zhang & Duan, 2018).

The differences between the two skin properties were also assessed in the arm indentation scenario. Since the aged skin model exhibited stiffer response on the individual tissue level, the response of the upper arm with aged skin was also expected to be higher. What was surprising was the magnitude of the difference between the two models. The peak force at the final displacement of the indenter of 20 mm for the aged skin model was 209% higher than the peak force of the young skin model. A possible explanation for this might be the fact that the arm model was only partially *aged*. Of three soft tissues within SAM, only the skin was aged, whereas the remaining tissues, i.e. muscle and AT, kept their original properties. Justification of partial ageing of SAM follows. Muscle testing is usually performed on the excised animal tissue. That being the case, the age of an animal cannot be directly recalculated to the age of a human. By contrast, in the case of skin, there were two readily available data sets with a clear distinction between young and aged specimens obtained from human PMHS. Because of that, it was deemed appropriate to investigate the differences between the two data sets of skin. For future reference, to model the behaviour of the aged arm during indentation, it is highly recommended to use material properties representative of the elderly population.

5.2.4 Arm Diameter

Arm dimensions vary among the human population. They depend on factors like age, stature, whole body dimensions, or athletic condition. To assess the influence of the arm diameter on the responses to indentation, a parametric study was performed on SAM with three different diameters: 70, 100, and 120 mm.

The baseline diameter of SAM was 100 mm. The lower bound of the diameter was set to 70mm. To assure consistency, the diameter of the bone was also scaled by the factor of 0.7. The overall decrease in the diameter caused also the decrease in the amount of soft tissues. The force-displacement response observed for SAM with 70 mm was higher than the baseline response (SAM with 100 mm diameter). This observation was confirmed by the comparison of the peak forces at the indenter displacement of 20 mm. SAM with a diameter of 70 mm predicted the peak force of 35.15 N, whereas the responses of the baseline SAM (100 mm diameter) predicted only 18.42 N (91% difference) (Table 5-2).

Test Case	Fmax (N)	Difference w.r.t. baseline (%)
SIM | d=70 mm	35.15	90.81
SIM | d=100 mm	18.42	-
SIM | d=120 mm	16.03	12.97

Table 5-2. Peak force difference for SAM with different diameters (70, 100, and 120 mm)

The difference between the numerical responses can be attributed to the lower amount of the soft tissues encompassing the bone in SAM 70 mm. Therefore, there was a lesser amount of the soft tissue to be compressed between the indenter and the bone. As a result, the stiffness of the bone might have played a dominating role in the response to indentation.

The upper bound of the SAM diameter was 120 mm. In contrast to the SAM 70 mm and the baseline SAM, the response of SAM 120 mm was more compliant. The peak force at the maximum indenter displacement of 20 mm was 13% lower than the baseline response (16.03 N compared to 18.42 N) (Table 5-2). In the case of SAM 120 mm, there was more a higher amount of soft tissue between the indenter and the bone. This means that the compression occurred mostly in the soft tissue region and the influence of the bone was not as dominant as in the case of SAM 70 mm.

The numerical results for three SAM diameters (70, 100, and 120 mm) were also compared with the average experimental force-displacement response provided by Clemen (Benderoth, 2019; Clemen, 2017). It is clearly seen, that the response of SAM 70 mm overpredicted the average experimental response. The force-displacement responses of the two remaining models, SAM 100 mm and SAM 120 mm, approached the average experimental response, although they overpredicted the peak force by 46% and 27% respectively. Interestingly, when compared to the responses of the individual subjects, the numerical results of SAM 100 mm and SAM 120 mm are within one SD of the experimental results (Figure 5-7).

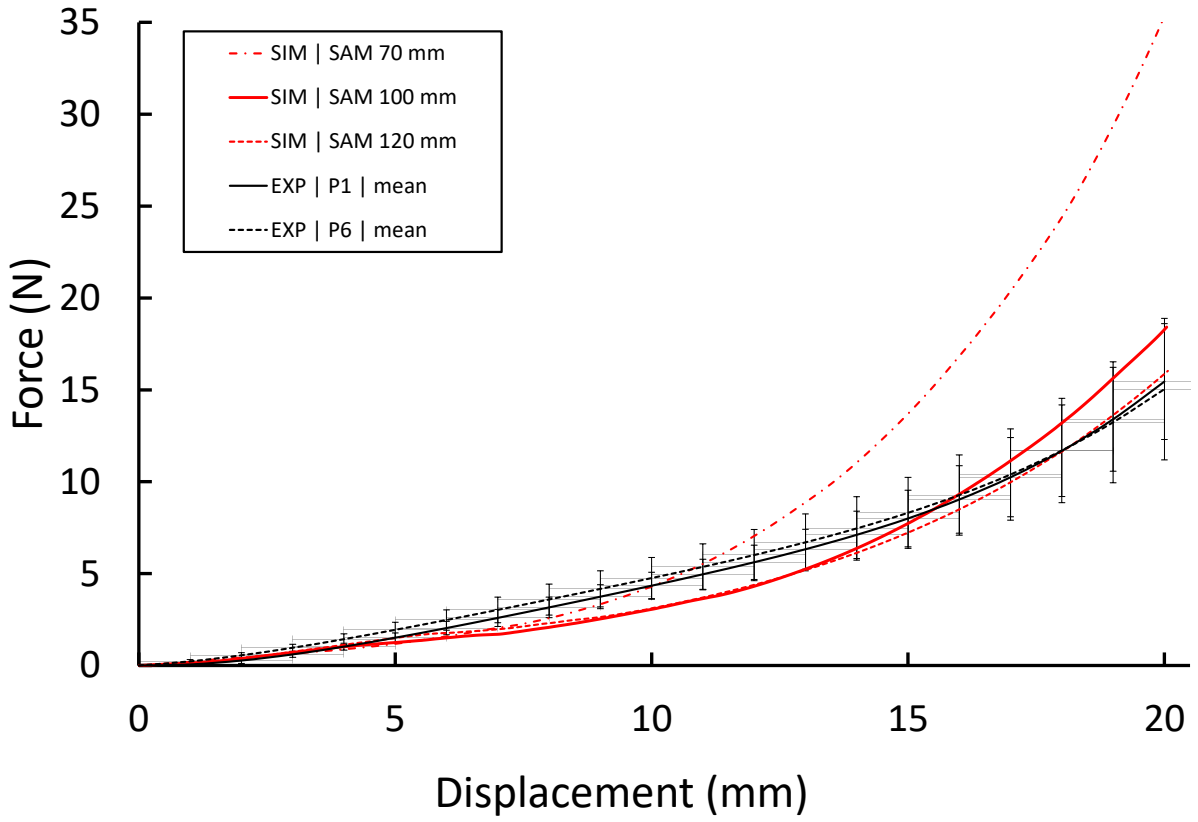

Figure 5-7. Force-displacement response for SAM with varying diameter and experimental responses of two subjects

The results obtained via the parametric study for varying diameters of SAM allow concluding that the higher amount of the soft tissue surrounding the bone will result in a softer force-displacement response to indentation. Finally, it can be concluded that provided with accurate anthropometrical dimensions, SAM can address the variability among the population.

This parametric study on the arm diameter highlights an important point linking the experiments and numerical modelling. As stated earlier, there was no anthropometric data available on the human volunteers participating in the experimental study (Benderoth, 2019; Clemen, 2017). The current parametric study showed that the force-displacement response is sensitive to the arm diameter. Therefore, lack of detailed anthropometrical dimensions may be a serious limitation in the modelling process.

5.3 The Response of the GHBMC Arm Model to Indentation

The existing GHBMC arm model was tested in the indentation scenario. The results of this test were compared with SAM. This comparison was performed to identify the differences between

the subject-specific (GHBMC) and simplified arm (SAM) geometries. To assess the contribution of the soft tissues to the indentation response, the GHBMC arm model was tested with two sets of the soft tissue properties: GHBMC tissue properties and NST properties, where the latter were developed in the course of this study.

The response of the GHBMC arm model with the GHBMC tissue properties exhibited much higher values than the average experimental data: ~90 N as opposed to ~10 N (Benderoth, 2019). The difference range between the numerical response and the experimental results ranges from 635% to 1073% (Figure 4-21). This comparison clearly showed that the existing GHBMC tissue properties within the GHBMC arm model were unable to predict the response of the upper arm to indentation. This result may be explained by the compressive mechanical properties of the GHBMC soft tissue materials. In the course of this study, it was confirmed that, on a single tissue level, the response of the GHBMC soft tissues were in general stiffer than the NST properties. This behaviour was carried over from the single element response to the force-displacement response of the GHBMC arm model.

Another possible explanation for the high response of the GHBMC arm model with the GHBMC tissue properties is the mesh size thereof. In general, the mesh density has to be adequate for the investigated problem. In the case of localized deformations, a coarse-meshed model may provide less accurate results (Ghavidel et al., 2018). The mesh density of the GHBMC arm model ranges from 4 to 12 mm. The diameter of the indenter used in the indentation scenario was 20 mm. Such coarse mesh may be unable to predict highly localized deformations caused by the indenter.

The second test performed on the GHBMC arm model involved changing the soft tissue materials from the GHBMC to NST properties. As discussed earlier, the NST properties, on a single tissue level, were more compliant than the GHBMC tissue properties. Once implemented into the GHBMC arm model, the compliant behaviour was carried over. The GHBMC arm model with the NST properties exhibited a more compliant response to the indentation. The difference in the peak force between the experimental average and the simulation response was between 113% and 240% (Figure 4-21). On the other hand, the higher overall response of the GHBMC arm model with the NST properties may be related to the coarse mesh of the GHBMC arm model.

As mentioned above, the mesh size of the GHBMC arm model (4-12 mm) is coarse in comparison to SAM (2 mm). In FE modelling, the mesh size is problem-dependent. That being the case, the

mesh size of the GHBMC arm may be suitable for predicting the kinematics of the arm model in a car crash scenario. On the other hand, however, the identical mesh size may fail to predict a localized deformation on the tissue level. Based on the above, it can be assumed that the NST properties combined with a finer mesh size of the GHBMC arm model might accurately predict the force-displacement response of the upper arm to indentation.

5.4 Mesh Convergence Study

Mesh convergence study was performed for three mesh densities: coarse, medium, and fine with the characteristic element dimension of 4, 2, and 1 mm respectively. The metric used for calculating the Grid Convergence Index was the peak force at the final indenter displacement (20 mm). Mesh convergence was achieved, therefore the 2 mm mesh was deemed appropriate for further analysis.

It is important to state that the mesh convergence study is usually problem-dependent. This statement may be explained by two scenarios. In the first case, a small indenter pushes into the soft tissue of the human arm. That being the case, the mesh has to be small enough to predict the response on a detailed level. In the second case, the lower human limb is being hit by a large pendulum with no detailed deformation. To predict the response of this scenario, a coarser mesh would suffice. Therefore it is crucial to determine the mesh size appropriate for the modelled scenario.

6 Summary

The goal of this study was to assess the mechanical properties of muscle, skin, and adipose tissue on the response of a simplified arm model to quasi-static indentation loading.

Due to the presence of the fibres and irregular connective tissue, biological tissues exhibit anisotropy. However, in the current study, this effect was not included due to limitations in the available constitutive models, but this effect was generally smaller than other effects in the tissues. The literature review performed in this study identified that the responses of muscle and adipose tissue to tensile and compressive loading are asymmetrical. To replicate the experimental response the asymmetrical behaviour was implemented in the numerical models. For both of these tissues, the asymmetry between tensile and compressive responses was observed. A comparison of these two tissues revealed an interesting characteristic. Both tissues represent very similar stiffness under compressive loading; however, the response of the muscle to tension loading was stiffer by an order of magnitude compared to the adipose tissue.

The three soft tissues investigated in this study were first assessed individually using single element simulations. The literature review together with the simulation studies guided the decisions on models and properties representing particular tissues. The skin was modelled as a shell because the thickness of the skin is lesser than the remaining dimensions. Both, skeletal muscle and adipose tissue, were represented by solid elements with hyperelastic material properties. Once the soft tissue models were analyzed on the single element level, they were incorporated into the arm model. The arm model was then indented and the force-displacement response was collected. Finally, the simulation response was compared with the experimental data.

One of the key achievements of this study was to employ uncalibrated mechanical properties of muscle, skin, and adipose tissue reported in the literature and implement them in a commercial FE software using available constitutive models. Next, these models were implemented in the arm model and assessed in the arm indentation scenario. These methods allowed achieving results comparable with the average experimental data on the upper arm indentation. Further, the simulation results revealed that muscle and adipose tissue underwent large compressive deformations which made them the main contributors to the indentation response. By contrast, skin tissue underwent smaller deformations due to the modes of loading including bending and membrane tension, thus not providing a high contribution to the overall response to indentation.

The response of the GHBMC arm model as implemented in a current HBM overpredicted the arm stiffness relative to the experimental response. However, when considering the NST properties, the GHBCM arm model response was stiffer but closer to the experimental data. It was noted that the GHBCM arm model finite element mesh incorporated larger elements compared to the recommended value for the SAM, and this coarse mesh could contribute to a higher arm stiffness. The GHBCM arm model was not designed for local indentation simulations, and therefore mesh refinement should be considered for such loading scenarios. The outcome of the GHBMC arm analysis demonstrates, that to accurately predict the experimental response, the model requires the appropriate geometry, finite element mesh resolution, and material properties representative of the modelled scenario.

The study presented in this thesis investigated the importance of the soft tissues on the indentation response of the arm under quasi-static conditions. Future research in this area could include improved geometry of the tissues in the upper arm using imaging methods such as CT scans to assess the differences between simplified and complex geometry. Although the available experimental data presenting force versus displacement was useful for assessing the model, future experimental studies should incorporate detailed imaging (CT or MRI) and measurements to provide detailed data for the assessment of computational models. It is recommended that impact scenarios should be investigated using the SAM with updated material properties including deformation rate effects. In addition, the stiffness of skeletal muscle is known to increase with muscle activation. Future work in this field should investigate the response of active muscle to indentation loading.

7 References

Abraham, A. C., Kaufman, K. R., & Haut Donahue, T. L., 2013, Phenomenological consequences of sectioning and bathing on passive muscle mechanics of the New Zealand white rabbit tibialis anterior Adam, *J Mech Behav Biomed Mater.*, *1*(17), 290–295. https://doi.org/10.1016/j.dcn.2011.01.002.The

Ahmadi, S., Sinclair, P. J., Foroughi, N., & Davis, G. M., 2007, Electromyographic activity of the biceps brachii after exercise-induced muscle damage., *Journal of Sports Science & Medicine*, *6*(4), 461–470. Retrieved from http://www.pubmedcentral.nih.gov/articlerender.fcgi?artid=3794486&tool=pmcentrez&rendertype=abstract

Alkhouli, N., Mansfield, J., Green, E., Bell, J., Knight, B., Liversedge, N., … Winlove, C. P., 2013, The mechanical properties of human adipose tissues and their relationships to the structure and composition of the extracellular matrix, *Am J Physiol Endocrinol Metab*, *305*(1), E1427–E1435. https://doi.org/10.1152/ajpendo.00111.2013

Annaidh, A. N., Karine Bruyère, Destrade, M., Gilchrist, M. D., Maurini, C., Otténio, M., & Saccomandi, G., 2012, Automated estimation of collagen fibre dispersion in the dermis and its contribution to the anisotropic behaviour of skin, *Annals of Biomedical Engineering*, *40*(8), 1666–1678. https://doi.org/10.1007/s10439-012-0542-3

Bekmez, S., Uzumcugil, A., Kalafat, E., Mermerkaya, M. U., Demirci, N., Tonuk, E., & Leblebicioglu, G., 2014, Passive Mechanical Properties of Skeletal Muscle: Analyzing the Effects of Denervation with Mathematical Modelling in a Rabbit Quadriceps Model, *Acta Medica*, 68–74.

Benderoth, G. E. K., 2019, *Private communication on the experimental data on the upper arm indentation*.

Benítez, J. M., & Montáns, F. J., 2017, The mechanical behavior of skin: Structures and models for the finite element analysis, *Computers and Structures*, *190*, 75–107. https://doi.org/10.1016/j.compstruc.2017.05.003

Bischoff, J. E., Arruda, E. M., & Grosh, K., 2000, Finite element modeling of human skin using an isotropic, nonlinear elastic constitutive model, *Journal of Biomechanics*, *33*(6), 645–652. https://doi.org/10.1016/S0021-9290(00)00018-X

Böl, M., Ehret, A. E., Leichsenring, K., Weichert, C., & Kruse, R., 2014, On the anisotropy of skeletal muscle tissue under compression, *Acta Biomaterialia*, *10*(7), 3225–3234. https://doi.org/10.1016/j.actbio.2014.03.003

Böl, M., Kruse, R., Ehret, A. E., Leichsenring, K., & Siebert, T., 2012, Compressive properties of passive skeletal muscle-The impact of precise sample geometry on parameter identification in inverse finite element analysis, *Journal of Biomechanics*, *45*(15), 2673–2679. https://doi.org/10.1016/j.jbiomech.2012.08.023

Böl, M., Leichsenring, K., Ernst, M., & Ehret, A. E., 2016, Long-term mechanical behaviour of skeletal muscle tissue in semi-confined compression experiments, *Journal of the Mechanical Behavior of Biomedical Materials*, *63*, 115–124. https://doi.org/10.1016/j.jmbbm.2016.06.012

Bosboom, E. M. H., Hesselink, M. K. C., Oomens, C. W. J., Bouten, C. V. C., Drost, M. R., & Baaijens, F. P. T., 2001, Passive transverse mechanical properties of skeletal muscle under in vivo compression, *Journal of Biomechanics*, *34*(10), 1365–1368. https://doi.org/10.1016/S0021-9290(01)00083-5

Brolin, K., Hedenstierna, S., Halldin, P., Bass, C., & Alem, N., 2008, The importance of muscle tension on the outcome of impacts with a major vertical component, *International Journal of Crashworthiness*, *13*(5), 487–498. https://doi.org/10.1080/13588260802215510

Calvo-Gallego, J. L., Domínguez, J., Gómez Cía, T., Gómez, G., & Martínez-Reina, J., 2018, Comparison of different constitutive models to characterize the viscoelastic properties of human abdominal adipose tissue. A pilot study, *Journal of the Mechanical Behavior of Biomedical Materials*, *80*(February 2018), 293–302. https://doi.org/10.1016/j.jmbbm.2018.02.013

Calvo, B., Ramírez, A., Alonso, A., Grasa, J., Soteras, F., Osta, R., & Muñoz, M. J., 2010, Passive nonlinear elastic behaviour of skeletal muscle: Experimental results and model formulation, *Journal of Biomechanics*, *43*(2), 318–325. https://doi.org/10.1016/j.jbiomech.2009.08.032

Calvo, B., Sierra, M., Grasa, J., Muñoz, M. J., & Peña, E., 2014, Determination of passive viscoelastic response of the abdominal muscle and related constitutive modeling: Stress-relaxation behavior, *Journal of the Mechanical Behavior of Biomedical Materials*, *36*, 47–58. https://doi.org/10.1016/j.jmbbm.2014.04.006

Carvalhais, V. O. do C., Ocarino, J. de M., Araújo, V. L., Souza, T. R., Silva, P. L. P., & Fonseca, S. T., 2013, Myofascial force transmission between the latissimus dorsi and gluteus maximus muscles: An in vivo experiment, *Journal of Biomechanics*, *46*(5), 1003–1007. https://doi.org/10.1016/j.jbiomech.2012.11.044

Chawla, A., Mukherjee, S., & Karthikeyan, B., 2009, Characterization of human passive muscles for impact loads using genetic algorithm and inverse finite element methods, *Biomechanics and Modeling in Mechanobiology*, *8*(1), 67–76. https://doi.org/10.1007/s10237-008-0121-6

Chen, K., & Weiland, J. D., 2011, Mechanical Properties of Orbital Fat and Its Encapsulating Connective Tissue, *Journal of Biomechanical Engineering*, *133*(6), 064505. https://doi.org/10.1115/1.4004289

Clemen, C. B., Benderoth, G. E. K., Schmidt, A., Hübner, F., Vogl, T. J., & Silber, G., 2017, Human skeletal muscle behavior in vivo: Finite element implementation, experiment, and passive mechanical characterization, *Journal of the Mechanical Behavior of Biomedical Materials*, *65*(April 2016), 679–687. https://doi.org/10.1016/j.jmbbm.2016.09.030

Comley, K., & Fleck, N., 2009, The mechanical response of porcine adipose tissue, *ASME Journal*

of Biomechanical Engineering, (June), 1–30.

Comley, K., & Fleck, N., 2012, The compressive response of porcine adipose tissue from low to high strain rate, *International Journal of Impact Engineering*, *46*, 1–10. https://doi.org/10.1016/j.ijimpeng.2011.12.009

Comley, K., & Fleck, N. A., 2010a, A micromechanical model for the Young's modulus of adipose tissue, *International Journal of Solids and Structures*, *47*(21), 2982–2990. https://doi.org/10.1016/j.ijsolstr.2010.07.001

Comley, K., & Fleck, N. A., 2010b, The toughness of adipose tissue: measurements and physical basis, *Journal of Biomechanics*, *43*(9), 1823–1826. https://doi.org/10.1016/j.jbiomech.2010.02.029

Danelson, K. a, Geer, C. P., Stitzel, J. D., Slice, D. E., & Takhounts, E. G., 2008, Age and gender based biomechanical shape and size analysis of the pediatric brain., *Stapp Car Crash Journal*, *52*(November), 59–81.

Davis, J., Kaufman, K. R., & Lieber, R. L., 2003, Correlation between active and passive isometric force and intramuscular pressure in the isolated rabbit tibialis anterior muscle, *Journal of Biomechanics*, *36*(4), 505–512. https://doi.org/10.1016/S0021-9290(02)00430-X

Dhaliwal, T. S., Beillas, P., Chou, C. C., Prasad, P., Yang, K. H., & King, A. I., 2002, Structural Response of Lower Leg Muscles in Compression: A Low Impact Energy Study Employing Volunteers, Cadavers and the Hybrid III., *Stapp Car Crash Journal*, *46*(November), 229–243.

Dibb, A. T., Cox, C. A., Nightingale, R. W., Luck, J. F., Cutcliffe, H. C., Myers, B. S., … Bass, C. R., 2013, Importance of Muscle Activations for Biofidelic Pediatric Neck Response in Computational Models, *Traffic Injury Prevention*, *14*(SUPPL1). https://doi.org/10.1080/15389588.2013.806795

Dordević, S., Stančin, S., Meglič, A., Milutinović, V., & Tomažič, S., 2011, MC sensor-a novel method for measurement of muscle tension, *Sensors*, *11*(10), 9411–9425. https://doi.org/10.3390/s111009411

Dr.Gayatri, & H. R. Sharada, 2014, Asymmetry in Length, Weight and Circumference of Upper Limb Bones in Telangana State, *IOSR Journal of Dental and Medical Sciences (IOSR-JDMS)*, *13*(10), 24–26. Retrieved from http://www.iosrjournals.org/iosr-jdms/papers/Vol13-issue10/Version-4/E0131042426.pdf

Du Bois, P., 2003, A simplified approach to the simulation of rubber-like materials under dynamic loading, *4th European LS-DYNA Users Conference*, 31–46. Retrieved from http://www.dynalook.com/european-conf-2003/a-simplified-approach-to-the-simulation-of-rubber.pdf

Eby, S. F., Cloud, B. A., Brandenburg, J. E., Giambini, H., Song, P., Chen, S., … An, K. N., 2015, Shear wave elastography of passive skeletal muscle stiffness: Influences of sex and age throughout adulthood, *Clinical Biomechanics*, *30*(1), 22–27. https://doi.org/10.1016/j.clinbiomech.2014.11.011

Eby, S. F., Song, P., Chen, S., Chen, Q., Greenleaf, J. F., & An, K. N., 2013, Validation of shear wave elastography in skeletal muscle, *Journal of Biomechanics*, *46*(14), 2381–2387. https://doi.org/10.1016/j.jbiomech.2013.07.033

ElMaraghy, A., Devereaux, M., & Tsoi, K., 2008, The biceps crease interval for diagnosing complete distal biceps tendon ruptures, *Clinical Orthopaedics and Related Research*, *466*(9), 2255–2262. https://doi.org/10.1007/s11999-008-0334-0

Engelbrektsson, K., 2011, Evaluation of material models in LS-DYNA for impact simulation of white adipose tissue.

Evans, N. C., 2018, Private Communication on the Passive Muscle Model.

Farvid, M. S., Ng, T. W. K., Chan, D. C., Barrett, P. H. R., & Watts, G. F., 2006, Association of adiponectin and resistin with adipose tissue compartments, insulin resistance and dyslipidaemia, *Diabetes, Obesity & Metabolism*, *8*(2), 136–145. https://doi.org/10.1111/j.1463

Faulkner, J. A., Larkin, L. M., Claflin, D. R., & Brooks, S. V, 2007, AGE-RELATED CHANGES IN THE STRUCTURE AND FUNCTION OF SKELETAL MUSCLES, *Clinical and Experimental Pharmacology and Physiology*, *34*, 1091–1096. https://doi.org/10.1016/0022-510X(88)90132-3

Flynn, C., & Mccormack, B. A. O., 2008, Finite element modelling of forearm skin wrinkling, *Skin Research and Technology*, *14*(3), 261–269. https://doi.org/10.1111/j.1600-0846.2008.00289.x

Flynn, C., Stavness, I., Lloyd, J., & Fels, S., 2015, A finite element model of the face including an orthotropic skin model under in vivo tension, *Computer Methods in Biomechanics and Biomedical Engineering*, *18*(6), 571–582. https://doi.org/10.1080/10255842.2013.820720

Frances, C., Branchet, M. C., Boisnic, S., Lesty, C. L., & Robert, L., 1990, Elastic fibers in normal human skin. variations with age: a morphometric analysis, *Archives of Gerontology and Geriatrics*, *10*(1), 57–67. https://doi.org/10.1016/0167-4943(90)90044-7

Gahagnon, S., Mofid, Y., Josse, G., & Ossant, F., 2012, Skin anisotropy in vivo and initial natural stress effect: A quantitative study using high-frequency static elastography, *Journal of Biomechanics*, *45*(16), 2860–2865. https://doi.org/10.1016/j.jbiomech.2012.08.032

Gąsior-Głogowska, M., Komorowska, M., Hanuza, J., Maczka, M., Zajac, A., Ptak, M., … Szotek, S., 2013, FT-Raman spectroscopic study of human skin subjected to uniaxial stress, *Journal of the Mechanical Behavior of Biomedical Materials*, *18*, 240–252. https://doi.org/10.1016/j.jmbbm.2012.11.023

Gayzik, F. S., Moreno, D. P., Geer, C. P., Wuertzer, S. D., Martin, R. S., & Stitzel, J. D., 2011, Development of a full body CAD dataset for computational modeling: A multi-modality approach, *Annals of Biomedical Engineering*, *39*(10), 2568–2583. https://doi.org/10.1007/s10439-011-0359-5

Gepner, B., Joodaki, H., Sun, Z., Jayathirtha, M., Kim, T., Forman, J., & Kerrigan, J., 2018, Performance of the Obese GHBMC Models in the Sled and Belt Pull Test Conditions, *IRCOBI Conference*, 355–368. Retrieved from http://www.ircobi.org/wordpress/downloads/irc18/pdf-files/60.pdf

Ghavidel, A., Mousavi, S. R., & Rashki, M., 2018, The effect of FEM mesh density on the failure probability analysis of structures, *KSCE Journal of Civil Engineering*, *22*(7), 2371–2383. https://doi.org/10.1007/s12205-017-1437-5

Gierczycka, D., & Cronin, D., 2018, Influence of the chest compression measurement method on assessment of restraint performance in side-impact crash scenarios, *Journal of Biomechanics*, *75*, 53–57. https://doi.org/10.1016/j.jbiomech.2018.04.044

Goodpaster, B. H., Thaete, F. L., & Kelley, D. E., 2000, Composition of Skeletal Muscle Evaluated with, *Annals of the New York Academy of Sciences Volume 904, IN VIVO BODY COMPOSITION STUDIES Pages 18–24, May 2000*, 18–24. https://doi.org/doi: 10.1111/j.1749-6632.2000.tb06416.x

Gottsauner-Wolf, F., Grabowski, J. J., Chao, E. Y. S., & An, K., 1995, Effects of Freeze/Thaw Conditioning on the Tensile Properties and Failure Mode of Bone-Muscle-Bone Units: A Biomechanical and Histological Study in Dogs, *13*(4), 90–95.

Gras, L. L., Mitton, D., Viot, P., & Laporte, S., 2013, Viscoelastic properties of the human sternocleidomastoideus muscle of aged women in relaxation, *Journal of the Mechanical Behavior of Biomedical Materials*, *27*, 77–83. https://doi.org/10.1016/j.jmbbm.2013.06.010

Grasa, J., Ramírez, A., Osta, R., Muñoz, M. J., Soteras, F., & Calvo, B., 2011, A 3D active-passive numerical skeletal muscle model incorporating initial tissue strains. Validation with experimental results on rat tibialis anterior muscle, *Biomechanics and Modeling in Mechanobiology*, *10*(5), 779–787. https://doi.org/10.1007/s10237-010-0273-z

Grasa, J., Sierra, M., Lauzeral, N., Muñoz, M. J., Miana-Mena, F. J., & Calvo, B., 2016, Active behavior of abdominal wall muscles: Experimental results and numerical model formulation, *Journal of the Mechanical Behavior of Biomedical Materials*, *61*, 444–454. https://doi.org/10.1016/j.jmbbm.2016.04.013

Hallquist, J. O., 2015, LS-DYNA Keyword User's Manual, Volume II, Material Models.

Hansen, J. T., 2010, *Netter's Clinical Anatomy*. Saunders Elsevier.

Hedenstierna, S., Halldin, P., & Brolin, K., 2008, Evaluation of a combination of continuum and truss finite elements in a model of passive and active muscle tissue, *Computer Methods in Biomechanics and Biomedical Engineering*, *11*(6), 627–639. https://doi.org/10.1080/17474230802312516

Hernández-Gascón, B., Grasa, J., Calvo, B., & Rodríguez, J. F., 2013, A 3D electro-mechanical continuum model for simulating skeletal muscle contraction, *Journal of Theoretical Biology*, *335*, 108–118. https://doi.org/10.1016/j.jtbi.2013.06.029

Iivarinen, J. T., Korhonen, R. K., Julkunen, P., & Jurvelin, J. S., 2011, Experimental and computational analysis of soft tissue stiffness in forearm using a manual indentation device, *Medical Engineering and Physics*, *33*(10), 1245–1253. https://doi.org/10.1016/j.medengphy.2011.05.015

Iwamoto, M., Nakahira, Y., & Kimpara, H., 2015, Development and Validation of the Total HUman Model for Safety (THUMS) Toward Further Understanding of Occupant Injury Mechanisms in Precrash and During Crash, *Traffic Injury Prevention*, *16*, 36–48. https://doi.org/10.1080/15389588.2015.1015000

Iwamoto, M., Nakahira, Y., Kimpara, H., Sugiyama, T., & Min, K., 2012, Development of a Human Body Finite Element Model with Multiple Muscles and their Controller for Estimating Occupant Motions and Impact Responses in Frontal Crash Situations, *Stapp Car Crash Journal*, *56*(October), 231–268.

Jacquet, E., Chambert, J., Pauchot, J., & Sandoz, P., 2017, Intra- and inter-individual variability in the mechanical properties of the human skin from in vivo measurements on 20 volunteers, *Skin Research and Technology*, *23*(4), 491–499. https://doi.org/10.1111/srt.12361

Jehle, D., Gemme, S., & Jehle, C., 2012, Influence of obesity on mortality of drivers in severe motor vehicle crashes, *American Journal of Emergency Medicine*, *30*(1), 191–195. https://doi.org/10.1016/j.ajem.2010.10.017

Joodaki, H., & Panzer, M. B., 2018, Skin mechanical properties and modeling: A review, *Proceedings of the Institution of Mechanical Engineers, Part H: Journal of Engineering in Medicine*, *232*(4), 323–343. https://doi.org/10.1177/0954411918759801

Joseph, B., Hadeed, S., Haider, A. A., Ditillo, M., Joseph, A., Pandit, V., … Rhee, P., 2017, Obesity and trauma mortality: Sizing up the risks in motor vehicle crashes, *Obesity Research and Clinical Practice*, *11*(1), 72–78. https://doi.org/10.1016/j.orcp.2016.03.003

Karthikeyan, B., 2009, *IMPACT RESPONSE OF MUSCLES*. https://doi.org/10.13140/RG.2.1.1560.3282

Khor, F., 2018, Computational Modeling of Hard Tissue Response and Fracture in the Lower Cervical Spine under Compression Including Age Effects.

Kleinbach, C., Martynenko, O., Promies, J., Haeufle, D. F. B., Fehr, J., & Schmitt, S., 2017, Implementation and validation of the extended Hill-type muscle model with robust routing capabilities in LS-DYNA for active human body models, *BioMedical Engineering Online*, *16*(1), 1–28. https://doi.org/10.1186/s12938-017-0399-7

Krašna, S., Đorđević, S., Hribernik, M., & Trajkovski, A., 2017, A novel approach to measuring muscle mechanics in vehicle collision conditions, *Sensors (Switzerland)*, *17*(6), 1–17. https://doi.org/10.3390/s17061389

Lamers, E., van Kempen, T. H. S., Baaijens, F. P. T., Peters, G. W. M., & Oomens, C. W. J., 2013, Large amplitude oscillatory shear properties of human skin, *Journal of the Mechanical Behavior of Biomedical Materials*, *28*, 462–470.

https://doi.org/10.1016/j.jmbbm.2013.01.024

Lanir, Y., & Fung, Y. C., 1974, Two-Dimensional Mechanical Properties of Rabbit Skin - II Experimental Results, *Journal of Biomechanics*, *7*, 171–182.

Lapeer, R. J., Gasson, P. D., & Karri, V., 2010, Simulating plastic surgery: From human skin tensile tests, through hyperelastic finite element models to real-time haptics, *Progress in Biophysics and Molecular Biology*, *103*(2–3), 208–216. https://doi.org/10.1016/j.pbiomolbio.2010.09.013

Lewandowski, B., Brooker, J., Weaver, A., & Myers, J., 2012, Development of a Traumatic Abdominal Injury Module for Estimation of Injury Probability During an International Space Station Mission, 1–14. Retrieved from https://ntrs.nasa.gov/search.jsp?R=20150010154

Limbert, G., & Middleton, J., 2004, A transversely isotropic viscohyperelastic material Application to the modeling of biological soft connective tissues, *International Journal of Solids and Structures*, *41*(15), 4237–4260. https://doi.org/10.1016/j.ijsolstr.2004.02.057

Loerakker, S., Solis, L. R., Bader, D. L., Baaijens, F. P. T., Mushahwar, V. K., & Oomens, C. W. J., 2013, How does muscle stiffness affect the internal deformations within the soft tissue layers of the buttocks under constant loading?, *Computer Methods in Biomechanics and Biomedical Engineering*, *16*(5), 520–529. https://doi.org/10.1080/10255842.2011.627682

Loerakker, S., Stekelenburg, A., Strijkers, G. J., Rijpkema, J. J. M., Baaijens, F. P. T., Bader, D. L., … Oomens, C. W. J., 2010, Temporal Effects of Mechanical Loading on Deformation-Induced Damage in Skeletal Muscle Tissue, *Annals of Biomedical Engineering*, *38*(8), 2577–2587. https://doi.org/10.1007/s10439-010-0002-x

Maganaris, C. N., 2002, Tensile properties of in vivo human tendinous tissue, *Journal of Biomechanics*, *35*(8), 1019–1027. https://doi.org/10.1016/S0021-9290(02)00047-7

Marsh, R. L., 2016, Speed of sound in muscle for use in sonomicrometry, *Journal of Biomechanics*, *49*(16), 4138–4141. https://doi.org/10.1016/j.jbiomech.2016.10.024

Martin, A. D., Daniel, M. Z., Drinkwater, D. T., & Clarys, J. ., 1994, Adipose tissue density, estimated adipose lipid fraction and whole body adiposity in male cadavers, *International Journal of Obesity*, *18*(2), 79–83.

Mathur, A. B., Collinsworth, A. M., Reichert, W. M., Kraus, W. E., & Truskey, G. A., 2001, Endothelial, cardiac muscle and skeletal muscle exhibit different viscous and elastic properties as determined by atomic force microscopy, *Journal of Biomechanics*, *34*(12), 1545–1553. https://doi.org/10.1016/S0021-9290(01)00149-X

Matkowski, B., Martin, A., & Lepers, R., 2011, Comparison of maximal unilateral versus bilateral voluntary contraction force, *European Journal of Applied Physiology*, *111*(8), 1571–1578. https://doi.org/10.1007/s00421-010-1775-1

Miller-Young, J. E., Duncan, N. A., & Baroud, G., 2002, Material properties of the human calcaneal fat pad in compression: Experiment and theory, *Journal of Biomechanics*, *35*(12), 1523–

1531. https://doi.org/10.1016/S0021-9290(02)00090-8

Moerman, K. M., Simms, C. K., & Nagel, T., 2016, Control of tension-compression asymmetry in Ogden hyperelasticity with application to soft tissue modelling, *Journal of the Mechanical Behavior of Biomedical Materials*, *56*, 218–228. https://doi.org/10.1016/j.jmbbm.2015.11.027

Mohammadkhah, M., Murphy, P., & Simms, C. K., 2016, The in vitro passive elastic response of chicken pectoralis muscle to applied tensile and compressive deformation, *Journal of the Mechanical Behavior of Biomedical Materials*, *62*, 468–480. https://doi.org/10.1016/j.jmbbm.2016.05.021

Morrison, B., Cater, H. L., Wang, C. C.-B., Thomas, F. C., Hung, C. T., Ateshian, G. a, & Sundstrom, L. E., 2003, A tissue level tolerance criterion for living brain developed with an in vitro model of traumatic mechanical loading., *Stapp Car Crash Journal*, *47*(October), 93–105. https://doi.org/2003-22-0006 [pii]

Morrow, D. A., Haut Donahue, T. L., Odegard, G. M., & Kaufman, K. R., 2010, Transversely isotropic tensile material properties of skeletal muscle tissue, *Journal of the Mechanical Behavior of Biomedical Materials*, *3*(1), 124–129. https://doi.org/10.1016/j.jmbbm.2009.03.004

Mortensen, J., Trkov, M., & Merryweather, A., 2018, Exploring novel objective functions for simulating muscle coactivation in the neck, *Journal of Biomechanics*, *71*, 127–134. https://doi.org/10.1016/j.jbiomech.2018.01.030

Muggenthaler, H., Praxl, N., Adamec, J., Merten, K. Von, Schönpflug, M., Graw, M., & Schneider, K., 2006, The Effects of Muscle Activity on Human Kinematics and Muscle Response Characteristics – Volunteer Tests for the Validation of Active Human Models and Engineering Conference, (724), 776–790.

Muggenthaler, H., von Merten, K., Peldschus, S., Holley, S., Adamec, J., Praxl, N., & Graw, M., 2008, Experimental tests for the validation of active numerical human models, *Forensic Science International*, *177*(2–3), 184–191. https://doi.org/10.1016/j.forsciint.2007.12.005

Murakami, D., Kobayashi, S., Torigaki, T., & Kent, R., 2006, Finite element analysis of hard and soft tissue contributions to thoracic response: sensitivity analysis of fluctuations in boundary conditions., *Stapp Car Crash Journal*, *50*(November), 169–189. https://doi.org/2006-22-0008 [pii]

Murdoch, A. H., Mathias, K. J., & Smith, F. W., 2002, Measurement of the bony anatomy of the humerus using magnetic resonance imaging, *Proceedings of the Institution of Mechanical Engineers, Part H: Journal of Engineering in Medicine*, *216*(1), 31–35. https://doi.org/10.1243/0954411021536252

Myers, B. S., Ee, C. a Van, Camacho, D. L. a, Woolley, C. T., Best, T. M., Van Ee, C., & Woolley, T., 1995, On the structural and material properties of mammalian skeletal muscle, *Control*. https://doi.org/10.4271/952723

Myers, B. S., Woolley, C. T., Slotter, T. L., Garrett, W. E., & Best, T. M., 1998, The Influence of Strain Rate on the Passive and Stimulated Engineering Stress–Large Strain Behavior of the Rabbit Tibialis Anterior Muscle, *Journal of Biomechanical Engineering*, *120*(1), 126. https://doi.org/10.1115/1.2834292

Nagle, A. S., Barker, M. A., Kleeman, S. D., Haridas, B., & Douglas Mast, T., 2014, Passive biomechanical properties of human cadaveric levator ani muscle at low strains, *Journal of Biomechanics*, *47*(2), 583–586. https://doi.org/10.1016/j.jbiomech.2013.11.033

Naseri, H., Johansson, H., & Brolin, K., 2017, A nonlinear viscoelastic model for adipose tissue representing tissue response at a wide range of strain rates and high strain levels, *Journal of Biomechanical Engineering*, *140*(April 2018), 1–8. https://doi.org/10.1115/1.4038200

Ní Annaidh, A., Bruyère, K., Destrade, M., Gilchrist, M. D., & Otténio, M., 2012, Characterization of the anisotropic mechanical properties of excised human skin, *Journal of the Mechanical Behavior of Biomedical Materials*, *5*(1), 139–148. https://doi.org/10.1016/j.jmbbm.2011.08.016

Nie, X., Cheng, J.-I., Chen, W. W., & Weerasooriya, T., 2011, Dynamic Tensile Response of Porcine Muscle, *Journal of Applied Mechanics*, *78*(2), 021009. https://doi.org/10.1115/1.4002580

Nolan, D. R., Gower, A. L., Destrade, M., Ogden, R. W., & McGarry, J. P., 2014, A robust anisotropic hyperelastic formulation for the modelling of soft tissue, *Journal of the Mechanical Behavior of Biomedical Materials*, *39*, 48–60. https://doi.org/10.1016/j.jmbbm.2014.06.016

Nordez, A., & Hug, F., 2010, Muscle shear elastic modulus measured using supersonic shear imaging is highly related to muscle activity level, *Journal of Applied Physiology*, *108*(5), 1389–1394. https://doi.org/10.1152/japplphysiol.01323.2009

Ogden, R. W., 1984, *Non-linear Elastic Deformations*. Ellis Horwood Limited.

Ogden, R. W., Saccomandi, G., & Sgura, I., 2004, Fitting hyperelastic models to experimental data, *Computational Mechanics*, *34*(6), 484–502. https://doi.org/10.1007/s00466-004-0593-y

Ólafsdóttir, J. M., Brolin, K., Blouin, J. S., & Siegmund, G. P., 2015, Dynamic spatial tuning of cervical muscle reflexes to multidirectional seated perturbations, *Spine*, *40*(4), E211–E219. https://doi.org/10.1097/BRS.0000000000000721

Oomens, C. W. J., Maenhout, M., van Oijen, C. H., Drost, M. R., & Baaijens, F. P., 2003, Finite element modelling of contracting skeletal muscle, *Philosophical Transactions of the Royal Society B: Biological Sciences*, *358*(1437), 1453–1460. https://doi.org/10.1098/rstb.2003.1345

Östh, J., 2014, *Muscle Responses of Car Occupants. Numerical Modeling and Volunteer Experiments under Pre - Crash Braking Conditions*. Chalmers University of Technology.

Östh, J., Brolin, K., Ólafsdóttir, J. M., Davidsson, J., Pipkorn, B., Jakobsson, L., … National Highway Traffic Safety, A., 2015, Muscle Activation Strategies in Human Body Models for the Development of Integrated Safety, 15p. https://doi.org/10.1016/j.biombioe.2006.01.005

Östh, J., Mendoza-Vazquez, M., Linder, A., Svensson, M. Y., & Brolin, K., 2017, The VIVA OpenHBM Finite Element 50th Percentile Female Occupant Model: Whole Body Model Development and Kinematic Validation, *IRCOBI Conference*, 677–678.

Ottenio, M., Tran, D., Ní Annaidh, A., Gilchrist, M. D., & Bruyère, K., 2015, Strain rate and anisotropy effects on the tensile failure characteristics of human skin, *Journal of the Mechanical Behavior of Biomedical Materials*, *41*, 241–250. https://doi.org/10.1016/j.jmbbm.2014.10.006

Pamuk, U., Karakuzu, A., Ozturk, C., Acar, B., & Yucesoy, C. A., 2016, Combined magnetic resonance and diffusion tensor imaging analyses provide a powerful tool for in vivo assessment of deformation along human muscle fibers, *Journal of the Mechanical Behavior of Biomedical Materials*, *63*, 207–219. https://doi.org/10.1016/j.jmbbm.2016.06.031

Panzer, M. B., Fice, J. B., & Cronin, D. S., 2011, Cervical spine response in frontal crash, *Medical Engineering and Physics*, *33*(9), 1147–1159. https://doi.org/10.1016/j.medengphy.2011.05.004

Pereira, J. M., Mansour, J. M., & Davis, B. R., 1991, Dynamic Measurement of the Viscoelastic Properties of Skin, *Journal of Biomechanics*, *24*(2), 157–162.

Potts, R. O., Chrisman, D. A., & Buras, E. M., 1983, The dynamic mechanical properties of human skin in vivo, *Journal of Biomechanics*, *16*(6), 365–372. https://doi.org/10.1016/0021-9290(83)90070-2

Ralis, Z. A., 1989, Freezing of Orthopaedic Specimens Before Mechanical Testing, *Journal of Bone and Joint Surgery*, *71-B*(1), 55–57. https://doi.org/10.1302/0301-620X.71B1.2915006

Rehorn, M. R., Schroer, A. K., & Blemker, S. S., 2014, The passive properties of muscle fibers are velocity dependent, *Journal of Biomechanics*, *47*(3), 687–693. https://doi.org/10.1016/j.jbiomech.2013.11.044

Reihsner, R., Balogh, B., & Menzel, E. J., 1995, Two-dimensional elastic properties of human skin in terms of an incremental model at the in vivo configuration, *Medical Engineering and Physics*, *17*(4), 304–313. https://doi.org/10.1016/1350-4533(95)90856-7

Richmond, F. J., Singh, K., & Corneil, B. D., 2001, Neck muscles in the rhesus monkey. I. Muscle morphometry and histochemistry., *Journal of Neurophysiology*, *86*(4), 1717–1728. https://doi.org/10.1152/jn.2001.86.4.1717

Ridge, M. D., & Wright, V., 1966, The directional effects of skin. A bio-engineering study of skin with particular reference to Langer's lines., *The Journal of Investigative Dermatology*, *46*(4), 341–346. https://doi.org/10.1038/jid.1966.54

Roache, P. J., 1994, Perspective: A Method for Uniform Reporting of Grid Refinement Studies, *Journal of Fluids Engineering*, *116*(3), 405. https://doi.org/10.1115/1.2910291

Roache, P. J., 1998, *Verification and Validation in Computational Science and Engineering*. Albuquerque NM: Hermosa Publishers.

Robbins, D. H., 1983, Anthropometric specifications for mid-sized male dummy, (2), 134.

Ruan, J. S., El-Jawahri, R., Barbat, S., Rouhana, S. W., & Prasad, P., 2008, Impact response and biomechanical analysis of the knee-thigh-hip complex in frontal impacts with a full human body finite element model., *Stapp Car Crash Journal*, *52*(November), 505–526.

Saraf, H., Ramesh, K. T., Lennon, A. M., Merkle, A. C., & Roberts, J. C., 2007, Mechanical properties of soft human tissues under dynamic loading, *Journal of Biomechanics*, *40*(9), 1960–1967. https://doi.org/10.1016/j.jbiomech.2006.09.021

Schmitt, K.-U., Niederer, P. F., Cronin, D. S., Morrison III, B., Muser, M. H., & Walz, F., 2019, *Trauma Biomechanics*.

Schwartz, D., Guleyupoglu, B., Koya, B., Stitzel, J. D., & Gayzik, F. S., 2015, Development of a Computationally Efficient Full Human Body Finite Element Model, *Traffic Injury Prevention*, *16*(March 2017), 49–56. https://doi.org/10.1080/15389588.2015.1021418

Sengeh, D. M., Moerman, K. M., Petron, A., & Herr, H., 2016, Multi-material 3-D viscoelastic model of a transtibial residuum from in-vivo indentation and MRI data, *Journal of the Mechanical Behavior of Biomedical Materials*, *59*, 379–392. https://doi.org/10.1016/j.jmbbm.2016.02.020

Shah, C., 2002, Mesh Discretization Error and Criteria for Accuracy of Finite Element Solutions, *International ANSYS Conference* , 12.

Shapiro, M., Tovar, N., Yoo, D., Sobieraj, M., Gupta, N., Branski, R. C., & Coelho, P. G., 2014, Strain rate effects on the mechanical properties and fracture mode of skeletal muscle, *Materials Science and Engineering C*, *39*(1), 100–104. https://doi.org/10.1016/j.msec.2014.02.032

Sharafi, B., & Blemker, S. S., 2011, A mathematical model of force transmission from intrafascicularly terminating muscle fibers, *Journal of Biomechanics*, *44*(11), 2031–2039. https://doi.org/10.1016/j.jbiomech.2011.04.038

Shergold, O. A., Fleck, N. A., & Radford, D., 2006, The uniaxial stress versus strain response of pig skin and silicone rubber at low and high strain rates, *International Journal of Impact Engineering*, *32*(9), 1384–1402. https://doi.org/10.1016/j.ijimpeng.2004.11.010

Sherman, V. R., Tang, Y., Zhao, S., Yang, W., & Meyers, M. A., 2017, Structural characterization and viscoelastic constitutive modeling of skin, *Acta Biomaterialia*, *53*, 460–469. https://doi.org/10.1016/j.actbio.2017.02.011

Shuster, S., Black, M. M., & McVittie, E., 1975, The influence of age and sex on skin thickness, skin collagen and density, *British Journal of Dermatology*, *93*(6), 639–643. https://doi.org/10.1111/j.1365-2133.1975.tb05113.x

Siegmund, G. P., & Blouin, J. S., 2009, Head and neck control varies with perturbation acceleration but not jerk: Implications for whiplash injuries, *Journal of Physiology*, *587*(8), 1829–1842. https://doi.org/10.1113/jphysiol.2009.169151

Siegmund, G. P., Sanderson, D. J., Myers, B. S., & Inglis, J. T., 2003, Awareness affects the response

of human subjects exposed to a single whiplash-like perturbation, *Spine*, *28*(7), 671–679. https://doi.org/10.1097/00007632-200304010-00010

Silva, M. P. T., & Ambrósio, J. A. C., 1999, Pedestrian impact and run over using a multibody simulation tool, *International Journal of Crashworthiness*, *4*(3), 261–272. https://doi.org/10.1533/cras.1999.0104

Simms, C., Kilroy, H., Blackburn, G., & Takaza, M., 2017, The influence of physical dimension on apparent stress-strain behaviour of in vitro passive skeletal muscle samples, *Journal of Strain Analysis for Engineering Design*, *52*(1), 3–11. https://doi.org/10.1177/0309324716668673

Singh, A., Nagar, M., & Kumar, A., 2014, RESEARCH AND REVIEWS : JOURNAL OF MEDICAL AND An Anthropometric Study of the Humerus in Adults ., *3*(3), 77–82.

Soetens, J. F. J., van Vijven, M., Bader, D. L., Peters, G. W. M., & Oomens, C. W. J., 2018, A model of human skin under large amplitude oscillatory shear, *Journal of the Mechanical Behavior of Biomedical Materials*, *86*(July), 423–432. https://doi.org/10.1016/j.jmbbm.2018.07.008

Sommer, G., Eder, M., Kovacs, L., Pathak, H., Bonitz, L., Mueller, C., … Holzapfel, G. A., 2013, Multiaxial mechanical properties and constitutive modeling of human adipose tissue: A basis for preoperative simulations in plastic and reconstructive surgery, *Acta Biomaterialia*, *9*(11), 9036–9048. https://doi.org/10.1016/j.actbio.2013.06.011

Souza, J. de, & Gottfried, C., 2013, Muscle injury: Review of experimental models, *Journal of Electromyography and Kinesiology*, *23*(6), 1253–1260. https://doi.org/10.1016/j.jelekin.2013.07.009

Standring, S., 2008, *Gray's Anatomy - The Anatomical Basis of Clinical Practice*, (S. Standring, Ed.) (40th ed.). London, UK: Churchill Livingstone Elsevier.

Stitzel, J. D., Gayzik, F. S., Hoth, J. J., Mercier, J., Gage, H. D., Morton, K. a, … Payne, R. M., 2005, Development of a finite element-based injury metric for pulmonary contusion part I: model development and validation., *Stapp Car Crash Journal*, *49*(November), 271–289. https://doi.org/2005-22-0013 [pii]

Stokes, K. L., Forbes, S. L., & Tibbett, M., 2013, Human Versus Animal: Contrasting Decomposition Dynamics of Mammalian Analogues in Experimental Taphonomy, *Journal of Forensic Sciences*, *58*(3), 583–591. https://doi.org/10.1111/1556-4029.12115

Takaza, M., Moerman, K. M., & Simms, C. K., 2013, Passive skeletal muscle response to impact loading: Experimental testing and inverse modelling, *Journal of the Mechanical Behavior of Biomedical Materials*, *27*, 214–225. https://doi.org/10.1016/j.jmbbm.2013.04.016

Then, C., Vogl, T. J., & Silber, G., 2012, Method for characterizing viscoelasticity of human gluteal tissue, *Journal of Biomechanics*, *45*(7), 1252–1258. https://doi.org/10.1016/j.jbiomech.2012.01.037

Tirrell, T. F., Cook, M. S., Carr, J. A., Lin, E., Ward, S. R., & Lieber, R. L., 2012, Human skeletal muscle biochemical diversity, *Journal of Experimental Biology*, *215*(15), 2551–2559.

https://doi.org/10.1242/jeb.069385

Urbanchek, M. G., Picken, E. B., Kalliainen, L. K., & Kuzon, W. M., 2001, Specific force deficit in skeletal muscles of old rats is partially explained by the existence of denervated muscle fibers, *Journals of Gerontology - Series A Biological Sciences and Medical Sciences*, *56*(5), B191–B197. https://doi.org/10.1093/gerona/56.5.B191

Van Loocke, M., Lyons, C. G., & Simms, C. K., 2006, A validated model of passive muscle in compression, *Journal of Biomechanics*, *39*(16), 2999–3009. https://doi.org/10.1016/j.jbiomech.2005.10.016

Van Loocke, M., Lyons, C. G., & Simms, C. K., 2008, Viscoelastic properties of passive skeletal muscle in compression: Stress-relaxation behaviour and constitutive modelling, *Journal of Biomechanics*, *41*(7), 1555–1566. https://doi.org/10.1016/j.jbiomech.2008.02.007

Van Loocke, M., Simms, C. K., & Lyons, C. G., 2009, Viscoelastic properties of passive skeletal muscle in compression-Cyclic behaviour, *Journal of Biomechanics*, *42*(8), 1038–1048. https://doi.org/10.1016/j.jbiomech.2009.02.022

Vannah, W. M., & Childress, D. S., 1996, Indentor tests and finite element modeling of bulk muscular tissue in vivo., *Journal of Rehabilitation Research and Development*, *33*(3), 239–252.

Vezin, P., Bruyere-Garnier, K., Bermond, F., & Verriest, J. P., 2002, Comparison of Hybrid III , Thor-α and PMHS Response in Frontal Sled Tests 46th Stapp Car Crash Conference, *Stapp Car Crash Journal*, *46*(November), 1–26.

Vizniak, N. A., 2010, *Muscle Manual*. Professional Health Systems Inc.

Wang, J., Thornton, J. C., Kolesnik, S., & Pierson, R. N., 2006, Anthropometry in Body Composition: An Overview, *Annals of the New York Academy of Sciences*, *904*(1), 317–326. https://doi.org/10.1111/j.1749-6632.2000.tb06474.x

Wheatley, B. B., Odegard, G. M., Kaufman, K. R., & Donahue, T. L. H., 2016a, How does tissue preparation affect skeletal muscle transverse isotropy?, *Journal of Biomechanics*, *49*(13), 3056–3060. https://doi.org/10.1016/j.jbiomech.2016.06.034

Wheatley, B. B., Pietsch, R. B., Haut Donahue, T. L., & Williams, L. N., 2016b, Fully non-linear hyper-viscoelastic modeling of skeletal muscle in compression, *Computer Methods in Biomechanics and Biomedical Engineering*, *19*(11), 1181–1189. https://doi.org/10.1080/10255842.2015.1118468

Winters, J., Stark, L., & Seif-Naraghi, A. H., 1988, An analysis of the sources of musculoskeletal system impedance, *Journal of Biomechanics*, *21*(12), 1011–1025. https://doi.org/10.1016/0021-9290(88)90248-5

Zhang, S., & Duan, E., 2018, Fighting against Skin Aging: The Way from Bench to Bedside, *Cell Transplantation*, *27*(5), 729–738. https://doi.org/10.1177/0963689717725755

Zheng, Y., Mak, A. F., & Lue, B., 1999, Objective assessment of limb tissue elasticity: development

of a manual indentation procedure., *Journal of Rehabilitation Research and Development*, *36*(2), 71–85.